Fundamental Studies of Electrochemical Reactions and Microfluidics in Proton Exchange Membrane Electrolyzer Cells

A Dissertation Presented for the

Doctor of Philosophy

Degree

The University of Tennessee, Knoxville

Jingke Mo

December 2016

Copyright © 2016 by Jingke Mo

All rights reserved.

ACKNOWLEDGEMENTS

I would like to express my most sincere gratitude to my advisor, Dr. Feng-Yuan Zhang for his support, patience and guidance throughout my entire graduate school. I would like to thank Dr. Matthew M. Mench, Dr. Zhili Zhang and Dr. Lloyd M. Davis for serving on my committee and giving me valuable advice towards my research.

I would also like to thanks the entire research group Zhenye Kang, Gaoqiang Yang, Dr. Bo Han, Stuart M. Steen III, William Barnhill, Aaron Liu, Matthew Middleton, it has been my privilege working amongst you. I'd also like to thanks Dr. Lei Shi, Dr. Zhongren Yue, Rong Chen, Douglas Warnberg, Alexander Terekhov, Natallia Kaptur, Kathleen Lansford, Dr. Lee Leonard, Dr. Lino Costa, Gary Payne, and Jack LeGeune for their countless help on my research.

I also want to express my appreciation to Dr. Scott Retterer, Dr. Dave Cullen, Dr. Todd J. Toops, Dr. Michael P. Brady, Dr. Ryan R. Dehoff, Dr. William H. Peter, Dr. Ryan R. Dehoff, Dr. William H. Peter, Dr. Johney B. Green Jr., Dayrl Briggs, Dale Hensley, Kevin C. Lester, and Dr. Bernadeta R. Srijanto from ORNL for assisting me with my material characterization and fabrication.

My friends and family have been extremely helpful throughout my doctoral work. Finally, I wish to thank my parents and my sister for their unconditional love and support, and their belief in me to succeed. They always support me to pursuit of my dreams.

ABSTRACT

In electrochemical energy devices, including fuel cells, electrolyzers and batteries, the electrochemical reactions occur only on triple phase boundaries (TPBs). The boundaries provide the conductors for electros and protons, the catalysts for electrochemical reactions and the effective pathways for transport of reactants and products. The interfaces have a critical impact on the overall performance and cost of the devices in which they are incorporated, and therefore could be a key feature to optimize in order to turn a prototype into a commercially viable product. For electrolysis of water, proton exchange membrane electrolyzer cells (PEMECs) have several advantages compared to other electrolysis processes, including greater energy efficiency, higher product purity, and a more compact design. In addition, the integration of renewable energy sources with water electrolysis is very attractive because it can be accomplished with high efficiency, flexibility, and sustainability. However, there is a lack in fundamental understanding of rapid and microscale electrochemical reactions and microfluidics in PEMECs. This research investigates the multiscale behaviors of electrochemical reactions and microfluidics in a PEMEC by coupling an innovative design of the PEMEC with a high-speed and micro-scale visualization system (HMVS). The results of the investigation are used to aid in revealing the electrochemical reaction mechanisms and the microfluidics behavior including bubble generation, growth and detachment, which all together play a very important role in the optimization of the design of PEMECs. The effects of operating parameters such as current density, temperature and pressure on the electrochemical reactions and the microfluidics are determined and analyzed by mathematical models of PEMECs, which also match the experimental results. Improved understanding of the

electrochemical reactions and microfluidics in PEMECs can not only help to optimize their designs, but can also help advance many other applications in energy, environment and defense research fields.

TABLE OF CONTENTS

CHAPTER 1 INTRODUCTION AND LITERATURE REVIEW 1

1.1 MOTIVATION 1

1.2 BACKGROUND 4

1.3 SIGNIFICANCE 10

CHAPTER 2 STAINLESS STEEL LIQUID/GAS DIFFUSION LAYER 11

2.1 INTRODUCTION 11

2.2 MATERIALS AND METHODS 13

2.3 RESULTS AND DISCUSSION 14

2.4 CONCLUSION 22

CHAPTER 3 TITANIUM 3D PRINTING LIQUID/GAS DIFFUSION LAYER 24

3.1 INTRODUCTION 24

3.2 MATERIALS AND METHODS 27

3.3 RESULTS AND DISCUSSION 32

3.4 CONCLUSION 41

CHAPTER 4 TITANIUM THIN/WELL TUNABLE LIQUID/GAS DIFFUSION LAYER 43

4.1 INTRODUCTION 43

4.2 MATERIALS AND METHODS 46

4.2.1 Nano-manufacturing of titanium thin/well-tunable LGDLs 46

4.2.2 Test system and in-situ characterizations 48

4.2.3 Ex-situ characterizations 49
4.3 RESULTS AND DISCUSSION 50
4.3.1 Ex-situ characterization of titanium conventional and novel thin LGDLs 50
4.3.2 PEMEC performance and efficiency 50
4.3.3 Electrochemical impedance spectroscopy results 53
4.4 CONCLUSION 57
CHAPTER 5 MECHANISM OF ELECTROCHEMICAL REACTION IN PEMECS 58
5.1 INTRODUCTION 58
5.2 METHODOLOGY 63
5.3 RESULTS AND DISCUSSION 72
5.4 CONCLUSION 90
CHAPTER 6 DIRECT VISUALIZATION OF BUBBLE DYNAMICS IN PEMECS 92
6.1 INTRODUCTION 92
6.2 MATERIALS AND METHODS 95
6.3 RESULTS AND DISCUSSION 102
6.4 CONCLUSION 111
CHAPTER 7 MATHMATICAL MODELING INVESTIGATION ON OXYGEN BUBBLE EVOLUTION IN PEMECS 113
7.1 INTRODUCTION 113
7.2 METHODOLOGY 119
7.2.1 Mathematical model of oxygen bubble growth 119

7.2.2 Mathematical model of oxygen bubble detachment 121
7.3 RESULTS AND DISCUSSION 124
7.3.1 Effects of parameters on the bubble growth 125
7.3.2 Effects of parameters on the bubble detachment 131
7.4 CONCLUSION 134
CHAPTER 8 CONCLUSIONS AND SUGGESTIONS FOR FUTURE WORK 138
REFERENCES 144
VITA 168

LIST OF TABLES

Table 5.1 Main calculation parameters for mathematical modeling of equivalent circuit for catalyst layer in PEMECs 86

Table 6.1 Main parameters in experiments 101

Table 7.1 Parameters in calculation of bubble dynamics 126

LIST OF FIGURES

Figure 1.1. Schematics of applications of PEM electrolyzer cells for energy storage coupled with sustainable energy sources. 3

Figure 1.2. Schematic of the working process in a PEMEC. 6

Figure 1.3. 3D Schematic of the components of a PEMEC. 7

Figure 2.1. SEM images of anode stainless steel mesh LGDL, (A) fresh sample; (B) used sample; (C) Close-up of (B); (D) EDS results. 15

Figure 2.2. SEM images of cathode carbon paper LGDL, (A) fresh sample; (B) used sample; (C) Close-up of (B); (D) EDS results. 17

Figure 2.3. XRD patterns of anode stainless steel mesh LGDL, (A) fresh sample; (B) used sample. 19

Figure 2.4. XRD patterns of cathode carbon paper LGDL, (A) fresh sample; (B) used sample 21

Figure 3.1. Schematic of the functions of LGDL at anode of PEMECs. 25

Figure 3.2. Schematic of a PEMEC with a LGDL of EBM Ti-6Al-4V mesh. 28

Figure 3.3. Images of an EBM Ti-6Al-4V mesh LGDL at different scales. 33

Figure 3.4. Schematic of LGDLs with different fabrication method, (A) EBM Ti-6Al-4V mesh, (B) woven mesh. 33

Figure 3.5. XRD Pattern of the EBM Ti-6Al-4V mesh LGDL. 35

Figure 3.6. Performance curves of PEMEC with an anode LGDL of an EBM Ti-6Al-4V mesh and a Ti woven mesh at room temperature. 36

Figure 3.7. GEIS curves of PEMEC with an anode LGDL of an EBM Ti-6Al-4V mesh and a Ti woven mesh under the current density of 2 A/cm^2 at room temperature. 37

Figure 3.8. Performance results of a PEMEC with anode LGDL of an EBM Ti-6Al-4V mesh at different temperatures. 39

Figure 3.9. GEIS results of a PEMEC with an anode LGDL of EBM Ti-6Al-4V mesh at different temperatures. 40

Figure 4.1. Schematic of LGDL functions at the anode of PEMECs. 45

Figure 4.2. Typical wet etching fabrication process for titanium thin LGDLs..... 48

Figure 4.3. SEM Images of titanium conventional and thin LGDLs with similar pore size (a) titanium felt LGDL with average pore size of 100 µm and porosity of 0.78; (b) titanium thin LGDL with a pore size of 100 µm and porosity of 0.30. 51

Figure 4.4. Performance comparisons of PEMEC with titanium thin LGDL and conventional LGDL (red colour: titanium thin/ well tunable LGDL with thickness of 25 µm, pore size of 100 µm and porosity of 0.30; black color: titanium felt LGDL with thickness of 350 µm, average pore size of 100 µm and porosity of 0.78). 52

Figure 4.5. EIS comparisons of PEMEC with titanium thin etched LGDL and conventional LGDL (red colour: titanium thin/ well tunable LGDL with thickness of 25 µm, pore size of 100 µm and porosity of 0.30; black color: titanium felt LGDL with thickness of 350 µm, average pore size of 100 µm and porosity of 0.78). 55

Figure 5.1. Schematics of applications of PEM electrolyzer cells and PEM fuel cells coupled with renewable energy sources. 59
Figure 5.2. Schematic of a cross-section view of a PEMEC. 61
Figure 5.3. Schematic of the transparent and reaction-visible PEM electrolyzer cell, LGDLs have well-controllable and throughout straight holes. 65
Figure 5.4. Schematic of a developed nano fabrication process for titanium thin-film LGDL with well-tunable micro pores. 68
Figure 5.5. A sequence of pore-scale images of electrochemical reactions (triangular pore size: 600 μm, water is fully fill the channel and flowing from right to left): (A) Initial time, t_0; (B) t_0 + 0.0017 s; (C) t_0 + 0.0033 s; (D) t_0 + 0.005 s; (E) t_0 + 0.0067 s; (F) t_0 + 0.0083 s. 70
Figure 5.6. Micro-scale electrochemical reactions in PEMECs. (A) Front-view image of electrochemical reactions in the PEMEC microchannel. (B) 600 μm triangular pore; (C) 400 μm triangular pore; (D) 500 μm circular pore; (E) 50 μm circular pore. (Please see the detail from the supplementary material: Movie S1, Movie S2, Movie S3, Movie S4 and Movie S5). 73
Figure 5.7. Schematic of pore-scale electrochemical reactions occurred in the anode of a PEMEC. (A) True phenomena of electrochemical reactions occurred in PEMECs. (B) Conventional assumption of electrochemical reactions in PEMECs. (C) triple-phase boundary electrochemical reaction in PEMECs. (D) Phenomena of exclusive experiments for electrochemical reaction occurred in the anode of PEMECs (white wire: conductive material, yellow wire: non-conductive material, please see the detail from the supplementary material: Movie S6 and Movie S7).

(E) Future design and fabrication of catalyst layer in PEMECs, the catalyst only deposits on the lands of LGDLs..... 76

Figure 5.8. Comparison of different catalyst loading method and substrates in the cathode of a PEMEC (one is on membrane and the other one is on LGDL). (A) Schematic of catalyst conventional-method loaded on membrane in PEMECs. (B) Schematic of catalyst sputter coated on LGDL in PEMECs. (C) SEM and zoom-in images of catalyst crystal structure which loaded on the membrane. (D) SEM and zoom-in images of catalyst crystal structure which loaded on the LGDL. (E) Comparison of cell voltage between cathode catalyst with a conventional method loaded on membrane and sputter coated on LGDL. (F) Comparison of H_2 production rate per catalyst loading between conventional method loaded on membrane and sputter coated on LGDL..... 79

Figure 5.9. Schematic of ohmic distribution inside a PEMEC..... 82

Figure 5.10. Schematic of an analyzing unit with dividing catalyst in a 100 μm diameter opening into 50 torus and equivalent circuit..... 84

Figure 5.11. The relationship between current and distance away from the edge of opening, L. (L is the distance between torus and the edge of circular pore). 88

Figure 5.12. The relationship between in-plane resistivity of catalyst layer with current distribution on the surface of catalyzer layer. (Red dot is the results of CL with in-plane resistivity of 1.52×10^{-2} Ω·m, blue dot is the results of CL with in-plane resistivity of 1.52×10^{-3} Ω·m, black dot is the results of CL with in-plane resistivity of 1.52×10^{-5} Ω·m). 89

Figure 6.1. Four typical two-phase flow patterns in horizontal microchannel. 94

Figure 6.2. Schematic of two-phase flow in a triangle micro-pore in LGDLs with different wettability. 94
Figure 6.3. Schematics of a transparent proton exchange membrane electrolyzer cell. ... 97
Figure 6.4. Schematic of the thin/well tunable LGDL fabrication process and SEM images of fabricated LGDLs. 99
Figure 6.5. Schematic of a high-speed, micro-scale visualization system. 100
Figure 6.6. Sequence of photos for oxygen bubble generation, growth and detachment in a micro circular pore of an operating PEMEC under different current densities of (a) 0.02 A/cm^2, (b) 0.2 A/cm^2 and (c) 2 A/cm^2; the time interval between each picture (i-ii-iii) in sequence: (a) is 1.0 ms, (b) is 4.7 ms, and (c) is 2.3 ms. 103
Figure 6.7. A sequence of images of two-phase flow in the anode microchannel of an operating PEMEC. 105
Figure 6.8. A sequence of two-phase flow pattern changed in the anode microchannel of an operating PEMEC. 108
Figure 6.9. Oxygen bubble detach diameters in the microchannel of PEMECs under different current densities of (a) 0.02 A/cm^2, (b) 0.2 A/cm^2, (c) 0.4 A/cm^2, (a) 0.8 A/cm^2, (b) 1.6 A/cm^2, and (c) 2.0 A/cm^2. 110
Figure 7.1. Schematics of gas/liquid two-phase transport and microstructure in a PEMEC. 114
Figure 7.2. Schematic of bubble generate and growth on the surface of substrate..... 120
Figure 7.3. Schematic of bubble force analysis and detachment situations on a LGDL surface. 121

Figure 7.4. Comparison of the modeling data and experimental data for oxygen bubble growth in PEMECs. 128
Figure 7.5. Effect of temperature on oxygen bubble growth. 129
Figure 7.6. Effect of pressure on oxygen bubble growth. 130
Figure 7.7. Effect of current density on oxygen bubble growth. 132
Figure 7.8. Effect of temperature on the oxygen bubble detachment. 135
Figure 7.9. Effect of pressure on the oxygen bubble detachment. 136

CHAPTER 1

INTRODUCTION AND LITERATURE REVIEW

1.1 Motivation

The demand for power has increased rapidly over the past decades, due to economic growth, population expansion, and industrialization of developing countries worldwide. Meeting this demand can be difficult and often result in high levels of pollutions and greenhouse gases (GHG) emissions, thus creating serious health and environmental concerns and elevating indirect cost on society. Industries, such as power generation, manufacturing and transportation, often rely on non-renewable resources that stress the energy grid and accelerating the pollution of atmosphere. To combat those issues, there's been a shift to employ renewable technology, a superior method energy generation from nature resources, such as hydro, wind and solar. Renewables are well suited for diverse of energy demands and various industries by providing sustainable, clean and efficiency energy. Free of harm for pollution or GHG emissions. However, intermittent power disruptions are common with dealing with renewable resources. This occurs where there is mismatch between the supplier energy generated and consumption demanded. Energy storage eases intermittent power disruptions by storing excess power generated from renewable resources at the time of low demand and distributing the power at the periods of heightened demand. This helps balance the load on energy created and reduce dependence on nonrenewable resources. Hydrogen, as a high-energy density and environmentally friendly fuel, is expected to be one of the most promising energy carriers in the near future [1-4]. However, hydrogen is not an energy source; it doesn't exist in nature in its elemental or molecular form; therefore,

hydrogen must be produced. Water electrolysis, a carbon free way to produce fuel when coupled with renewable or nuclear energy sources, can split water into hydrogen and oxygen by using electrical power. The integration of a sustainable energy source and water electrolysis as shown in Figure 1.1 is very attractive because of its high efficiency, lack of carbon and numerous applications, although the cost is still higher than other conventional energy sources [5-10]. Proton exchange membrane electrolyzer cells (PEMECs) have a number of advantages compared to other electrolysis processes, including production of hydrogen at a higher purity, capable of operation at higher current density on the electrodes leading to faster reaction, and the ability to operate at pressures up to 200 bar thus providing the advantage of delivering the hydrogen at a high pressure for the end user. These benefits all contribute to the choice of PEM based electrolysis as the best method to supply hydrogen [11-14]. Although the first solid polymer electrolyte cell has been built in 1960s by General Electrics Ltd [15], PEMECs have several big obstacles to overcome to be widely used in hydrogen production industry, including cost, durability and efficiency [13]. PEMECs use proton exchange membranes (PEMs) as an electrolyte that permits the transfer of protons from anode to cathode, and employ RuIrOx and Pt Black as the anode and cathode catalysts, respectively [8, 16]. The main effects on costs are noble metal catalyst loading/catalyst utilization for electrochemical reaction and degradation of layers and interfacial contacts of PEMECs under the electrochemical reaction. In PEMECs, the oxygen is generated at the anode side by triple-phase boundary reactions, and the water flowing over the liquid/gas diffusion layer (LGDL) yield two-phase transport conditions, which strongly affect the performance [17]. It has become more critical for understanding

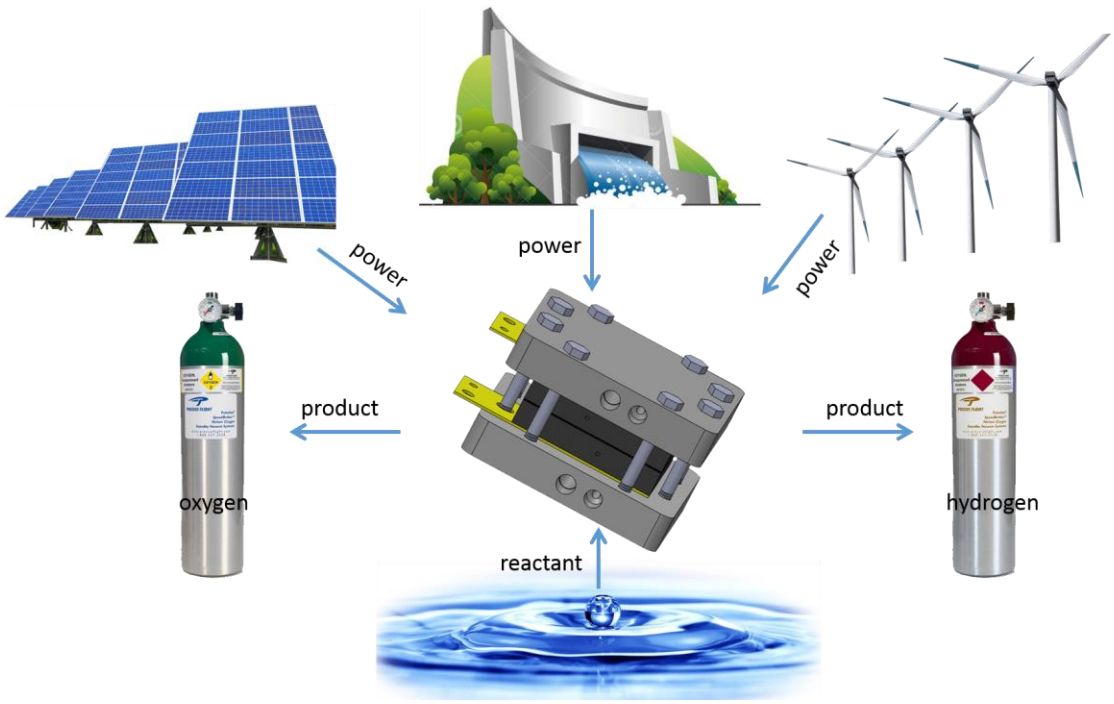


Figure 1.1. Schematics of applications of PEM electrolyzer cells for energy storage coupled with sustainable energy sources.

the fundamental principle of electrochemical reaction and microfluidics in PEMECs. The aim of this study is to investigate the mechanism of electrochemical reaction and behavior of microfluidics inside the PEMECs to aid in optimization of developing a high-performance and low-cost sustainable energy storage system.

1.2 Background

Hydrogen as a clean and environmentally acceptable fuel is expected to be one of the most promising energy carriers in the near future. Water electrolysis is one of the most attractive solutions to produce hydrogen in a clean and efficient way, and it is also considered a significant technique in the solutions of both energy and environment, since it can split the water into hydrogen and oxygen coupled with renewable energy resources such as wind or solar. Electrolysis of water is the decomposition of water into oxygen and hydrogen gas due to an electric current being passed through the water. The reaction with the thermodynamic energy values is described in following Equation (1).

$$H_2O + 237.2\,\frac{kj}{mol}\,(electricity) + 48.6\,\frac{kj}{mol}\,(heat) \xrightarrow{Catalyst} H_2 + \frac{1}{2}O_2 \qquad (1)$$

The stoichiometric equations for the electrochemical reactions at both side of PEMEC are the same as other methods of water electrolysis, as shown in below Equation (2) and Equation (3).

$$Anode:\ 2H_2O \xrightarrow{Catalyst} 4H^+ + O_2 + 4e^- \qquad (2)$$

$$Cathode:\ 4H^+ + 4e^- \xrightarrow{Catalyst} 2H_2 \qquad (3)$$

Oxygen and hydrogen gas can be generated at noble metal loaded catalyst layer. At the positively charged anode, an oxidation reaction occurs, generating oxygen gas and giving electrons to the circuit. At the negatively charged cathode, a reduction reaction takes place,

with electrons from the circuit being given to hydrogen cations to form hydrogen gas. Theoretically, the amount of gases produced per unit time is directly related to the current that passes through the electrochemical cell. The principle of a PEMEC is electrochemically splitting water into hydrogen and oxygen. During the operation, at the anode side, water is circulated through a flow field to the membrane electrode assembly (MEA) where it electrochemically reacts with catalyst and is split into oxygen, protons and electrons. The protons are then transported through the membrane, react with electrons from an external electrical circuit, and form hydrogen gas at the cathode, which exits through the flow channel at cathode side. Meanwhile, the oxygen is transported along with the water out of the anode. The schematic cross-section view of a PEMEC is shown in Figure 1.2.

Compare to the conventional methods, with higher energy efficiency/density, faster charging/discharging, and a more compact design, PEMECs have attracted significantly attention from the last decade [18]. A PEMEC mainly consists of a membrane electrode assembly (MEA) sandwiched by two electrodes. As a key component, the MEA is comprised of the proton exchange membrane, catalyst layers and LGDLs. The schematic is as shown in Figure 1.3.

To improve the performance and durability of the PEMECs, the catalyst coated membrane (CCM) of the PEMECs has been studied and developed by many scholars [19, 20]. It has also been seen in the past researches that metallic cation, especially iron cation, contaminated the membrane in a PEMFC [21-25]. In CCM, the Nafion ionomer is a multifunctional component. It acts as a conductor extending proton conduction from the

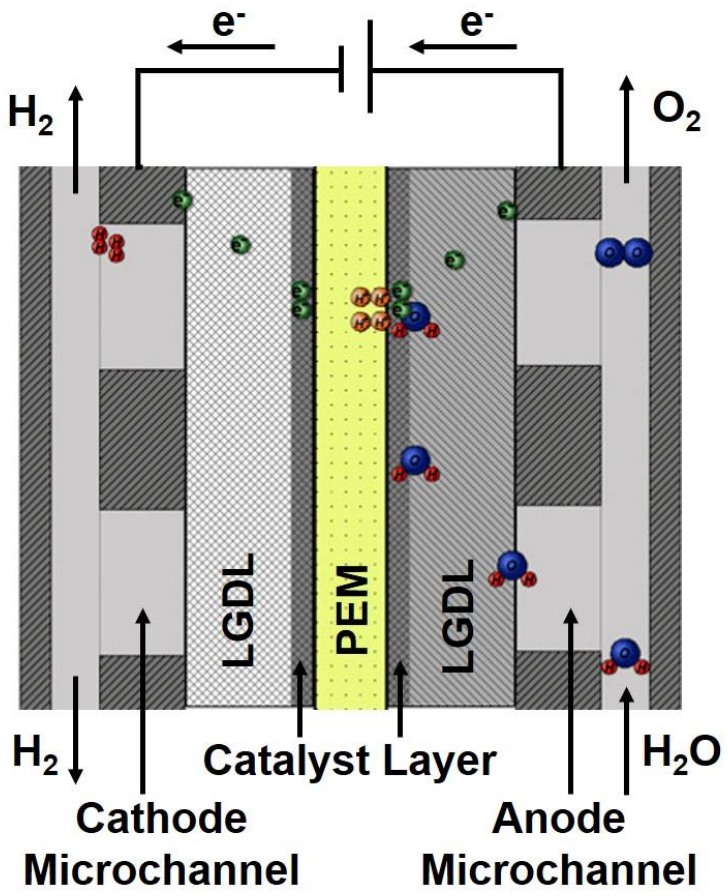


Figure 1.2. Schematic of the working process in a PEMEC.

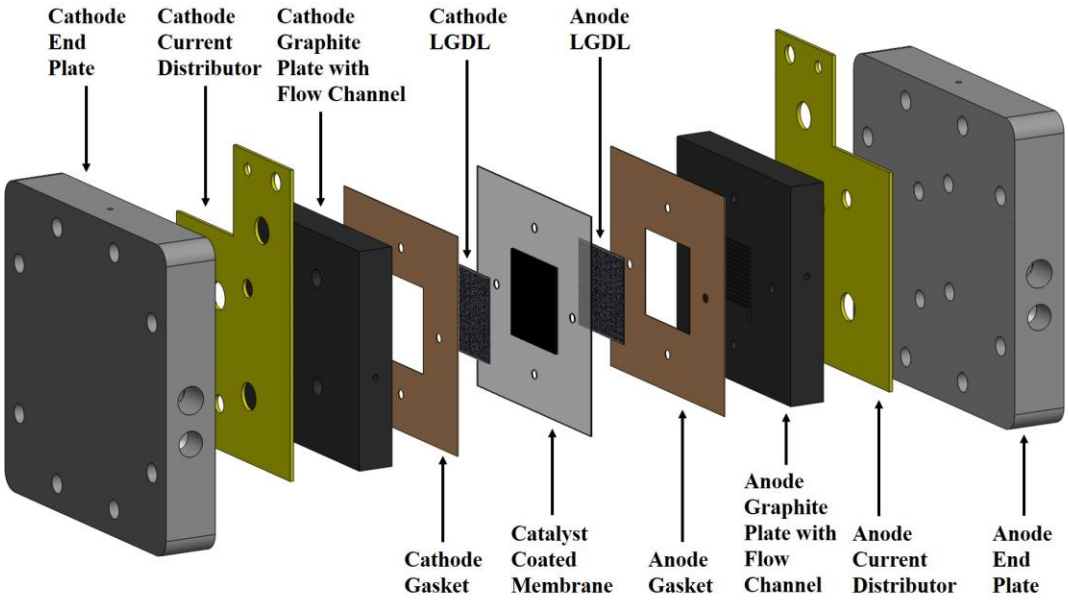


Figure 1.3. 3D Schematic of the components of a PEMEC.

PEM membrane to the surface of catalysts, a binder providing a three-dimensional structure of the catalyst layer, with abundant gas channels and certain mechanical stability, and a hydrophilic agent retaining moisture inside the catalyst layer. Similar to PEM fuel cells, the proton exchange membrane is applied as electrolytes that permit the transfer of protons with high efficiency from anode to cathode in a PEMEC.

The performance of PEMECs is highly depends on properties of the membrane electrode assembly (MEA), including membrane conductivities, activities of catalyst layers, and materials of LGDL. Expensive metal catalysts are used for the electrodes, generally Pt for the cathode and IrRuOx for the anode. Bipolar plates are generally made of titanium [26]. Choosing cheaper catalysts may effectively reduce the cost of PEMECs. However, there are few options for the researchers developing PEMECs. While carbon paper is widely used as a LGDL in fuel cells, it is unsuitable in the anode of PEMECs because it is easily corroded at the high positive potentials and oxidative environment present during water electrolysis operation [27, 28]. Therefore, studies of interfacial electrical reactions and two-phase transports on the MEAs of PEMECs, are of reasonable significance. Based on better fundamental understanding, optimization of the MEAs could improve the performances, extend the lifetime and reduce the cost of PEMECs currently with noble metal catalysts.

The performance of PEMECs, like PEM fuel cells, are typically compared by plotting their polarization curves, which is the relation of the cell voltage against the current density from the data of modeling or experiments. Based on polarization curves, the primary sources of overpotential in a PEMEC can be categorized into three main areas: activation losses,

ohmic losses and mass transport losses. Then the performance of PEMECs can be evaluated by following Equation (4).

$$V_{cell} = E + V_{act} + V_{ohm} + V_{con} \quad (4)$$

The first term E is the open circuit voltage (OCV) and is sometimes referred to as the reversible cell voltage (E), because it is the theoretical voltage required by the electrolyzer. The activation overvoltage, V_{act},is the voltage loss attributed to driving the electrochemical reaction and is necessary to overcome the molecular bonds. The ohmic losses, V_{ohm}, created by the resistance to the flow of electrons through the current collectors and separator plates as well as the conduction of protons through membrane and LGDL. The losses due to mass transfer, V_{con},are caused by flow restriction to the catalyst sites such as current collector and separator plate morphology as well as gas bubbles formed from the reaction products [13]. To improving the performance of PEMECs, each of these loses will be discussed individually in the following paragraphs.

First, the activation overpotential is energy losses in a reaction that can be described as the amount of energy require to start the reaction. This loss is directly affected by the temperature, catalyst material, utilization, loading and other factors. Secondly, the ohmic overpotential across the PEMEC is caused by the conductive resistances of each layers, interfacial contact resistance between each layers and the resistance of membrane to the hydrogen ions transporting through it. The ionic resistance of the membrane is related to the degree of humidification and thickness of the membrane as well as the membrane temperature. Thirdly, the concentration overpotential occurs when electrochemical reaction is sufficiently rapid to lower the surface concentration of reactant, which close

relate to the water supply and oxygen removal in PEMECs. It makes microfluidics significant effect the performance under high current density.

According to aforementioned situation, there are several challenges in present PEMECs: reduction and/or substitution of noble catalysts, increase the catalyst utilization, development of low cost and corrosion resistant LGDL and current collectors, development of both empirically and physically predictive relations for operating parameters. Those challenges are all connected to the mechanism and behavior of electrochemical reaction and microfluidics in PEMECs.

1.3 Significance

To better understanding the mechanism of electrochemical reaction and microfluidics in PEMECs, a novel design of PEMEC with thin/well tunable LGDL are introduced specifically to observe the phenomena on the surface of anode catalyst layer and inside microchannel and micro pores. The multi-phase boundary reactions theory is the common accepted concept for electrochemical reaction in PEMECs. Better understanding the multi-phase boundary reactions inside PEMECs can not only help to design a better LGDL to improve the performance of PEMECs, but can also direct the distribution pattern fabrication of catalyst on CCM, which can significant increase the mass activity of catalyst. Moreover, discovering the behavior of microfluidics in LGDLs and flow channels is also vital for promoting performance and optimizing the design of PEMECs. These results can also help validate the comprehensive mathematics models in the future. This research will provide several future research directions to aid in establishing PEM electrolysis as a commercially viable hydrogen production solution.

CHAPTER 2

STAINLESS STEEL LIQUID/GAS DIFFUSION LAYER

2.1 Introduction

Hydrogen, as a high energy and environment friendly fuel, has the potential to be a promising energy source in the near to intermediate future. An electrolyzer cell taking advantage of a proton exchange membrane (PEM) has attracted more attention for renewable energy storage and pure hydrogen/oxygen production due to their higher energy efficiency/density, faster charging/discharging, and a more compact design [13, 29-31]. The proton exchange membrane electrolyzer cell (PEMEC) splits water into separate streams of hydrogen and oxygen by using electrical power. The integrations of water electrolysis and energy from sustainable resources, including solar, wind and biomass, are very attractive because of its high efficiency, renewable, and pure hydrogen production [3, 7, 8, 14, 32, 33]. Once hydrogen is produced and stored, it can later provide a constant supply of electricity with a PEM fuel cell (PEMFC), which is a reverse device of the PEMEC. This regenerative system will allow renewable and hybrid energy systems to effectively provide reliable and multi-scale energy [34-37]. Compared to traditional technologies, both PEMECs and PEMFCs take advantage of proton exchange membranes as electrolytes that permit the transfer of protons with high efficiency. Their performance is highly dependent on properties of the membrane electrode assembly (MEA), including conductivity of the membrane, activation energy of the catalyst layers, and the conductivity and permeability of liquid/gas diffusion layers (LGDLs) [16, 19, 20, 27, 28, 38, 39]. PEMFC performance can also be affected by species concentration variations across and

within the cells which can reflect changes in reactants and products distribution and transport, localized and possibly dynamic active-site blocking, and membrane degradation [40, 41].

Metallic LGDLs and bipolar plates have attracted attentions in both PEMECs and PEMFCs due to their high conductivity, rapid production, and low cost.[22, 42-45] By taking advantage of novel designs and micro fabrications, a thin-film metallic LGDL with well-controllable pore morphologies and surface properties demonstrated excellent multi-functionalities and water managements [42, 46]. However, its durability has been challenged due to the aggressive electrochemical environment. In addition, while carbon paper is widely used as the LGDL in fuel cells, it is unsuitable in the anode side of PEMECs because it is easily corroded at the high positive potentials and extreme oxidative environments. Metallic LGDLs with higher corrosion resistance are one potential solution. Metal corrosion and ion poisoning on MEAs are critical issues especially for low-cost metals such as stainless steel. Current bipolar plate practically employs the use of more expensive metals such as titanium, and typically with precious metal coatings such as Pt, which significantly increase the cost [8]. It has been reported that metallic cations, especially iron cations, may contaminate the MEA and degrade the performance in PEMFCs [21-23, 47, 48]. However, to our knowledge, there are few (if any) reports on the electrode corrosion and transport mechanisms/effects in a MEA, especially with metallic LGDLs.

In this study, a stainless-steel mesh was purposely employed as the anode LGDL to develop an understanding of the metal ion migration and deactivation mechanism and identify alternative materials suitable for use in PEMEC. Scanning electron microscope (SEM)

characterizations of both anode and cathode LGDLs before and after testing were performed to compare the extent of metal migration in the materials. X-ray diffraction (XRD) has been demonstrated to be an effective method that readily provides quantitative information about the phase-composition of solid material [49, 50]. The LGDLs have also been analyzed by XRD for the identification of the form of the migrating metals. Migration of iron across the MEA resulting in the formation of iron oxide on the carbon paper gas diffusion layer at cathode side is observed, which to our knowledge is the first or among the first reports of this phenomenon for PEMEC.

2.2 Materials and methods

In the PEMEC used in the present study, both end plates are made of aluminum. The anode current distributor with a parallel flow field is fabricated from a titanium plate, while the cathode current distributor is fabricated from copper and coated with nickel and chromium. The cathode flow field is also a parallel flow field that is fabricated from graphite. Both anode and cathode gaskets are made from PVC sheets. The cathode LGDL is Toray 090 carbon paper treated with 5% PTFE. The anode LGDL is a type 316 stainless steel mesh (nominal composition of 316 is 16-18.5% Cr, 10-14% Ni, 2-3% Mo, <2% Mn, <1% Si, all in weight %). The catalyst-coated membrane (CCM) is Nafion 115 film with Ru/Ir oxides and Pt employed as anode and cathode catalysts with loadings of 3 mg/cm^2, respectively. Eight evenly distributed bolts assembled the cell to a torque of 40 lb-in. Teflon piping and fittings were used throughout the system. While the cathode tubing was merely intended to safely exhaust hydrogen gas, a diaphragm liquid pump from KNF Neuberger was used to circulate water at a constant volumetric flow rate of 40 ml/min through the anode [39]. The electrolyzer with an active area of 5 cm^2 was operated for 15 hours with an average

operation voltage of 2.8 V at a current density of 1 A/cm^2 at room temperature. Before and after the water electrolyzer testing, the leak and crossover tests were performed with air. This evaluation produced identical results in the fresh and aged CCMs and no pinhole formation was found.

The morphological characteristics of the LGDLs were observed with a field emission SEM JEOL JSM-6320F with an accelerating voltage of 0.5-30kV, a magnification of 500x ~ 650,000x and a 5-axis specimen mount. The EDS detector is an EDAX Octane plus Silicon Drift Detector that works in tandem with EDAX's TEAM EDS software analysis system. The system allows for high resolution mapping and highly accurate point analysis at fast speeds. SEM images were captured, processed, and analyzed by TEAM software.

The characterization of structure and identification of the phase were carried out by XRD with a Philips X'Pert materials research diffractometer (45kV, 40mA), controlled by PANalytical's XRD software, in Bragg Brentano reflection geometry with Cu Kα radiation (λ=1.5418 Å) and a 2θ scan from 20° to 100° (at 0.01° per 5 second). The diffraction patterns are analyzed by software MDI Jade9 [51].

2.3 Results and discussion

The experimental results include two major parts: SEM characterizations and XRD investigations of fresh and used LGDLs from both anode and cathode sides in PEMECs. Figure 2.1Figure 2.1 shows the SEM images of fresh and used stainless-steel LGDLs at anode side, which reveals extensive corrosion of the stainless steel mesh after 15 hours of room temperature operation at a cell voltage of 2.8 V and a current density of 1 A/cm^2 in PEMEC. As shown in Figure 2.1 (A), the surface of fresh stainless steel mesh is smooth, while the

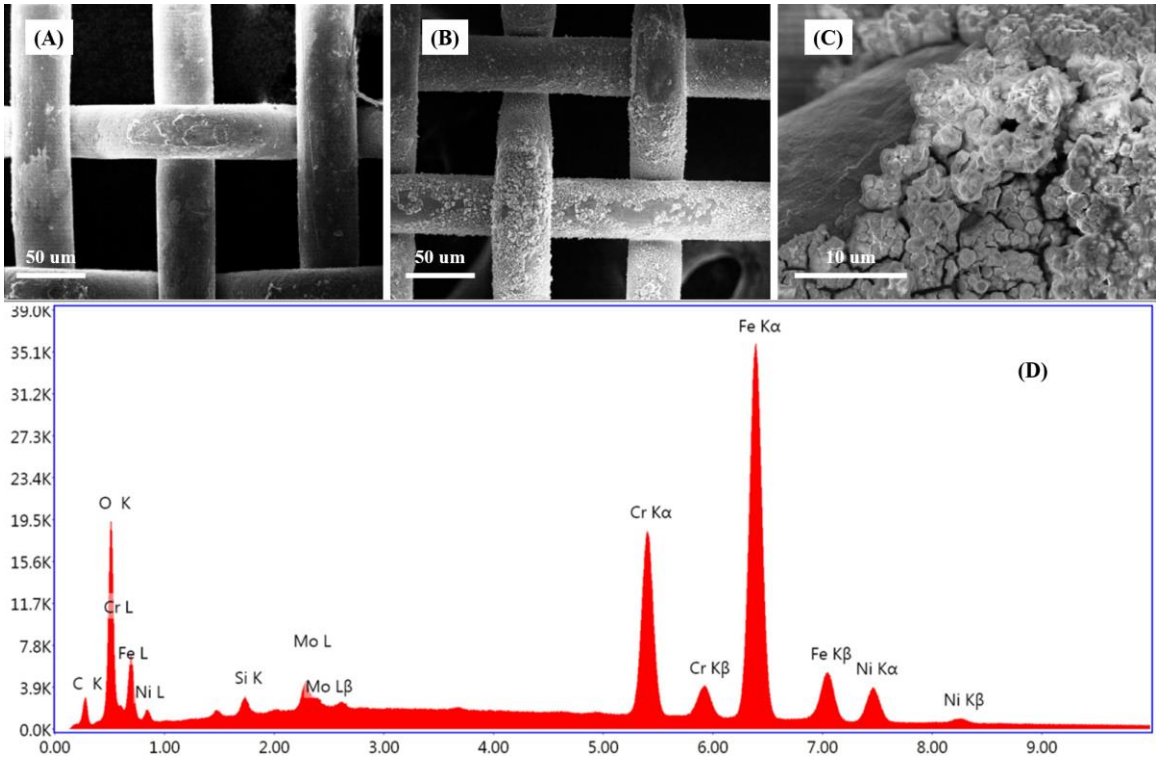


Figure 2.1. SEM images of anode stainless steel mesh LGDL, (A) fresh sample; (B) used sample; (C) Close-up of (B); (D) EDS results.

operated stainless steel shows a rough, corroded surface, which can be observed clearly in Figure 2.1 (B) and (C). The electrochemical reaction at anode side during PEMEC operation can be expressed as equation (5)

$$2H_2O \rightarrow 4H^+ + O_2 + 4e^- \quad (5)$$

The stainless steel at the anode side in the PEMEC experiences the high oxidative environment and high positive potentials. And the passive film is reported to be formed on the surface of stainless steel when the it is in the passive potential region, which is attributed to both reaction and diffusion mechanisms.[52] The growth of the oxide film is initially controlled by the oxidation reaction of iron and chrome elements. [53] Then, their diffusions becomes dominant in the barrier layer.[54] Passive films on stainless steels are heterogeneous and they have compositional and structural defects. The substance of the defects and the breakdown mechanism of passive films are still unclear. The reductive dissolution of the Fe_2O_3-component in passive films is considered to lead to passive film breakdown, which results in deeper corrosion in the substrate. [55, 56]. The passive film adheres loosely on the surface and can be spalled from the substrate surface. Similar oxidative attacks have been reported for stainless steels in supercritical water [57]. As shown in Figure 2.1 (C), some of outer loose layer detaches from the substrate, the outer layer is brittle, and the inside smooth layer is exposed. Based on EDS analysis Figure 2.1 (D), the outer corroded layer is a Fe-base oxide, with the smooth inner layer consistent with 316 metal.

The SEM images of fresh and operated carbon paper of the cathode LGDL is shown in Figure 2.2. The SEM image Figure 2.2 (A) for fresh carbon indicates the surface of sample is smooth, and the carbon fibers can be observed clearly. The SEM image of Figure 2.2 (B)

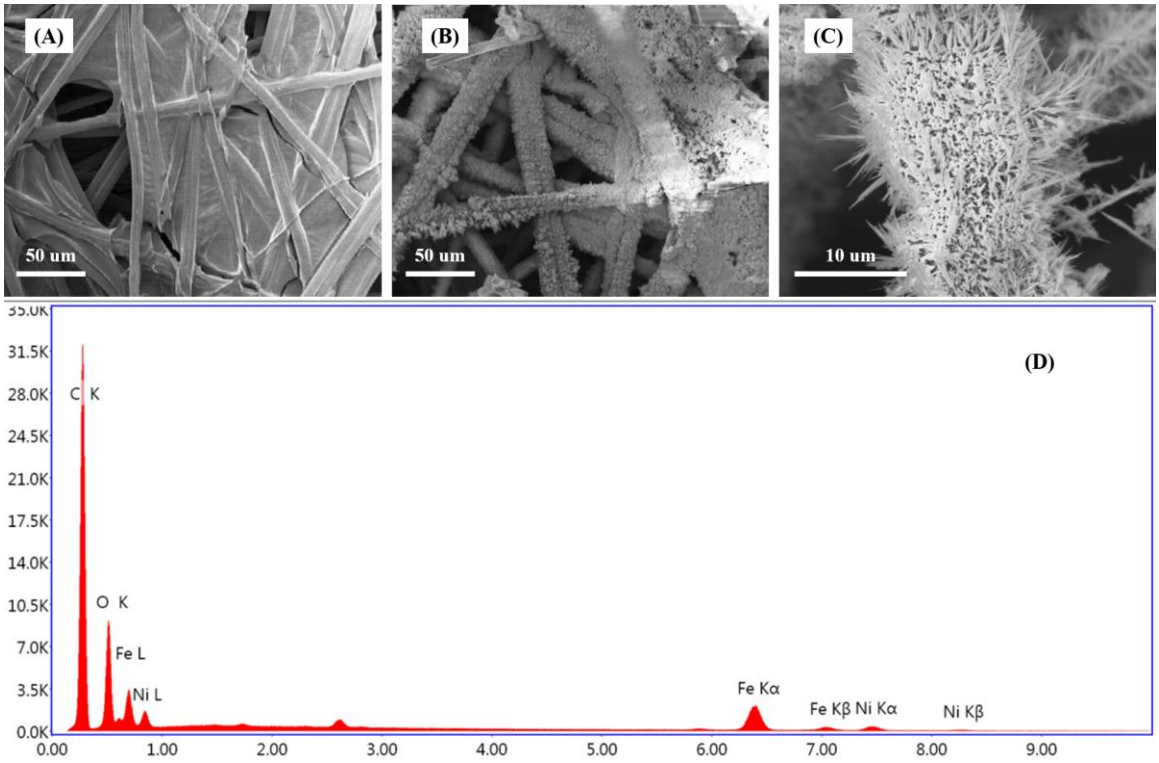


Figure 2.2. SEM images of cathode carbon paper LGDL, (A) fresh sample; (B) used sample; (C) Close-up of (B); (D) EDS results.

for used carbon paper shows the carbon fibers are fully covered by corrosion products, which is further examined in Figure 2.2 (C). The electrochemical reaction at cathode side results in hydrogen formation, which can be expressed as equation (6):

$$4H^+ + 4e^- \rightarrow 2H_2 \qquad (6)$$

Since the environment in the cathode side is different from one at the anode side, it is not expected that the carbon paper would be corroded as badly as shown in the SEM images of Figure 2.2 (B) and (C). According to this phenomenon, an EDS scan was conducted, the results of which indicated that the elements of crystal deposited on the surface of carbon paper were Fe, Ni, and O rich, as shown in Figure 2.2 (D). It can be hypothesized that iron and nickel ions diffused from the anode side to the cathode side and deposited onto the surface of the carbon fibers. The ratio of the content of Fe and Ni was roughly 1.5:1.

The X-Ray Diffraction pattern comparisons of anode and cathode LGDLs before and after testing in PEMECs are shown in Figure 2.3 and Figure2.4 , respectively. From the XRD pattern for the stainless steel mesh as shown in Figure 2.3 (A), the major phase at anode side LGDL fresh stainless steel 316 mesh is face-centered cubic austenite, although additional peaks consistent with deformation-induced alpha prime martensite were also observed (likely resulted from the mesh manufacturing process) [58]. After PEMEC operation, it can be observed that the peak intensity of α'(110) became weaker, while the austenite peak (111) became stronger, according to the XRD pattern of the anode LGDL as shown in Figure 2.3 (B).

During PEMEC operation, only electrochemical reaction occurred inside the cell, which kept the stainless steel mesh in the harsh environment at the anode side of PEMECs, caused the formation of oxide layer on the surface of stainless steel mesh. In the water electrolysis

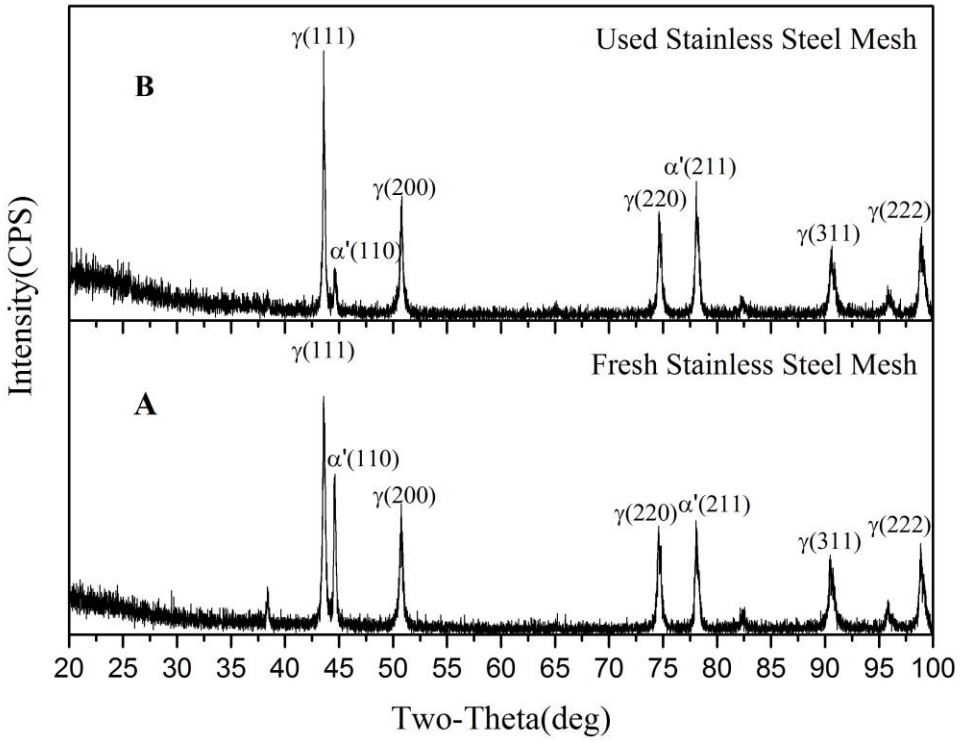


Figure 2.3. XRD patterns of anode stainless steel mesh LGDL, (A) fresh sample; (B) used sample.

process, the loosely oxide layer formed on the surface of anode LGDL stainless steel mesh [53, 57]. Since the anode LGDL stainless steel mesh is exposed in the flow of DI water, the oxide layer can be easily detached from stainless steel substrate due to shear stress of the flow and dissolved into the flow water. This process results in the phenomena in Figure 2.1 (C), rough outer iron oxide layer and smooth inner stainless steel substrate, which also has been verified by SEM results.

Figure 2.4 shows the XRD patterns for the cathode LGDL before and after testing, respectively. As shown in Figure 2.4 (A), the major phase in the cathode LGDL fresh carbon paper is graphite, which agrees well with reference [59]. After operation of the PEMEC, the XRD pattern for carbon paper, as show in Figure 2.4 (B), indicates iron oxide (Fe_3O_4) and nickel oxide (NiO) formation in the used carbon paper, which is absent in the fresh carbon paper. Those iron and nickel ions can only come from the anode LGDL, which is the sole portion of the PEMEC in which iron and nickel exists. In addition to the direct oxidation of iron, Fe and Ni cations can easily form into oxide in a wet environment [60]. This helps to explain why there is Fe oxide and Ni oxide on the surface of cathode LGDL carbon paper. This also indicates that the loose oxide layer of stainless steel detached from the stainless steel substrate, only some Fe oxide and Ni oxide dissolved into water with PH<7, since Cr oxide is insoluble in water with PH<7, the dissolved Fe and Ni ions transported from the anode LGDL stainless steel mesh to the cathode LGDL carbon paper through the catalyst-coated Nafion 115 membrane. The environment in the anode of the PEMEC is too aggressive for untreated stainless steel. The oxide films formed on 316 stainless steel exposed to anode high potential and extreme oxidative environment showed poor protection against corrosion. This baseline stainless steel sets a basis for the future

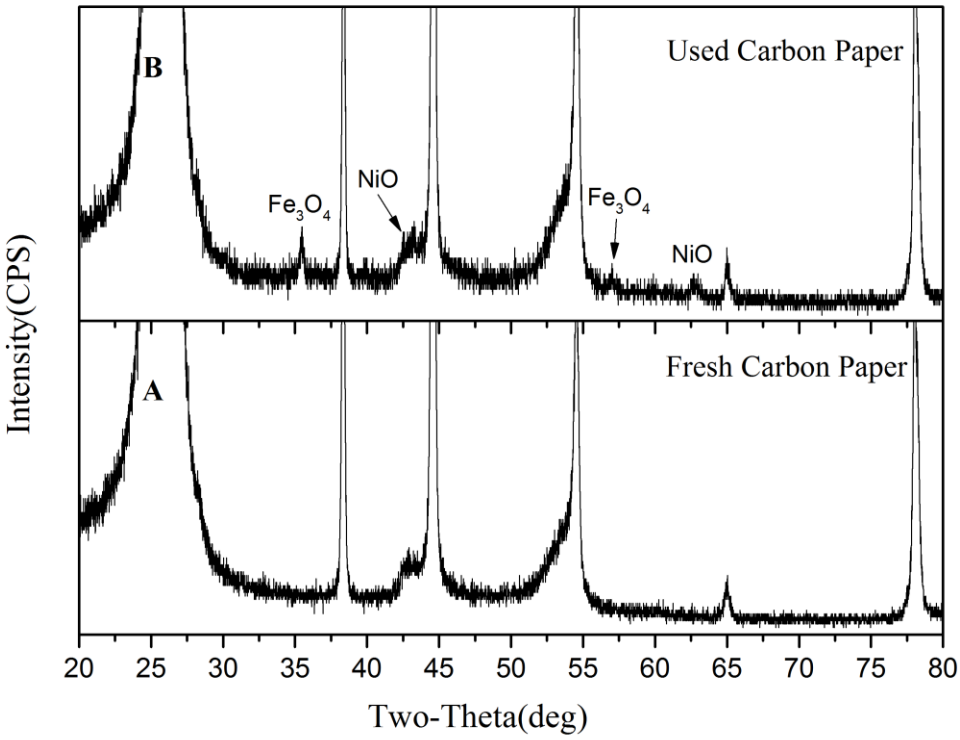


Figure 2.4. XRD patterns of cathode carbon paper LGDL, (A) fresh sample; (B) used sample

evaluation of coatings and/or comparison with other materials like Ti, which is usually used for metal LGDL in PEMEC.

The XRD patterns as shown in Figure 2.4 were scanned for the cathode LGDL before and after testing, respectively. XRD pattern of Figure 2.4 (A) indicates that the major crystal in cathode LGDL fresh carbon paper is graphite-2H, which agree well with reference [59]. After testing in the PEMEC, from the XRD pattern for carbon paper as show in Figure 2.4 (B), some iron oxide exists in the used carbon paper, which is absent in the fresh carbon paper. This iron oxide can only come from the anode LGDL, which is the sole portion of the PEMEC in which iron exists. In addition to the direct oxidation of iron, Fe_3O_4 can easily oxidize into Fe_2O_3 in a wet and high oxidative environment [60]. This helps to explain the reason why there is only Fe_2O_3 appeared on the cathode LGDL carbon paper, which also indicates that the iron oxide transported from the anode LGDL stainless steel mesh to the cathode LGDL carbon paper through the catalyst-coated Nafion 115 membrane.

2.4 Conclusion

For a better understanding of the corrosion mechanisms and ion transitions in electrochemical devices, a stainless steel mesh was purposely used as anode gas diffusion layer and was operated in a PEMEC with intentionally higher positive potentials under harsher oxidative environments. Large amount of iron is found to transport from anode to cathode, through the anode catalyst layer, the proton exchange membrane and the cathode catalyst layer. The formation of iron oxide and nickel oxide on single carbon fibers of a carbon paper gas diffusion layer on the cathode side is observed by both scanning electron microscope and x-ray diffraction. A visual comparison between SEM images shows that high levels of oxidation occur in PEMECs at room temperature, especially at the anode

side. The XRD pattern not only identifies the mechanism of oxidation on LGDLs, but also tracks the transportation pathways of corrosion from the anode to the cathode through the membrane along with SEM. The results indicate the corrosion elements of iron and nickel are transported from anode to cathode across through the catalyst-coated membrane, and deposited on carbon fibers. The test method and characterization have been demonstrated to be an effective approach to investigate corrosion mechanisms (transport and reformation) across MEAs in both quantitative and qualitative aspects. The addressed method could also open a new opportunity to fabricate multifunctional devices with single carbon fiber. In addition, this study has demonstrated a new accelerated test method, which can be easily for investigating the electrochemical corrosion and durability of various metallic materials.

CHAPTER 3

TITANIUM 3D PRINTING LIQUID/GAS DIFFUSION LAYER

3.1 Introduction

With a high-energy density and no harmful emissions, hydrogen has the potential to play an important role as an energy carrier in the future [2, 3, 61-65]. However, hydrogen is not an energy source; it doesn't exist in nature in its elemental or molecular form; therefore, hydrogen must be produced. Proton exchange membrane (PEM) water electrolysis, which was first developed in the mid-1970s by General Electric based on the first solid polymer electrolyte system deployed the Gemini Space Program [66], has been among the most efficient and practical means of producing hydrogen to date [67]. In recent years this technology has been developed significantly and has become more attractive to produce hydrogen from water and to store energy by taking advantage of renewable energy sources and new material innovations. Proton exchange membrane electrolyzer cells (PEMECs) have a number of advantages compared to other electrolysis processes, including production of hydrogen at a higher purity, capable of operation at higher current density on the electrodes leading to faster reaction, and the ability to operate at pressures up to 200 bar thus providing the advantage of delivering the hydrogen at a high pressure for the end user. These benefits all contribute to the choice of PEM based electrolysis as the best method to supply hydrogen [11-14].

A PEMEC consists of a catalyst-coated membrane sandwiched between anode and cathode electrodes. Each electrode includes a catalyst layer (CL), a liquid/gas diffusion layer (LGDL), and a bipolar plate (BP), which also acts as the current distributor (CD) and the

flow field. All components are fastened by two end plates by eight bolts. When a sufficient electrical current is applied, water decomposes to oxygen, protons, and electrons at the anode reaction site. Protons pass through the membrane, which is typically made of Nafion, to the cathode and react with electrons, supplied by the external circuit, to form hydrogen. By combining single cells, a PEMEC stack can supply huge amounts of hydrogen and oxygen that can be stored for later use.

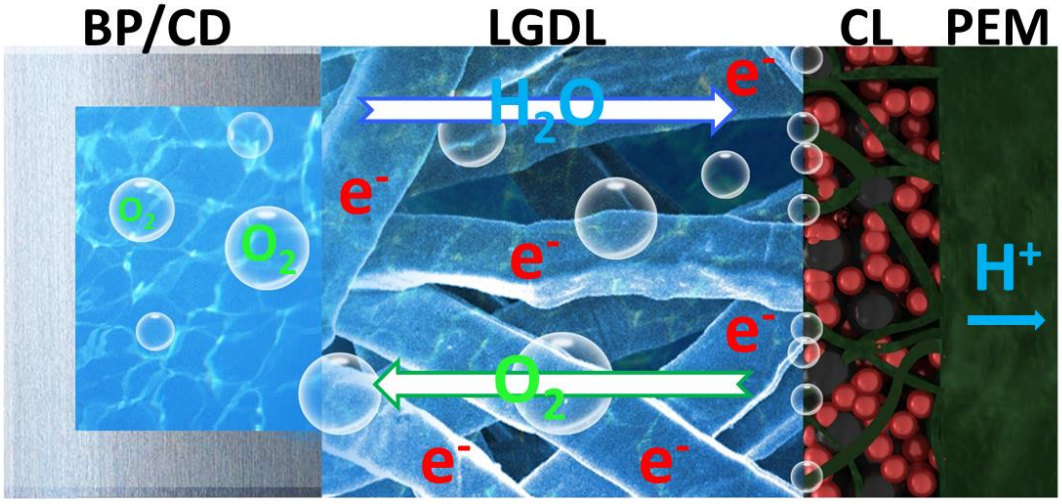


Figure 3.1. Schematic of the functions of LGDL at anode of PEMECs.

One of key challenges for current PEMECs is to improve the performance and cost efficiency with the most suitable LGDLs, which are located between the catalyst layers (CLs) and the bipolar plate (BP)/current distributor (CD) in a PEMEC, as shown in Figure 3.1. The LGDLs are expected to transport reactants, electrons, heat, and products, with minimum voltage, current, thermal, interfacial, and fluidic losses [8, 20, 68-72]. The LGDL

has to meet the following challenges: (1) Reactant permeability: provide reactant water access effectively from flow channels to catalyst layers; (2) Product permeability: provide flow pathways for H_2/O_2 from catalyst-layer area to flow channels; (3) Electronic conductivity: provide electrons to all reaction sites; (4) Thermal conductivity: provide efficient heat transport and uniform heat distribution; and (5) Interfacial and mechanical properties: provide high corrosion resistance and good contacts (i.e., good interfacial electrical and thermal conductivity) with the adjacent materials/parts (BP/CD and CL), and maintain small pressure drops in the flow channel. Thus, effective LGDLs will promote a uniform current/thermal distribution at the adjacent reaction sites.

Carbon materials (carbon paper or carbon cloth), which are typically used in PEM fuel cells (PEMFCs), are unsuitable for PEMECs due to the high potential of the oxygen electrode [73-81]. Metallic LGDLS and bipolar plates have attracted more interest in both PEMECs and PEMFCs due to their high conductivity, rapid production, and low cost [22, 42-45]. By taking advantage of novel designs and advanced fabrication methods, a thin-film metallic LGDL with well-controlled pore morphologies and surface properties demonstrated good functionality and water management in PEMFCs [42, 46, 82]. However, since material corrosion and consumption will result in poor interfacial contacts, degrading the PEMEC performance and efficiency, metallic LGDLs with higher corrosion resistance are strongly desired.

Titanium has received considerable attention as a promising structural/functional material in aerospace, marine, nuclear, electronics, medical implants, and instruments due to its high corrosion resistance even at high positive overpotential as well as in highly acidic and humid conditions; however, difficulty in the machining of titanium and its cost have been

limiting factors for its widespread application. With the development of additive manufacturing (AM) technology, which has the advantages of high precision, complex geometry capability, good repeatability, tooling-free, low-cost, and rapid batch production, several fabrication solutions for multifunctional and well-tunable LGDLs have become possible [83-85]. The electron beam melting (EBM) technology, which was commercialized by Arcam AB Corporation about 15 years ago, has greatly enhanced the AM capabilities by taking advantage of precisely-controlled and high-energy electron heating sources.

The EBM process can be utilized to fabricate complex microstructures not possible through conventional AM methods. Its well-controllable process parameter window coupled with layer-by-layer fine powders offers a significant flexibility in designing parameters for various materials with complex internal microstructures and network. The EBM process has been explored previously for use in medical applications where non-stochastic mesh structures have been explored to mimic the mechanical response of bone. In addition, the mesh structure can also be altered to maximize the amount of bone adhesion when implanted in the body [86-94]. To authors' knowledge, the EBM additive manufacturing of titanium-based components of PEMFCs/PEMECs has seldom been publicly reported [95]. In this study, a titanium porous medium with controllable thickness and pore morphology was first developed with the EBM additive manufacturing for its application in PEMECs.

3.2 Materials and methods

A PEMEC was designed and fabricated in lab to conduct the experiments. It mainly consists of two endplates made from commercial grade aluminum and designed to provide

even compression pressure on the cell. In order to apply a current to the cell, a copper plate was inserted at the cathode as a current distributor. The cathode bipolar plate was fabricated from graphite and used a parallel flow field. The anode bipolar plate was fabricated from grade 2 titanium, and used a parallel flow field to distribute the flow over the active area of the cell. The titanium plate also has a function as the current distributor, as shown in Figure 3.2. In an attempt to maintain even compression and prevent leakage, gaskets for the LGDLs were fabricated from polyvinyl chloride (PVC). The cell was compressed by eight evenly distributed bolts, which were tightened to 4.52 N·m of torque during assembly. It has been verified by testing that the interfacial contact is good enough under this torque, further increasing the assemble torque won't reduce the total ohmic resistance. The electrolyzer had an active area of 5 cm^2 and was operated at room temperature.

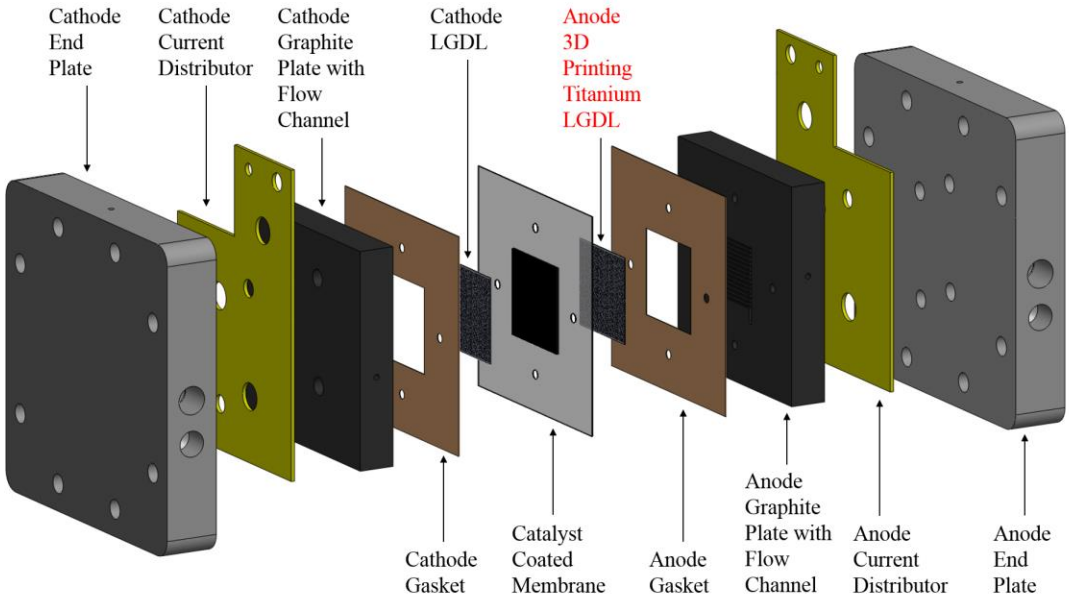


Figure 3.2. Schematic of a PEMEC with a LGDL of EBM Ti-6Al-4V mesh.

Testing Apparatus

The PEMEC was attached to an electrolyzer control system with a power supply of a current range up to 100 A and a voltage range up to 5 V. The hardware was connected to a Bio-Logic potentiostat controlled by EC-Lab, an electrochemical analysis software from Bio-Logic, which was used to evaluate performance and electrochemical impedance spectroscopy (EIS). For controlling the flow, a system of piping was connected to the PEMEC. While the cathode piping was merely intended to safely exhaust hydrogen gas that formed during electrolysis of water, a diaphragm liquid pump from KNF Neuberger was used to supply deionized water at a constant volumetric flow rate of 40 ml/min to the anode.

X-Ray Diffraction

The characterization of material structure and phase identification was carried out via x-ray diffraction (XRD) with a Philips X'Pert materials research diffractometer (45 kV, 40 mA), controlled by PANalytical's XRD software, in Bragg Brentano reflection geometry with Cu Kα radiation (λ=1.5418 Å) and a 2θ scan from 30° to 80° (with 0.01° steps for 5 s). The diffraction patterns are analyzed by the software MDI Jade9.

Scanning Electron Microscopy

The morphological characteristics of the liquid/gas diffusion layers and catalyst-coated membranes used in the experiments were observed using a field emission SEM. The SEM equipment used in the characterization is JEOL JSM-6320F with an accelerating voltage of 0.5-30 kV, a magnification range of 500x up to 650,000x, and a 5-axis specimen mount. The working distance ranged from 25 mm to 6 mm. Images were captured, processed, and analyzed by TEAM software.

Performance Testing

For performance evaluation, an increasing current density was applied to the PEMEC over a period of time. The current was stepped up from a current density of 0.2 A/cm^2 to 2.0 A/cm^2. At each current density, the potential of the cell was measured for five minutes before incrementing the current density again. Five minutes was chosen as an acceptable amount of time at each current density as it was empirically observed that the cell potential remained stable after this length of time.

Electrochemical Impedance Spectroscopy

Galvanostatic electrochemical impedance spectroscopy (GEIS) was used for measuring the impedance of the PEMEC at different operating conditions. In this method, the current is controlled as opposed to the potential. The test station is equipped with an operating current range of -100A to +100A and a voltage range of 0V to 5V. The current precision was 100 fA. The scanning frequency was varied from 10 kHz to 5 mHz, and recorded six points of data per decade. For analyzing impedance data, a Nyquist plot is normally used. There are normally two characteristic arcs in a typical Nyquist plot of the impedance of a PEMEC, which split the graph into three distinct ranges of high, medium, and low frequency. The leftmost x-intercept represents the ohmic losses of the PEMEC, and is generally measured for frequencies of a few kHz. The medium frequency range encompasses activation and charge-transfer losses in the electrolyzer, and has a characteristic frequency located in the local minima between the two arcs, and can range from 1 to a few hundred Hz. The low frequency region represents the mass-transfer losses in the PEMEC, and is at frequencies below 1 Hz.

3D Printer

The electron beam melting technology, developed by Arcam AB, is a powder bed additive manufacturing technology in which titanium powder materials are spread into a 50-µm thick layer and subsequently melted by a focused electron beam. The geometry of the melted region is determined by the 2-dimensional cross section of a 3-dimensional component. Successive layers are built on top of a stainless steel substrate in order to fabricate a 3-dimensional component. The powder used in the process, Ti-6Al-4V, is a heavily used aerospace and biomedical alloy. The powder particle size distribution was 45 µm to 105 µm and was plasma atomized powder supplied by Arcam AB. The samples were fabricated on an Arcam electron beam melting Q10 machine using software version 4.1.47. Because the melted area of the cross section is below a certain size threshold the entire structure is melted only with the contour melt theme and no bulk filling of the structure occurs. This results in the entire structure being melted as a series of spots along the contour of the stereo lithography (.stl) file. The outer contour is melted at 4.5 mA and the inner contour is melted using 8 mA. The standard focus values for this software version were used, and the resulting spot size of the electron beam is estimated to be on the order of 100-150 µm. Using these processing parameters resulted in a minimum wall thickness on the order of 100s µm.

Finer structures may be obtainable through optimizing the processing parameters; however, preliminary work on this has indicated this may lead to porosity in the wall. The size and shape of the unit cell determines the final geometry of the component fabricated. The process has been explored previously for use in medical applications where non-stochastic mesh structures have been explored to mimic the mechanical response of bone, and the

mesh structure can also be altered to maximize the amount of bone adhesion when implanted in the body.[86-90] For this particular study, a non-stochastic grid of various sizes was utilized with identical cross section in the vertical build direction.

3.3 Results and discussion

Before *in-situ* testing, the titanium LGDL samples from the 3D printer were characterized with SEM and XRD. Figure 3.3 shows typical images of an additively manufactured titanium LGDL, which has a thickness of 300 μm, a square pore size of 1.5 mm, and a pore-wall width of 500 μm. It should be noted here that the pore-wall width, pore size and pore distribution can be easily changed by altering the design parameters of the models, and/or varying fabrication conditions and powder sizes, thus obtaining expected porosities. In the high-resolution images shown in Figure 3.3(B) and Figure 3.3 (C), the titanium powder can be clearly observed at the side walls of the pores. The top and bottom surfaces are smooth and flat with uniform thickness, which markedly improves the contact interface thereby reducing the contact resistance between the LGDL and catalyst layer. These features significantly distinguish the 3D printed LGDL from woven or welded LGDLs, as shown in Figure 3.4. The wires crimp on both sides and are locked together at the wire joints for stability.

The XRD patterns of the EBM Ti-6Al-4V LGDL are shown in Figure 3.5, which show titanium crystalline nature with 2θ peaks lying at 35.09^{o} (100), 38.42^{o} (002), 40.17^{o} (101), 53.00^{o} (102), 62.95^{o} (110), 70.66^{o} (103), 76.22^{o} (112), and 77.37^{o} (201). All the peaks in the XRD patterns can be indexed as hexagonal alpha phases of titanium and the diffraction data is in strong agreement with Joint Committee on Powder Diffraction Standards (JCPDS) files # 44-1294 and reference.[96] Crystallite size can also be obtained based on the

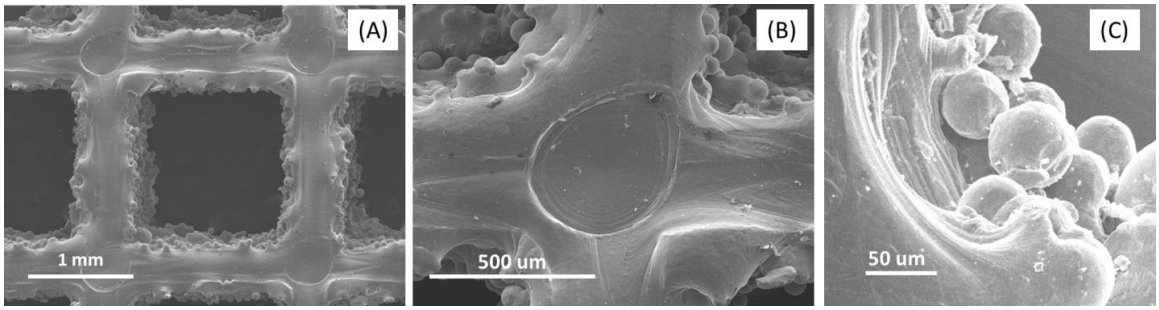


Figure 3.3. Images of an EBM Ti-6Al-4V mesh LGDL at different scales.

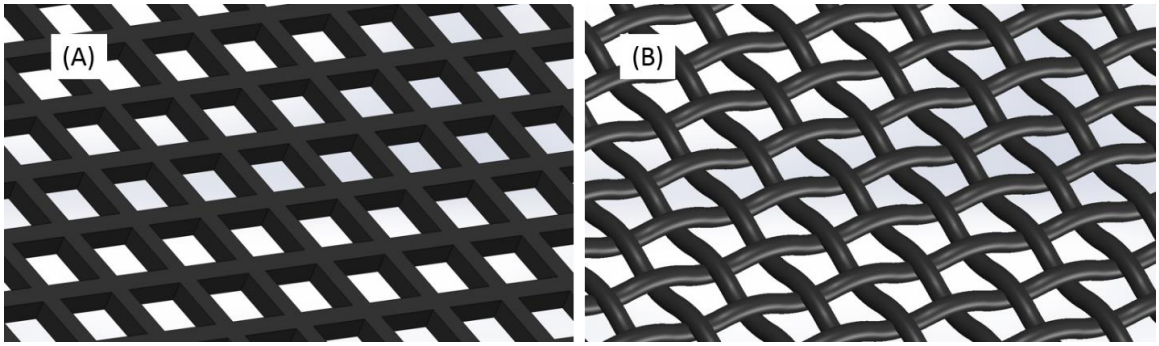


Figure 3.4. Schematic of LGDLs with different fabrication method, (A) EBM Ti-6Al-4V mesh, (B) woven mesh.

Scherrer equation (7):

$$\tau = \frac{K\lambda}{\beta cos\theta} \qquad (7)$$

Where τ is the crystal size; λ is the wavelength of the X-ray radiation (λ=0.15406 nm) for CuKα; K is usually taken as 0.9; and β is the line width at half-maximum height. The crystallite sizes obtained using this formula are from 18 to 32 nm.

In the PEMEC tests, EBM Ti-6Al-4V LGDLs were used at the anode and Toray 090 carbon paper treated with 5% PTFE was used as the cathode LGDL. For comparison, titanium woven mesh, which has similar wire thickness and porosity, was chosen to serve as a reference LGDL. Similar to EBM Ti-6Al-4V structures, woven meshes were used as the anode gas diffusion layer, and were tested in the same PEMEC and operating conditions. The effect of the LGDL with different fabrication process and structure at the anode on the PEMEC performance at room temperature is shown in Figure 3.6. The operation voltages for both LGDLs were increased linearly with current densities from 0.2 A/cm^2 to 2.0 A/cm^2, where ohmic losses limit performance. Better performance (lower voltage) was obtained with EBM Ti-6Al-4V LGDL. At 1.5 A/cm^2, the operating voltage decreased from 2.49 V to 2.18 V, corresponding to more than 12% of an efficiency improvement.

For a better understanding of the performance data, GEIS testing was conducted *in-situ* with both titanium woven and EBM Ti-6Al-4V LGDLs. Figure 3.7 shows the Nyquist plots of the impedances with EBM Ti-6Al-4V LGDLs and Ti woven LGDLs under the current density of 2 A/cm^2 at room temperature. The scanning frequency was from 10 kHz to 5 mHz, and recorded six points of data per decade. The ohmic loss, which was derived from their leftmost x-intercepts at a high frequency range, was significantly decreased from 0.47

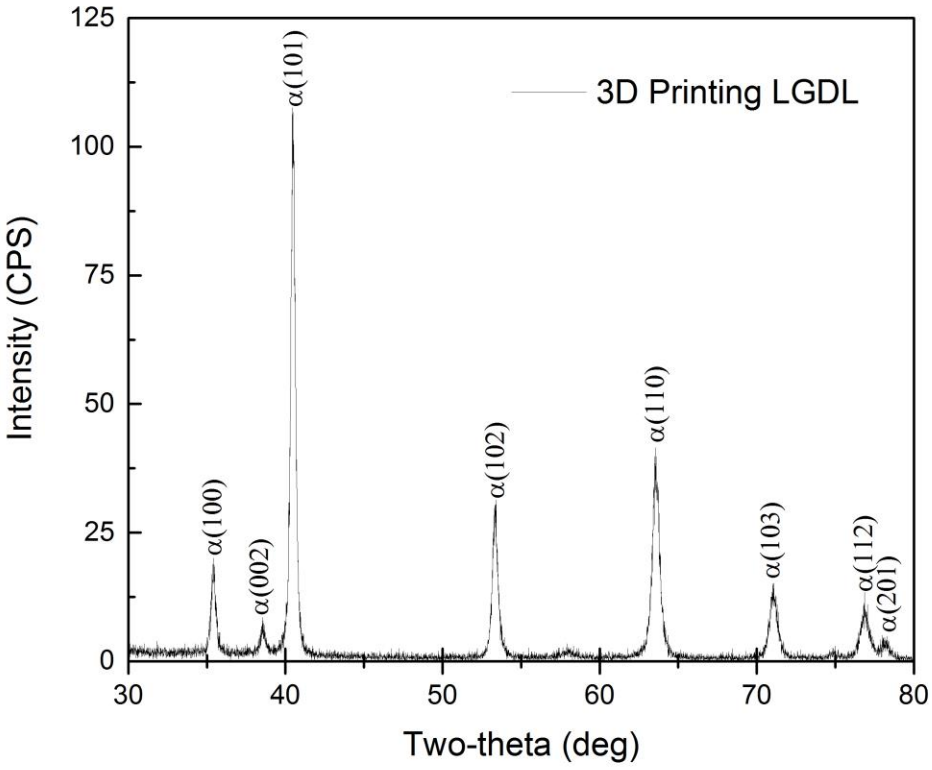


Figure 3.5. XRD Pattern of the EBM Ti-6Al-4V mesh LGDL.

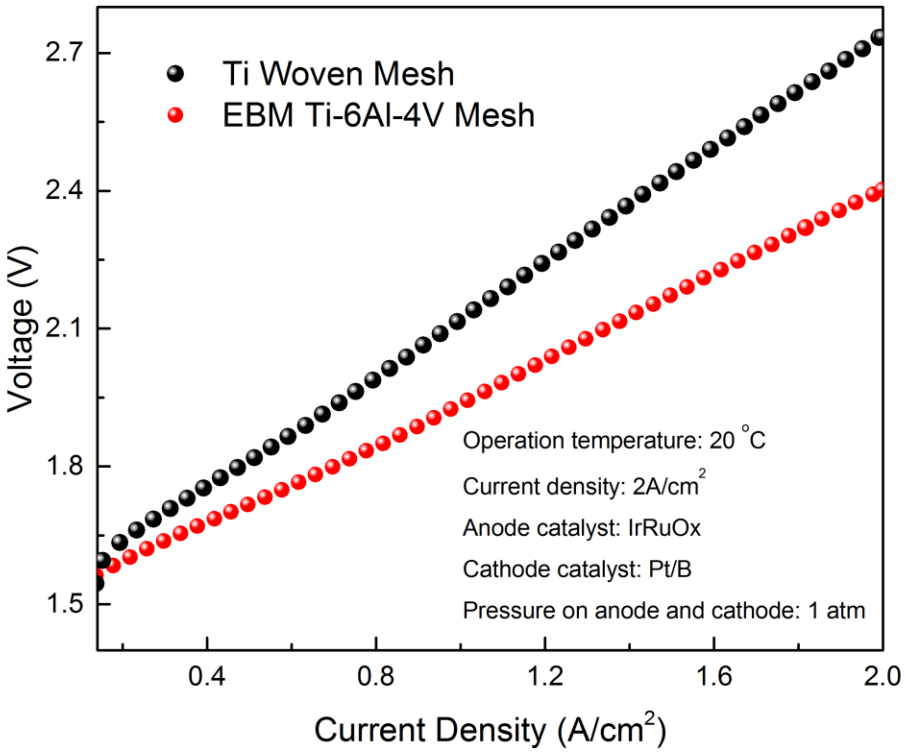


Figure 3.6. Performance curves of PEMEC with an anode LGDL of an EBM Ti-6Al-4V mesh and a Ti woven mesh at room temperature.

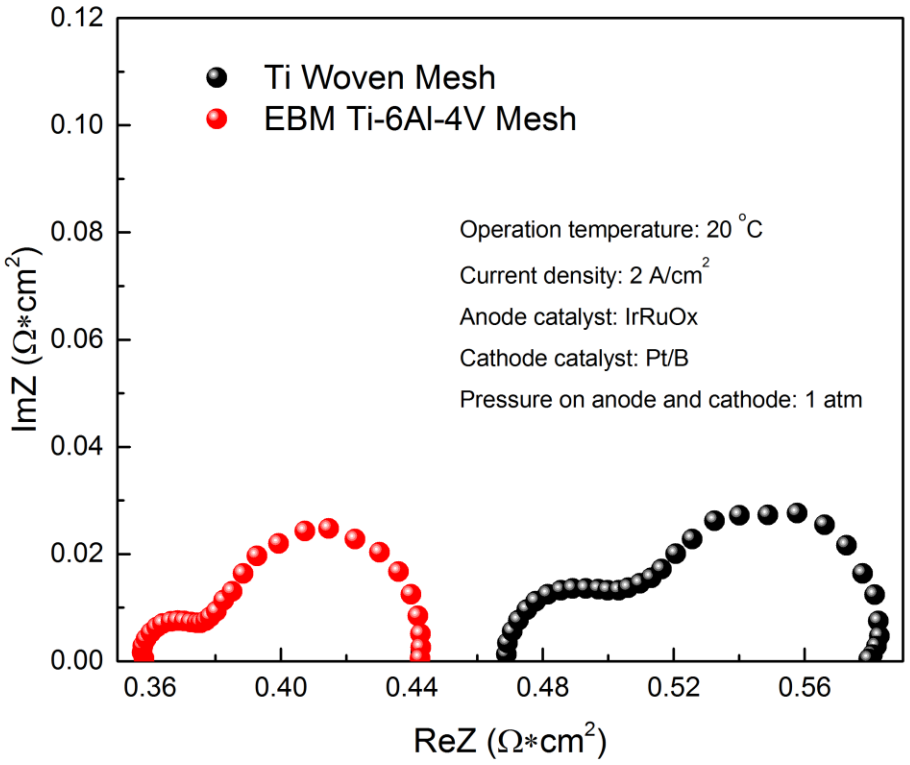


Figure 3.7. GEIS curves of PEMEC with an anode LGDL of an EBM Ti-6Al-4V mesh and a Ti woven mesh under the current density of 2 A/cm^2 at room temperature.

$\Omega \cdot cm^2$ to 0.36 $\Omega \cdot cm^2$ with woven mesh and EBM Ti-6Al-4V LGDLs respectively. This phenomenon can be explained by the distinct structures and morphologies between two meshes. With the flat and in-plane surface, the EBM Ti-6Al-4V printing LGDL provides a better contact with both current distributors and catalyst coated membranes (CCMs), as shown in Figure 3.3 and Figure 3.4, which significantly decrease the contact resistance, thus making the ohmic loss less than woven meshes.

The PEMEC performance was further enhanced at higher operating temperatures, as shown in Figure 3.8. The cell temperature is varied from 35 to 65 ^oC at a step of 15 ^oC, which is within the general operating temperature region in the PEMEC system [20]. At 1.5 A/cm^2, the operating voltage needed was decreased from 2.13V, 2.02 V to 1.91 V, respectively, which indicated a significant performance improvement. Higher temperature in PEMECs promotes improved kinetics and interfacial contacts, enhances the proton conductivity inside the membrane, and enhances the diffusion of reactants while decreasing the concentration difference [14, 24, 68].

As shown in Figure 3.9, the GEIS results indicated that the ohmic loss reduced remarkably along with the increasing of cell temperature. At 35 ^oC, its ohmic loss was about 0.33 $\Omega \cdot cm^2$, while at higher temperature of 65 ^oC, it was reduced to 0.21 $\Omega \cdot cm^2$, which lead to a lower voltage (better performance). The major impact on the ohmic loss is the change of interfacial contact resistance along with the increasing of operation temperature. The higher operation temperature will expand the components inside the PEMEC, tighten the components and then reduce the interfacial contact resistance, which can't be achieved by increasing the torque of fasten bolts as aforementioned.

It has been shown that ohmic losses play a dominant role in PEMEC performance, and its

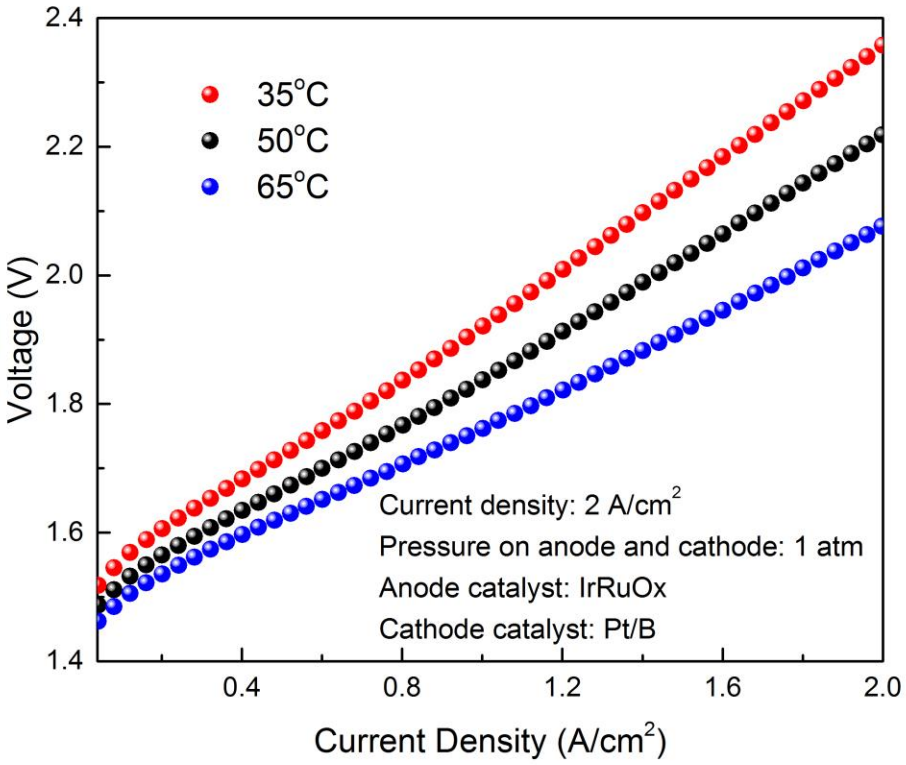


Figure 3.8. Performance results of a PEMEC with anode LGDL of an EBM Ti-6Al-4V mesh at different temperatures.

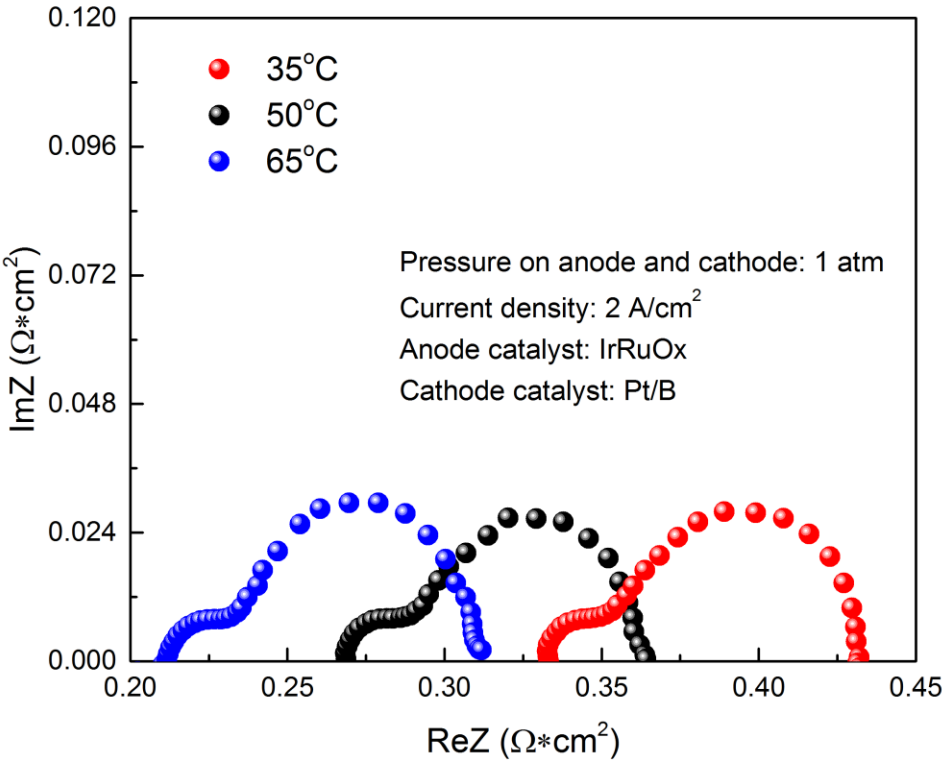


Figure 3.9. GEIS results of a PEMEC with an anode LGDL of EBM Ti-6Al-4V mesh at different temperatures.

reduction will directly result in lowering the operating voltage of the PEMEC, thus promoting performance and efficiency. With EBM Ti-6Al-4V technology, LGDLs with different pore morphologies and structures, including pore size, shape, wall thickness, and porosity can be easily manufactured for further reducing the ohmic resistance and enhancing performance in a PEMEC.

3.4 Conclusion

A novel low-cost technique of the electron beam melting (EBM) additive manufacturing for fabricating titanium liquid/gas diffusion media with high-corrosion resistance and well-tunable multifunctional parameters, including two-phase transport and improved electric/thermal conductivities, has been demonstrated for the first time. Their applications in proton exchange membrane electrolyzer cells have been explored. By taking advantage of the additive manufacturing, the EBM technology makes it possible to fabricate a three-dimensional and complicated object of virtually any shape from a digital model faster, cheaper, and easier than conventional methods, especially for titanium. In addition, compared with conventional woven LGDLs, increased performance and efficiency of up to 8% at room temperature with EBM Ti-6Al-4V LGDLs is obtained due to their significant reduction of ohmic losses. More importantly, this process can enable manufacturing of LGDLs with control of pore size, pore shape, pore distribution, and therefore porosity and permeability, which will be valuable in developing sophisticated PEMEC models, which will in turn allow the optimization of the LGDL for maximum performance. Further, it will lead to a manufacturing solution to couple the LGDLs with other parts, since they can be easily integrated together with this advanced manufacturing

process. Further optimal investigations and improvements of the EBM Ti-6Al-4V LGDLs and other components are underway.

CHAPTER 4

TITANIUM THIN/WELL TUNABLE LIQUID/GAS DIFFUSION LAYER

4.1 Introduction

Clean and sustainable energy sources are becoming increasingly attractive. Hydrogen fuel is a proven fuel source for clean energy and propulsion, which can be generated from low temperature water electrolysis and is currently undergoing rapid advancement. A proton exchange membrane electrolyzer cell (PEMEC) is an advanced, reverse PEM fuel cell (PEMFC), and is a key component of an effective energy storage solution that produces both hydrogen and oxygen from water. This is mainly due to its distinguished efficiency, high energy density, compact design, large capacity, and ability to use electricity from other renewable energy sources [13, 14, 18, 65, 97-104]. PEMECs are robust and may be coupled with PEMFCs in order to create highly efficient regenerative energy systems [2, 8, 70, 100]. A PEMEC mainly consists of a catalyst-coated membrane (CCM) sandwiched by two electrodes. At the anode, water is circulated through a flow field to the membrane electrode assembly (MEA) where it electrochemically reacts and is split into oxygen and protons. The protons are then transported through the membrane, react with electrons from an external electrical force, and form hydrogen gas at the cathode, which exits through the flow channel. Meanwhile, the oxygen is transported along with the water out of the anode. In the PEMEC as shown in Figure 4.1 [105], a liquid/gas diffusion layer (LGDL) is located between the catalyst layer and the current distributor, which also acts as the flow field. Its functions are to transport electrons, heat, and reactants or products to and from the catalyst

layer with minimal voltage, current, thermal, interfacial, and fluidic losses [106-116]. To meet these requirements, the LGDL should provide:

- Simultaneous reactant/product permeability: reactant water access effectively from flow channels to catalyst layers, and products of H_2/O_2 from catalyst-layer area to flow channels, respectively;
- Electronic and thermal conductivity: allow electrons to all reaction sites and efficient heat transport and uniform heat distribution;
- Interfacial and mechanical ability: provide high corrosion resistance and excellent contacts with the adjacent materials/parts (bipolar plate, current distributor and catalyst layer), and maintain small pressure drops in the flow channel.

Carbon-based materials (carbon paper, or carbon cloth), which are typically used in PEMFCs [6, 73-79, 117], are unsuitable for PEMECs due to their high ohmic potential and the highly oxidative environment of the oxygen-rich electrode [13, 80]. The corrosion and consumption of the carbon will degrade the LGDL and result in poor interfacial contacts, which will decrease the performance and efficiency of the PEMEC. In order to counteract this effect, materials with high-corrosion resistance have been sought. One such material with desirable properties for use as the LGDL in the anode of a PEMEC is titanium [65], which is a highly promising structural/functional material in aerospace, marine, nuclear, electronics, medical implements, implants and instruments due to its high corrosion resistance even at high positive overpotential, even in highly acidic and humid conditions. In addition, it provides high thermal/electrical conductivities and excellent mechanical properties. Currently, titanium meshes/felts/foams are mainly utilized as LGDLs at the PEMEC anode side. Its thickness is larger than 300 μm with significant electrical

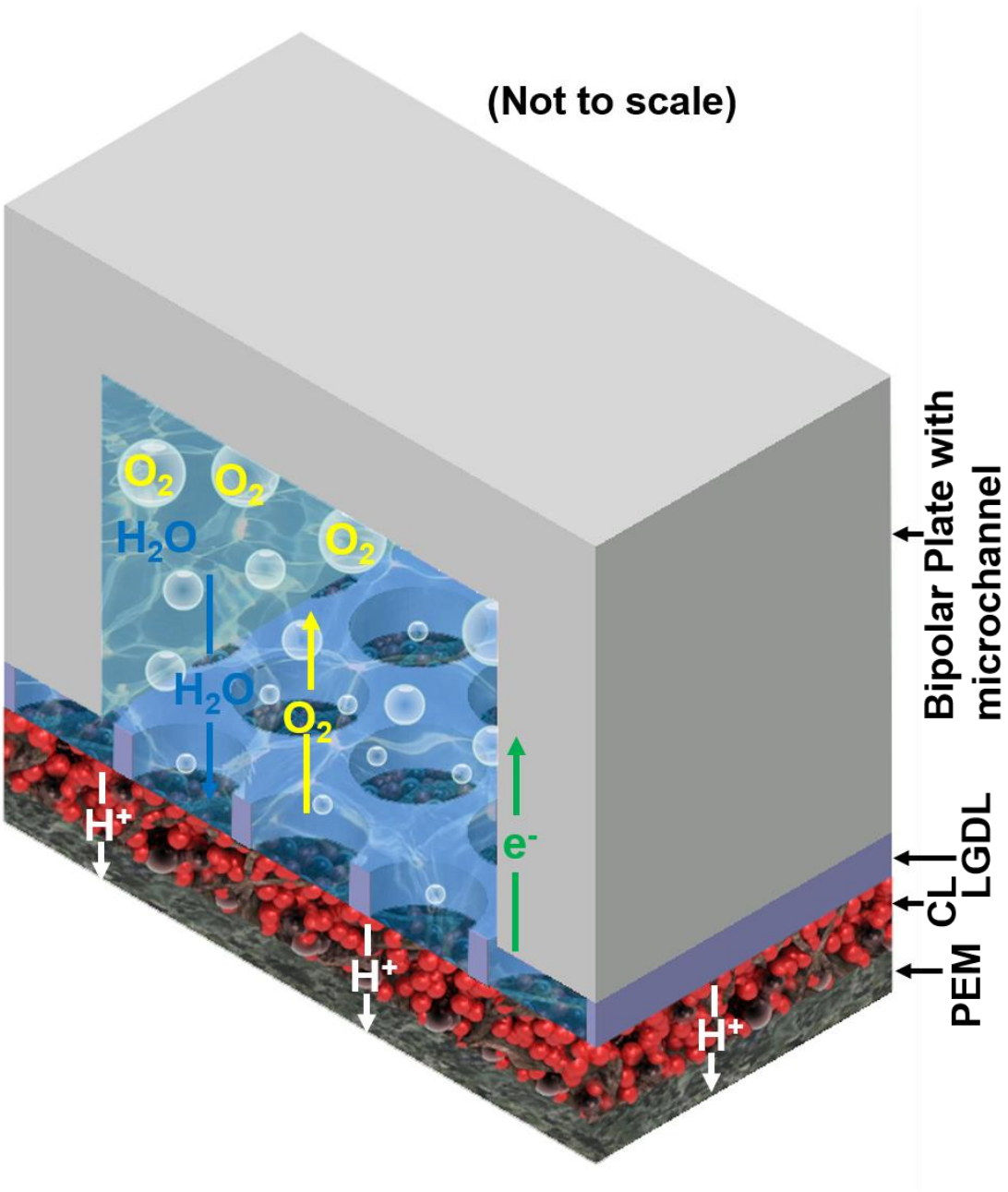


Figure 4.1. Schematic of LGDL functions at the anode of PEMECs.

conductive path and fluidic resistance. In addition, their random structures make it impossible to control the water/electron/thermal distribution and their complicated pore morphology results in unusual interfacial contact resistance.

With the development of micro/nanotechnology, which has the advantages of high precision, good repeatability, and repeatable batch-production, several solutions for improved thermal and electrical conductivity, mass transport, and permeability will become possible. In this study, a new titanium, thin, LGDL with well-tunable pore morphologies is developed using micro/nano-manufacturing. Both experimental evaluations of the electropotential performance and electrochemical impedance are conducted with this new LGDL, and the test results are compared with a conventional LGDL. It has been demonstrated that thin LGDLs remarkably reduce the ohmic, interfacial and transport losses, and achieve a superior multifunctional performance. Prospects for future LGDL development and optimization in PEMEC are also discussed.

4.2 Materials and methods

4.2.1 Nano-manufacturing of titanium thin/well-tunable LGDLs

Although, titanium has a lot of advantage to be chosen as raw material for LGDL, such as high corrosion resistance, excellent electric conductivity and good mechanical properties, etc. It's difficult to fabricate part with titanium material. 3D printing is capable to fabricate LGDL with the material of titanium for prototype, however, it is still expensive and slow for commercial application [105]. Photochemical machining thin titanium foils seams the most efficient way to mass produce the titanium thin/well-tunable LGDLs. The titanium thin/well-tunable LGDLs are manufactured using lithographically patterned resist masks and chemical wet etching of thin foils [82]. A typical fabrication procedure for titanium

thin LGDL begins with the design and fabrication of the photomasks. A mask pattern was designed using commercially available CAD/VLSI software (LayoutEditor, layouteditor.net). The design pattern was imported into a Heidelberg DWL 66 laser lithography system and patterned on a soda-lime glass mask plate that is precoated with chromium and photoresist. After patterning, the masks were developed for 1 minute in Microposit® MF® CD-26 Developer (Shipley Company, Marlborough, MA), rinsed with DI water and dried with N_2. Masks were then submerged in chrome etchant for 2 minutes, rinsed with DI water and dried with N_2. The remaining resist was subsequently removed in a heated bath (70oC) of N-Methyl Pyrolidone (NMP). Masks were rinsed with DI water and dried with N_2. As shown in Figure 4.2, in order to provide structural integrity of the extremely thin titanium foil, foils were affixed to a silicon wafer during processing. Substrate were treated with Microprime P20 Primer (Shin-Etsu MicroSi, Inc., Phoenix, AZ) adhesion promoter by coating the substrate with adhesion promoter, waiting for 10 seconds and spin-drying the samples at 3000 RPM for 45 seconds. Subsequently Microposit SPR220 photoresist (Rohm and Haas, Marlborough, MA) was spin-coated onto samples at 3000 RPM for 45 seconds. The titanium film was then placed on the resist coated silicon wafer with special care due to its delicate features, and soft baked for 90 s at 115 ^{o}C. A second layer of P20 and SPR220 photoresist was applied to the titanium foil under identical conditions, and then exposed to UV light using conventional contact photolithography. Developed in Microposit® MF® CD-26 Developer (Shipley Company, Marlborough, MA), rinsed with DI water and dried with N_2. Finally, after patterning the photoresist mask on the foil, the patterned material was etched in HF etchant.

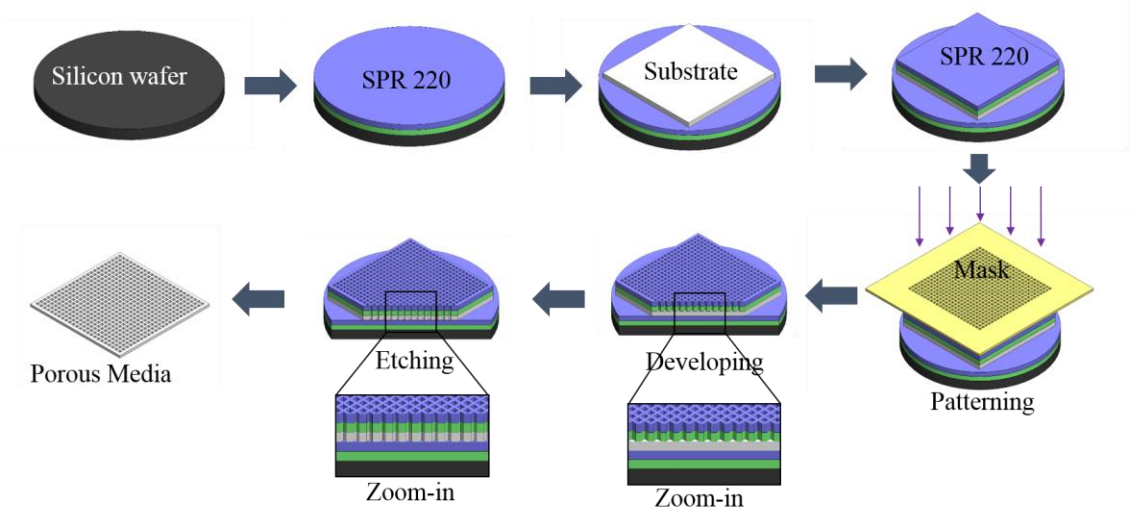


Figure 4.2. Typical wet etching fabrication process for titanium thin LGDLs.

4.2.2 Test system and *in-situ* characterizations

A standard PEMEC was used for conducting the designed experiments. It consists of two endplates made from commercial grade aluminum and designed to provide even compression on the cell. In order to apply a current to the cell, a copper plate was inserted at the cathode as a current distributor. The bipolar plate was manufactured from graphite with a parallel flow field to distribute the flow over the active area of the cell. The catalyst-coated membrane is comprised of Nafion 115, a perfluorosulfonic polymer with a thickness of 125 µm, an anode catalyst layer with an IrRuOx catalyst loading of 3 mg/cm^2, and a cathode layer with a platinum black (PtB) catalyst loading of 3 mg/cm^2. The cell was compressed by eight evenly distributed bolts, which were tightened to 40 in-lb. of torque during assembly. The electrolyzer had an active area of 5 cm^2 and was operated at a temperature of 80 ^{o}C.

The PEMEC was connected to a modular postentiostat system with a current booster, which can operate under a current range of up to 100A and a voltage range of up to 5V. The hardware was connected to Bio-Logic software, EC-Lab, which was used to conduct performance testing and electrochemical impedance spectroscopy (EIS). For controlling the flow, a flow system was connected to the PEMEC. While the cathode tubing was merely intended to safely exhaust hydrogen gas that formed during electrolysis, the water was circulated through the anode of cell at a constant volumetric flow rate of 20 ml/min by a diaphragm liquid pump from KNF Neuberger.

For the performance evaluation, a constant current was applied to the PEMEC over a period of time, while the required voltage was measured. The current density was stepped up from 0 A/cm^2 to 2 A/cm^2. At each current density, the potential of the cell was measured for five minutes before incrementing the current density again. Five minutes was chosen as an acceptable amount of time, after which the cell potential remained start to stable while changed to a new current density.

Electrochemical Impedance Spectroscopy (EIS) was used for measuring the impedance of the PEMEC at different operating conditions. In this method, the current is controlled as opposed to the potential. It is equipped with an operating current of -100A – +100A and a voltage of 0V – 5V. The current precision was 100 fA. The scanning frequency was varied from 15 kHz to 10 mHz, and recorded 15 points of data per decade. For analyzing impedance data, a Nyquist plot is normally used.

4.2.3 *Ex-situ* characterizations

The ex-situ characterizations of LGDLs were performed with a Hitachi S-4800 FEG Scanning electron microscopy (SEM) equipped with a cold cathode field emission column

emitter. Ultra-high resolution and high image quality was obtained at low operating voltage ~1.4 nm at 1 KV (1 nm at 15 KV). It can be operated under a wide voltage range of 100V to 30 KV. It was employed to observe uncoated samples by beam deceleration option and used In-lens SE and BSE detection at low voltages. Samples were loaded into the instrument on AGAR scientific conductive carbon tabs. Images were obtained with acceleration voltages 15 kV and were collected by built in Quartz PCI image acquisition and processing software.

4.3 Results and discussion

4.3.1 *Ex-situ* characterization of titanium conventional and novel thin LGDLs

The morphological characteristics of the liquid/gas diffusion layers used in testing were characterized using a field emission SEM. Figure 4.3 details SEM images of conventional titanium felt and newly designed titanium thin LGDLs, respectively. The surface structures and pore morphologies between titanium felt LGDL and thin LGDL are obviously different. The titanium felt LGDL has a thickness of 350 µm with a fiber diameter of about 20 µm. Its average pore size and porosity are around 100 µm and 0.78, respectively. The felt LGDL shows random pore shapes and pore distributions. The new thin LGDL is manufactured from a titanium thin foil with a thickness of about 25 µm. Its pore size, pore shape, and pore distribution are well controlled. With flat surface feature, its pore size and porosity are 100 µm and 0.3, respectively.

4.3.2 PEMEC performance and efficiency

Both the new thin LGDL with well-tunable micro-pores and the conventional felt LGDL were tested in a standard PEMEC. They were applied as anode LGDLs, while the Toray 090 carbon papers were used at cathode sides in the PEMEC tests. The relationship

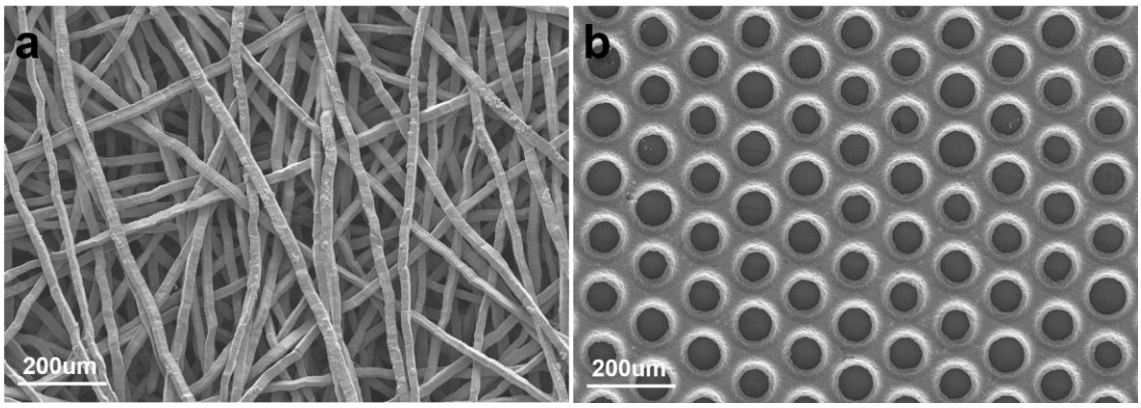


Figure 4.3. SEM Images of titanium conventional and thin LGDLs with similar pore size (a) titanium felt LGDL with average pore size of 100 µm and porosity of 0.78; (b) titanium thin LGDL with a pore size of 100 µm and porosity of 0.30.

between current density and voltage is a critical measure of the performance of the PEMEC, with lower voltage for a given current density indicating better performance. Figure 4.4 shows the PEMEC performance curves with both the thin/well tunable LGDL (red color), and conventional felt LGDL (black color) under the same operating conditions. The operating voltages needed for both LGDLs are increased with the current densities, while much lower voltages were needed for new thin LGDLs. At a current density of 2 A/cm^2, the needed votage is reduced from 1.88V with conventional titanium felt LGDL to 1.69V with new thin LGDL, which reaches the new-low among the recent publications[64, 99, 108, 118, 119].

The efficiency of the PEMEC, η, can be calculated as following equation (8),

$$\eta = \frac{V_{thermal}}{V_{cell}} \qquad (8)$$

where V_{cell} and $V_{thermal}$ are the PEMEC operating voltage and theoretical thermal voltage, respectively. Under the operating conditions with a temperature of 80°C and a pressure

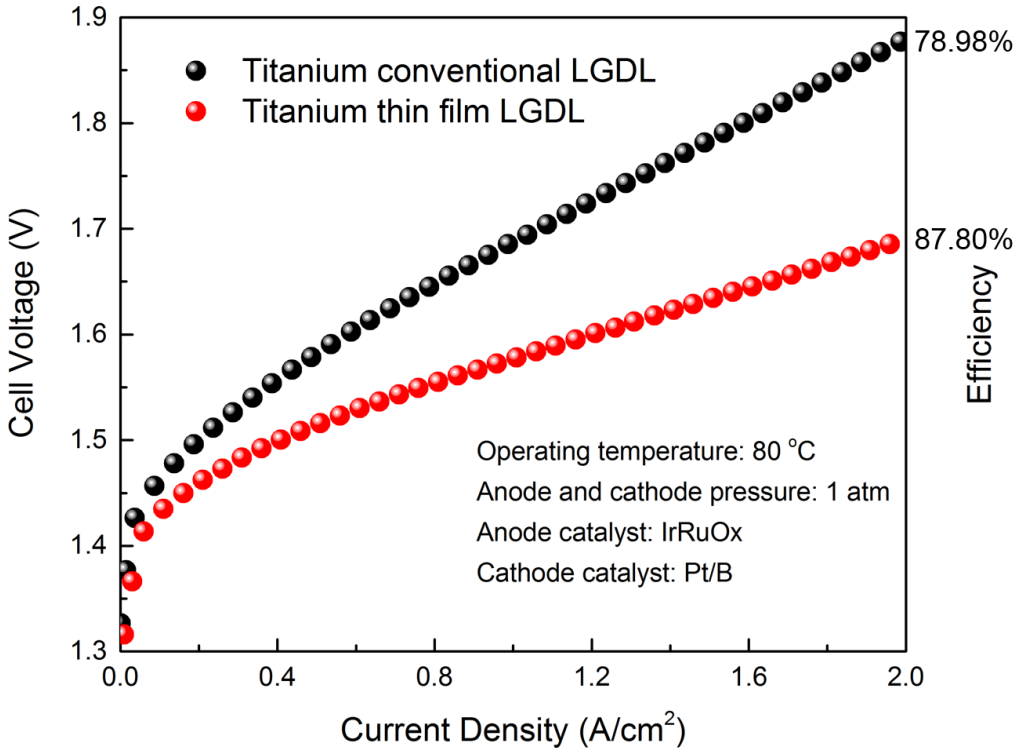


Figure 4.4. Performance comparisons of PEMEC with titanium thin LGDL and conventional LGDL (red colour: titanium thin/ well tunable LGDL with thickness of 25 µm, pore size of 100 µm and porosity of 0.30; black color: titanium felt LGDL with thickness of 350 µm, average pore size of 100 µm and porosity of 0.78).

of 1 atm, $V_{thermal}$ is about 1.4841V [120, 121]. As shown in Figure 4.4, at a current dencisyt of 2 A/cm^2, the PEMEC efficiency is increased from 78.98% with the titanium conventional felt LGDL to 87.80% with titanium thin/well tunable LGDL. The efficiency is much better than a recent report with a best efficiency of 82% [13].

4.3.3 Electrochemical impedance spectroscopy results

The EIS testing were *in-situ* conducted with both titanium conventional felt and new thin LGDLs. Figure 4.5 shows their EIS results at a fixed current density of 0.2 A/cm^2. Over the frequency range from 15 kHz to 10 mHz, there is one big arc. The high-frequency resistance, which mainly represents total ohmic resistance, is the leftmost intersection point of the arc with the real axis at the high-frequency end. It includes the ohmic resistances of all electrolyzer components, including bipolar plates, diffusion media, electrodes and membranes, and the associated interfacial resistances between them. As shown in Figure 4.5, the impedance representing total ohmic resistances significantly decrease from 0.1815 Ω·cm^2 with a conventional titanium felt LGDL of 350 μm thickness to 0.0758 Ω·cm^2 with a titanium thin LGDL of 25 μm thickness. These results show that a thicker titanium felt LGDL with complicated surface structures cause higher total ohmic losses, thus degrading the PEMEC performance, as shown in Figure 4.4. The new thin LGDL with simple flat surface results in great reduction of its associated ohmic resistances and interfacial resistances. The electronic resistance of bulk titanium felt and the nanomanufactured thin titanium film are 4.9 x 10^{-5} Ω and 2.7x10^{-8} Ω, respectively. Although the proton transport resistance through the membrane is difficult to estimate. The total resistance for each LGDL can be compared by EIS results. Between these two results, there is only anode LGDL have been changed in experiments. So the difference of total ohmic resistance only

come from the change from electronic resistances of the bulk titanium felt to nanomanufactured thin titanium film. While the contribution of performance improvement from the difference of electronic resistance between bulk titanium felt to nanomanufactured thin titanium film isn't enough, so it can assume that the major difference is coming from interfacial contact resistance. It has been indicated that the LGDL thickness and interfacial structures at a fixed material dominate the total ohmic resistance, thus playing crucial roles on PEMEC performance.

The thickness of novel designed titanium thin LGDL is much less than the conventional titanium felt LGDL, which definitely will reduce the ohmic resistance. More importantly, the surface structure of titanium thin LGDL and titanium felt LGDL are quite distinct. The titanium felt LGDL is made of titanium fibers, and its interfacial contacts with the catalyst layer and the bipolar plate (BP) is mainly due to curved surfaces of titanium fibers with plane surfaces of CLs and BPs. On the other hand, since the novel titanium thin LGDL is etched from a flat thin foil, its interfacial contacts with the catalyst layer and the bipolar plate are much improved due to the planar surfaces. Those plane-surface contacts significantly reduce the CL/LGDL/BP interfacial resistances, which dominate the total ohmic resistances in a PEMEC. This is the main reason that the total ohmic resistance with titanium thin LGDL is significantly reduced compared with the titanium felt LGDL, which agrees with the result of EIS test as shown in Figure 4.5.

Generally, in PEMECs, the electrochemical reactions occur mainly on the interfaces between LGDL and catalyst layer [122-125]. The functions of LGDL essentially consist of (1) conduct electrons between electrodes and current distributors, (2) transport liquid water from micro channels to reaction sites, and (3) allow diffusion of gaseous oxygen to the

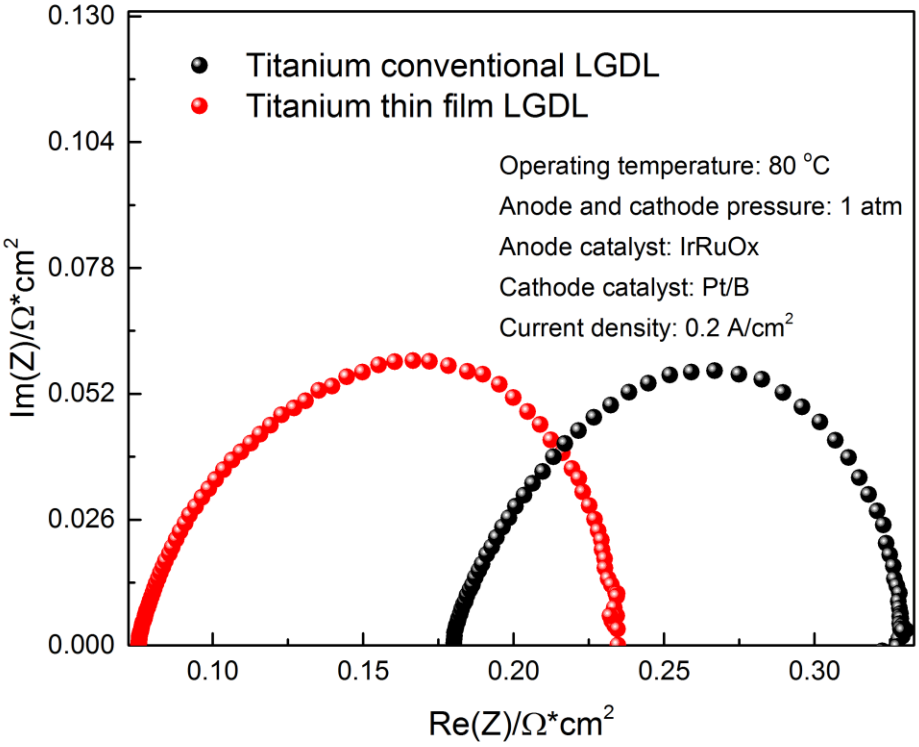


Figure 4.5. EIS comparisons of PEMEC with titanium thin etched LGDL and conventional LGDL (red colour: titanium thin/ well tunable LGDL with thickness of 25 µm, pore size of 100 µm and porosity of 0.30; black color: titanium felt LGDL with thickness of 350 µm, average pore size of 100 µm and porosity of 0.78).

flow channel. So the LGDL can be developed and optimized after considering those critical functions. With optimal designs of thickness, porosity and pore size, a better PEMEC performance can be achieved with thin structured LGDLs by taking advantage of well-tunable and straight-through micro-pores, while maintaining excellent properties for two phase flow in LGDLs. For conventional LGDL, such as titanium felt, the thickness is about 350 μm, and the mean pore size is about 100 μm, at this situation, the water need capillary pressure to get into the titanium felt LGDL and reach the interface of LGDL and catalyst layer, which is the reaction sites. For nano-manufacturing thin titanium LGDL, the pore size is still 100 μm while the thickness is about 25 μm, and the pore is throughout straight one. Under this situation, the water is easy to get into the LGDL and reach the reaction sites, and the oxygen is easy to get out of the LGDL. As shown in Figure 4.4 and Figure 4.5, the PEMEC with titanium thin film LGDL has less overpotential at activation, ohmic and mass transport states. Activation loss refer to the activation energy to transfer an electron from an electrode to anode electrolyte. So the interface between anode electrode and electrolyte can affect the activation loss, which make the performance difference in the activation dominant region. In this study, the anode LGDL is difference structure, which will cause the different interface between anode electrode and electrolyte. A total ohmic resistance reduction of LGDL will make it possible to decrease the PEMEC operating voltage and enhance its performance. In addition, with LGDL straight-through micro-pore features, precise controls of pore size, pore shape, pore distribution, and therefore porosity and permeability, can be easily produced based on advanced manufacturing [126]. This development will also lead to reducing the cost, volume, and weight of the LGDL itself and the whole system.

4.4 Conclusion

Titanium thin and well-tunable liquid/gas diffusion layers (LGDLs) with flat interfacial surfaces are developed and are introduced into a PEMEC for the first time, and exhibit superior multifunctional performance over conventional LGDLs. Based on the electropotential performance tests, the operating voltages at a current density of 2.0 A/cm^2 were as low as 1.69 V with an efficiency of up to 87.80%. In order to gain better understanding the mechanisms, both the *ex-situ* and *in-situ* characterizations were conducted and they showed the thin and well-tunable LGDL with flat surface features remarkably reduced its total resistances, and significantly promoted the PEMEC performance and efficiency by over 9%. It has also been shown that the total ohmic resistance plays a dominant role in the PEMFC performance, and a better efficiency can be obtained by reducing the LGDL thickness and further enhancing interfacial contacts between LGDLs with other components. In addition, the LGDL thickness reduction from 300 μm of conventional LGDLs to 25 μm will greatly decrease the weight and volume of PEMEC stacks, which can lead to new directions for future developments of low-cost PEMECs with high performance. Its well-tunable features, including pore size, pore shape, pore distribution, and thus porosity and permeability, will be very valuable to develop PEMEC modeling and to validate simulations of PEMECs with optimal and repeatable performance.

CHAPTER 5

MECHANISM OF ELECTROCHEMICAL REACTION IN PEMECs

5.1 Introduction

The demand for power has increased rapidly over the past decades, due to economic growth, population expansion, and industrialization of developing countries worldwide. Meeting this demand can be difficult and often result in high levels of pollutions and greenhouse gases (GHG) emissions, creating serious health and environmental concerns and elevating indirect cost on society. Industry, such as power generation, manufacturing and transportation, often rely on non-renewable resources that stress the energy grid and accelerating the pollution of atmosphere. To combat this issue, there's been a shift to employ renewable technology, a superior method energy generation from nature resources, such as hydro, wind and solar. Renewables are well suited for diverse of energy demands and various industries by providing sustainable, clean and efficiency energy. Free of harm for pollution or GHG emissions. However, intermittent power disruptions are common with dealing with renewable resources. This occurs where there is mismatch between the supplier energy generated and consumption demanded. Energy storage eases intermittent power disruptions by store excess power generated by renewable resources at the time of low demand and distributing the power at the periods of heightened demand. This helps balance the load on energy created and reduce rely on nonrenewable resources. Hydrogen, as a high energy density and environmentally friendly fuel, is expected to be one of the most promising energy carriers in the near future [1-4]. Water electrolysis, a carbon free way to produce fuel when coupled with renewable or nuclear energy sources, can split

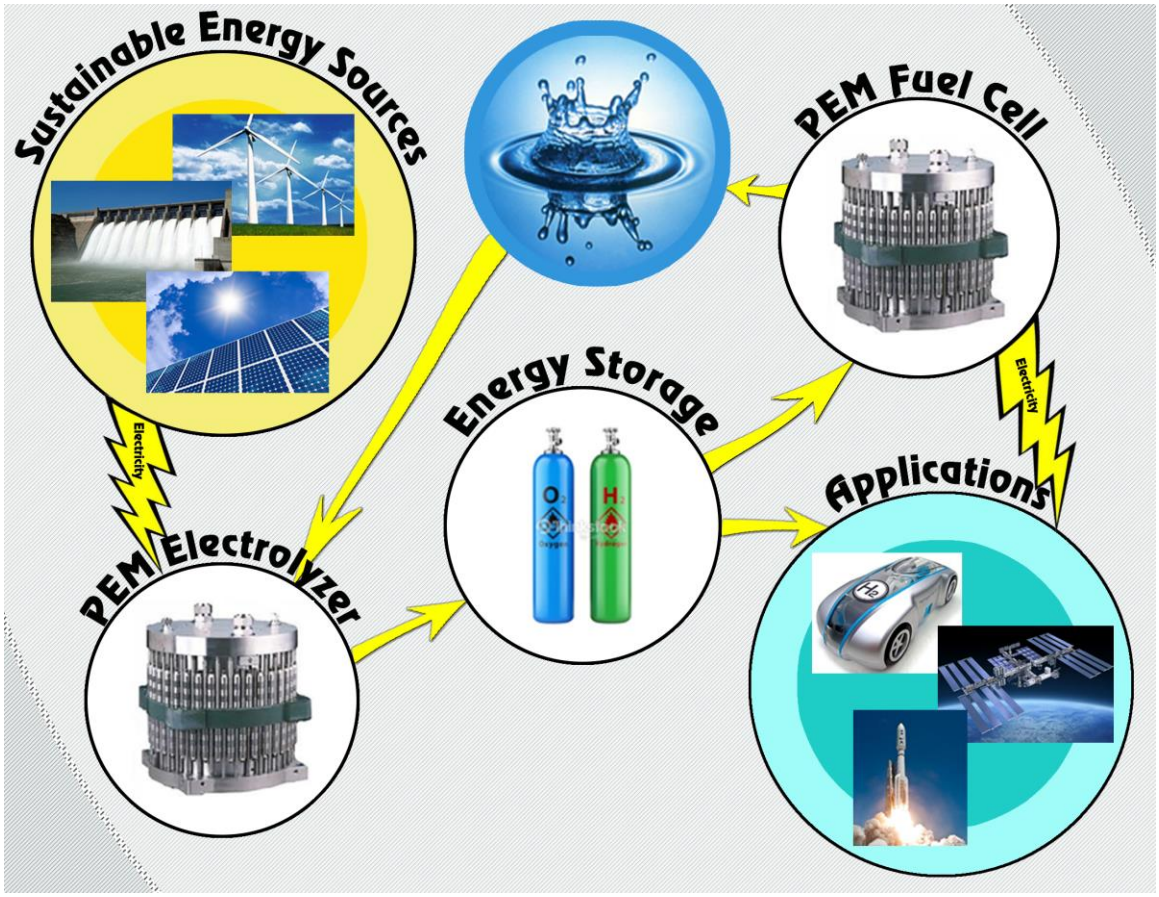


Figure 5.1. Schematics of applications of PEM electrolyzer cells and PEM fuel cells coupled with renewable energy sources.

water into hydrogen and oxygen by using electrical power. The integration of a sustainable energy source and water electrolysis is very attractive because of its high efficiency, lack of carbon and numerous applications as shown in Figure 5.1 (energy storage, fuel cell vehicle, oxygen generation system in pace and propulsion), although the cost is still higher than other conventional energy sources [5-10].

Compared to traditional water electrolysis technologies, proton exchange membrane electrolyzer cells (PEMECs) have several main advantages, including fast dynamic response time, favorable energy efficiency/density, high hydrogen purity and a more compact design [13, 14]. Although the PEMEC has been developed in past decades, it still has several significant challenges to overcome to be widely applied in hydrogen/oxygen production, including cost, durability and efficiency [13, 65, 80, 127]. PEMECs use proton exchange membranes (PEMs) as an electrolyte that permits the protons transport from anode to cathode, and typically employ $IrRuO_x$ and Pt as the anode and cathode catalysts, respectively. The main effects on costs are noble metal catalyst loading/catalyst utilization for electrochemical reaction and degradation of layers and interfacial contacts of PEMECs under the electrochemical reaction [16, 128, 129].

The principle of a PEMEC is electrochemically splitting water into hydrogen and oxygen. During the operation, as shown in Figure 5.2, deionized water is circulated at the anode side through a flow field to the membrane electrode assembly (MEA) where it electrochemically reacts with catalyst and is split into oxygen, protons and electrons. The protons are then transported through the membrane, react with electrons from an external electrical force, and form hydrogen at the cathode, which exits through the flow channel at cathode side. Meanwhile, the oxygen is transported along with the water out of the anode.

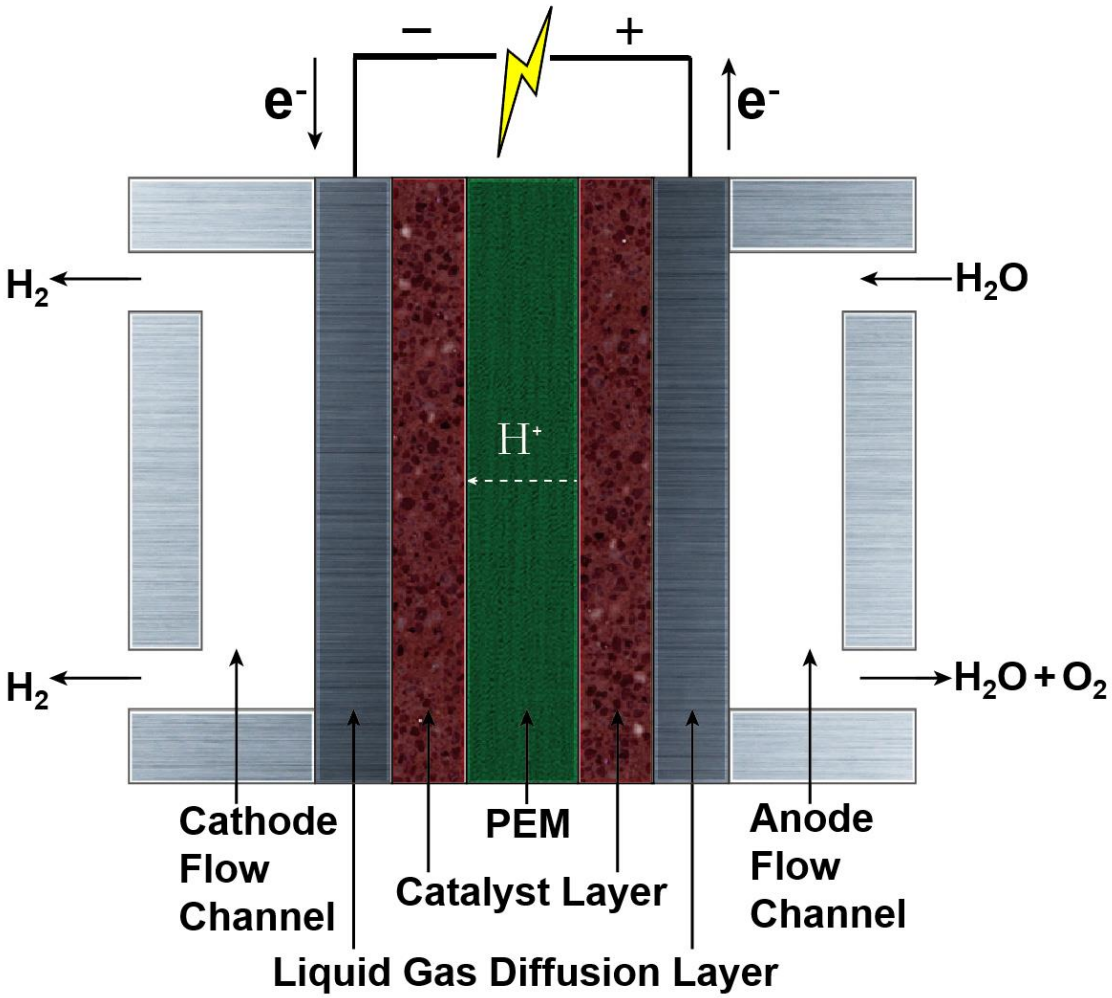


Figure 5.2. Schematic of a cross-section view of a PEMEC.

The stoichiometric equations for the electrochemical reactions at both sides in a PEMEC are shown below in Equation (9) and Equation (10). Theoretically, the amount of gases produced per unit time is directly related to the current that passes through the electrochemical cell.

$$Anode:\ 2H_2O \xrightarrow{Catalyst} 4H^+ + O_2 + 4e^- \quad (9)$$

$$Cathode:\ 4H^+ + 4e^- \xrightarrow{Catalyst} 2H_2 \quad (10)$$

The performance of PEMECs depends on electrochemical reactions and the associated properties of the membrane electrode assembly (MEA), including catalyst utilizations, membrane conductivities, activities of catalyst layers, and structures of liquid/gas diffusion layers (LGDLs) [19, 20, 24, 50]. In PEMECs, the electrochemical reactions occur only on "triple-phase boundary", meaning locations with electron conductors, catalysts, proton carriers, and pathways for reactants/products. For instance, a water splitting location at the anode needs: (i) A pore to transport liquid water in and gaseous O_2 out; (ii) catalyst and electron conductors for the reaction; and (iii) electrolyte for proton transport [17, 18, 122, 124]. It is critical to understand the fundamental principles and get the real situation of triple-phase boundary electrochemical reactions in PEMECs. However, since the reaction sites are located at the interfaces between the center layers of a PEMEC behind the other components, it has been a challenge to exploit *in-situ* micro-scale rapid electrochemical reactions and micro-scale interfacial effects for a long time. (i) The electrochemical reaction site on catalyst layers is next to the center part of PEM and located behind LGDLs, current distributor with flow channel and end plate; (ii) LGDLs are typically made of titanium fibers or foam with random interconnected and complicated pore morphology; (iii)

Current distributors are made from titanium to resist the high potential and oxidative environment; (iv) a large working distance for optical systems is required and the conventional microscope will not meet the needs at high spatial resolutions. Those factors have made it barely impossible to perform *in-situ* characterization to determine the role of the triple-phase boundary and phenomena of electrochemical reactions in PEMECs.

In this study, an innovative design of a transparent and reaction-visible PEMEC coupled with a high-speed and long working distance micro-scale visualization system and an electrochemical impedance spectroscopy for electrochemical reaction quantification is introduced. With micro/nano technology and advanced manufacturing, thin-film LGDLs with throughout straight pores have been developed and implemented to permit direct visualization of the electrochemical reactions in the PEMEC. The true mechanism of the rapid and micro-scale electrochemical reactions of splitting water in PEMEC are revealed for the first time.

5.2 Methodology

A PEMEC mainly consists of a catalyst-coated membrane (CCM) sandwiched by two electrodes and two end plates as shown in Figure 5.3. The catalyst coated membrane (Fuel Cells ETC, Inc.) is Nafion® 115 film with IrRuOx and Pt employed as anode and cathode catalysts, respectively. In the conventional PEMEC, both end plates are made of aluminum. The anode current distributor with a parallel flow field is fabricated from a titanium plate, while the cathode current distributor and flow field are fabricated from copper and graphite plate with a parallel flow field, respectively. The cathode GDL is Toray 090 carbon paper treated with 5% PTFE, while titanium felt is used as an anode LGDL. To visualize the electrochemical reactions *in-situ* at the center of the PEMEC, some alterations were made

compared to the conventional PEMEC. First, a rectangle hole on the anode end plate was machined as an observation window, similar to a transparent PEMFC in our previous work [111, 130, 131]; Secondly, the titanium anode current distributor with a parallel flow field was divided into two parts: a transparent plate with flow-in holes/channels, and a 0.5 mm titanium plate with chemically etched parallel flow channels of 1 mm in channel width. Additionally, a novel thin-film anode LGDL was developed by using micro/nano fabrications on thin titanium film with a thickness of 25 μm [42, 46, 82]. Eight evenly distributed bolts were used to assemble the single 5 cm^2 cell with a torque of 40 in-lb. The reaction-visible PEMEC was operated at room temperature with a flow rate of 40 ml/min controlled by a diaphragm liquid pump from KNF Neuberger.

In the PEMEC test, all electrochemical parameters are controlled by a SP-300 chassis with a 10A/5V booster kit. The built-in FRA has a frequency range of 10 μHz up to 7 MHz. Galvanostatic electrochemical impedance spectroscopy (GEIS) was used for measuring the impedance of the PEMEC at different operating conditions.

The high-speed and micro-scale visualization system (HMVS) is also unique and includes a high speed camera (Phantom V711) and in-house optical assembly. The high-speed camera can achieve a maximum speed of 7,500 frames-per-second (fps) at full resolution. At reduced resolutions, it can deliver up to 1,400,000 fps. The in-house optical assembly consists of a main zoom lens body and a series of objective and eye-piece lenses, with a working distance of > 70 mm even at high resolution. This feature distinguishes it from a conventional microscope, which need a much smaller working distance at a similar spatial resolution.

All parts were fastened on XYZ stages and positioners with well-designed layout and

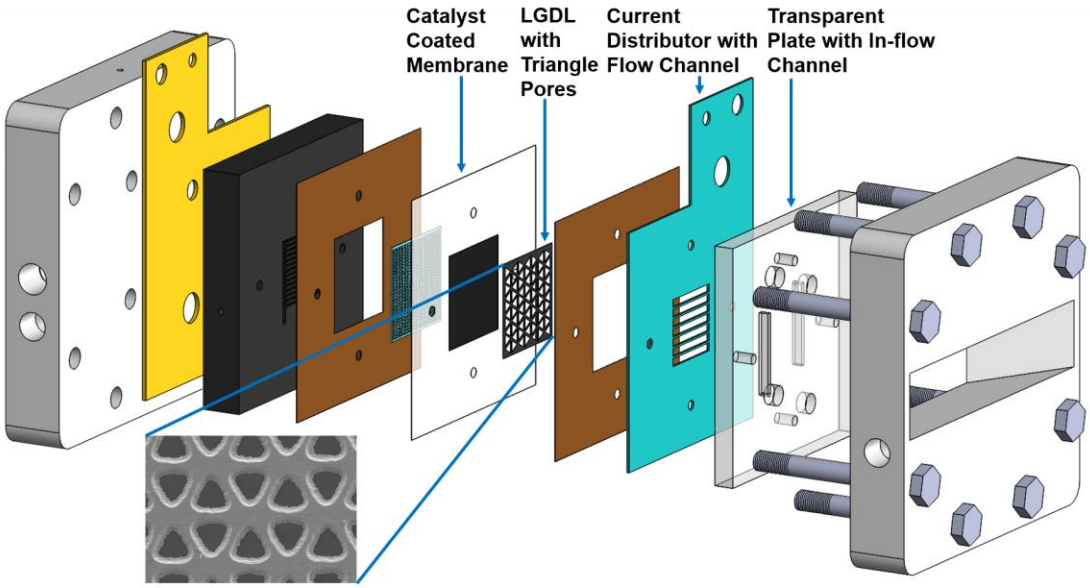


Figure 5.3. Schematic of the transparent and reaction-visible PEM electrolyzer cell, LGDLs have well-controllable and throughout straight holes.

control. The relative distance between the observation window of reaction-visible PEMEC and HMVS can be finely regulated. In addition, a cold light source with adjustable intensity was introduced through goosenecks to this system to ensure high quality videos and pictures. Local reaction activities can be monitored and analyzed based on micro-scale oxygen production in reaction-visible/operational PEMECs by HMVS.

The electric resistivity of materials for triple-phase boundary reaction in PEMEC were measured. The thin film materials were measured by four-point probe (Lucas Lab Pro 4-4400). Since the catalyst layer is porous media, there are some fluctuation of measurement by using four-point probe, the value is the average of five measurements.

Nano-manufacturing of titanium thin/well-tunable LGDLs

To get the visual image from inside of the PEMEC, some design modifications are conducted on conventional electrolyzer. Especially, a novel thin anode LGDL was developed by using nano-fabrications on thin titanium film.

As shown in Figure 5.4 a low-cost wet etching process was specifically developed in oak ridge national lab (ORNL). The titanium thin/well-tunable LGDLs are manufactured using lithographically patterned resist masks and chemical wet etching of thin foils [82]. The fabrication procedure for titanium thin LGDL begins with the design and fabrication of the photomasks. With this step, different pore size, pore shape and pore distribution can be achieved. A mask pattern was designed using commercially available CAD/VLSI software (LayoutEditor, layouteditor.net). The design pattern was imported into a Heidelberg DWL 66 laser lithography system and patterned on a soda-lime glass mask plate that is precoated with chromium and photoresist. After patterning, the masks were developed for 1 minute in Microposit® MF® CD-26 Developer (Shipley Company, Marlborough, MA), rinsed

with DI water and dried with N_2. Masks were then submerged in chrome etchant for 2 minutes, rinsed with DI water and dried with N_2. The remaining resist was subsequently removed in a heated bath (70^{o}C) of N-Methyl Pyrolidone (NMP). Masks were rinsed with DI water and dried with N_2. As shown in Figure 5.4, in order to provide structural integrity of the extremely thin titanium foil, foils were affixed to a silicon wafer during processing. Substrate were treated with Microprime P20 Primer (Shin-Etsu MicroSi, Inc., Phoenix, AZ) adhesion promoter by coating the substrate with adhesion promoter, waiting for 10 seconds and spin-drying the samples at 3000 RPM for 45 seconds. Subsequently Microposit SPR220 photoresist (Rohm and Haas, Marlborough, MA) was spin-coated onto samples at 3000 RPM for 45 seconds. The titanium film was then placed on the resist coated silicon wafer with special care due to its delicate features, and soft baked for 90 s at 115 ^{o}C. A second layer of P20 and SPR220 photoresist was applied to the titanium foil under identical conditions, and then exposed to UV light using conventional contact photolithography. Developed in Microposit® MF® CD-26 Developer (Shipley Company, Marlborough, MA), rinsed with DI water and dried with N_2. Finally, after patterning the photoresist mask on the foil, the patterned material was etched in HF etchant.

Based on the above mask pattern wet etching process, Titanium thin/well-tunable LGDLs with different pore sizes and pore shapes were fabricated.

A sequence of pictures of electrochemical reactions in micro pores of PEMEC

A sequence of close-up images of pore-scale electrochemical reactions is shown in Figure 5.5. It can be observed that, with the lapse of time, the oxygen bubbles are only generated and grow along the edge of LGDL pore land. In Figure 5.5 (A), at the initial time of the video, a relatively large oxygen bubble just flows over the pore of LGDL, which absorbs

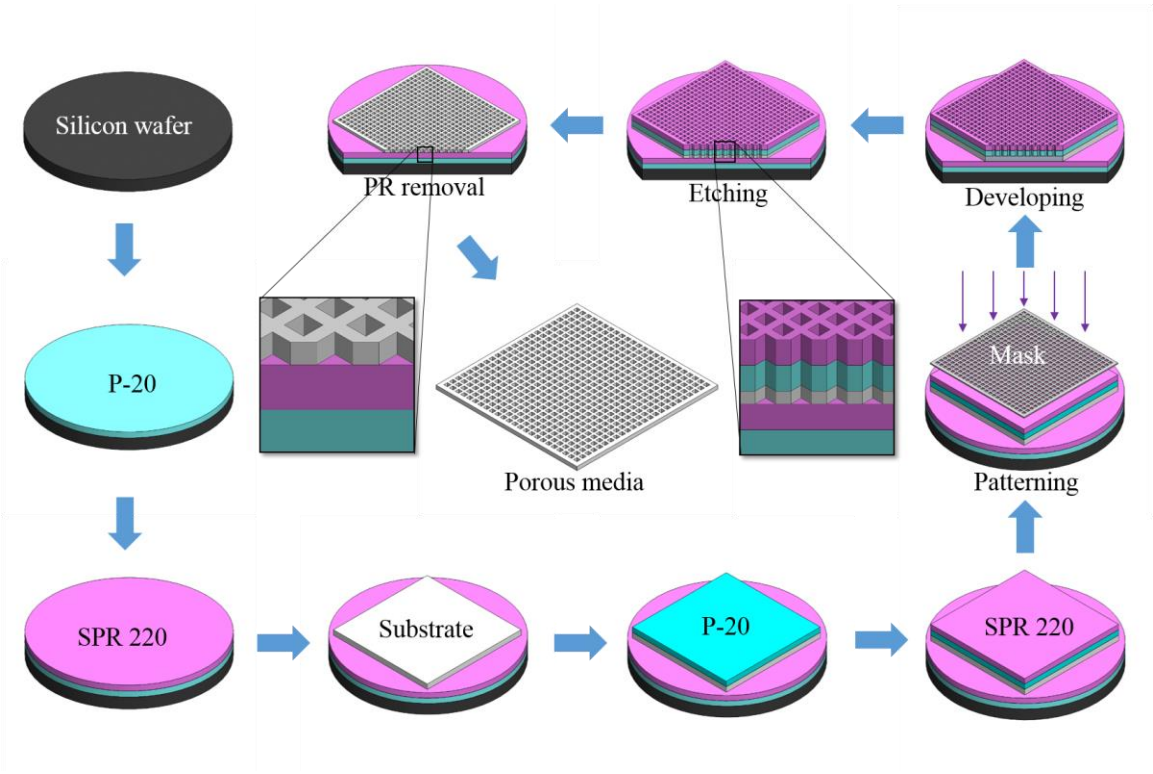


Figure 5.4. Schematic of a developed nano fabrication process for titanium thin-film LGDL with well-tunable micro pores.

some small bubbles along with the land of pore; in Figure 5.5 (B), at 0.0017s, some oxygen bubbles with different sizes are observed clearly along the edge of pore land; in Figure 5.5 (C), at 0.0033s, both the quantity and size of oxygen bubbles increase; in Figure 5.5 (D), at 0.005s, the size of oxygen bubble along the edge of pore land get larger and larger; in Figure 5.5 (E), at 0.0067s, some small oxygen bubbles merge together formed some big bubbles; in Figure 5.5 (F), at 0083s, the size of oxygen bubbles keep increasing and some of them are going to detach the surface of catalyst layer. The similar reactions are also observed in the PEMECs with various LGDL parameters with different pore sizes from 50 μm to 600 μm and pore shapes (triangular and circular), as shown in Figure 5.6. All of them were also operated at the same current density of 2 A/cm^2. The dynamic details can be found in the supplementary materials: Movie S1 to S5.

Preliminary results of new fabrication of catalyst

The phenomena caught in the experiments revealed the real situation of electrochemical reactions in a PEMEC, which could be a new instruction of fabrications and optimizations of catalyst layers. For instance: deposit catalyst layers only on the edges of LGDLs as shown in Figure 5.7 (E). To further prove the assumption concluded in manuscript, two groups of control experiments were conducted. Both group experiments are conducted in the following PEMEC.

A PEMEC was designed and fabricated in lab for conducting the designed experiments. It consists of two endplates made from commercial grade aluminum and designed to provide even compression pressure on the cell. In order to apply a current to the cell, a copper plate was inserted at the cathode as a current distributor. The bipolar plate was fabricated from graphite and used a parallel flow field to distribute the flow over the active area of the cell.

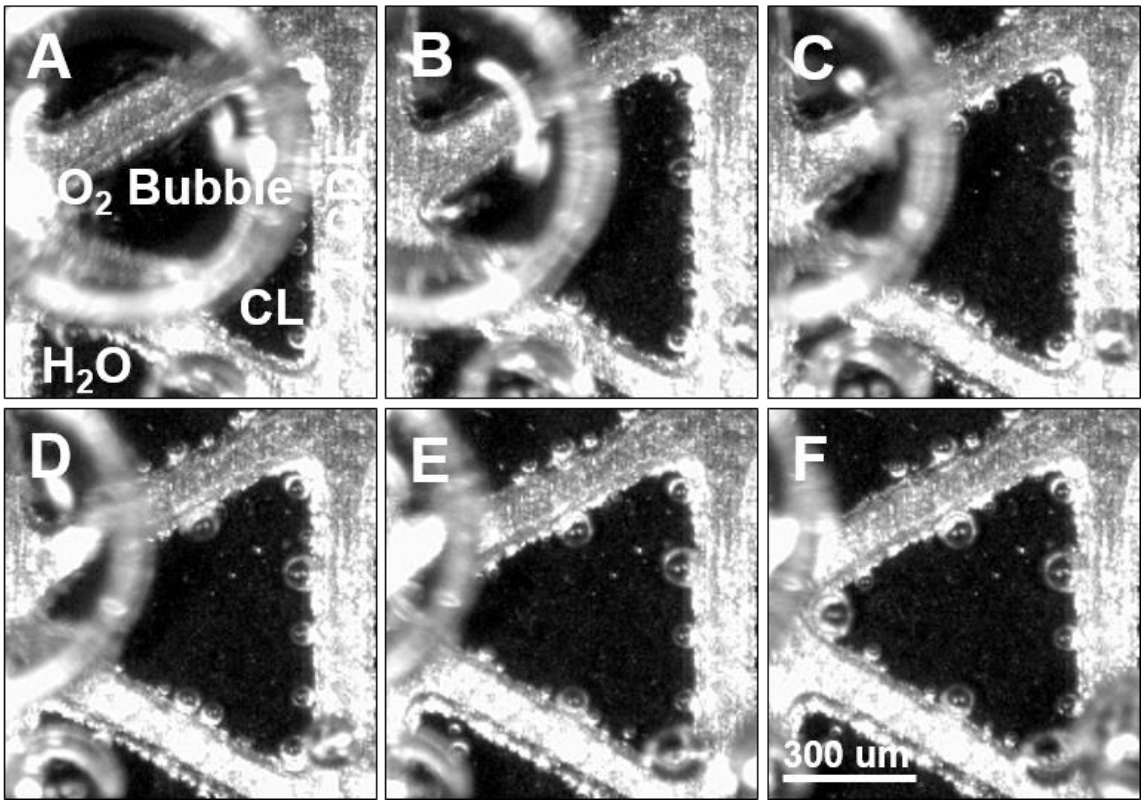


Figure 5.5. A sequence of pore-scale images of electrochemical reactions (triangular pore size: 600 µm, water is fully fill the channel and flowing from right to left): (A) Initial time, t_0*; (B)* t_0 *+ 0.0017 s; (C)* t_0 *+ 0.0033 s; (D)* t_0 *+ 0.005 s; (E)* t_0 *+ 0.0067 s; (F)* t_0 *+ 0.0083 s.*

In order to maintain even compression and prevent leakage, gaskets for the LGDLs were fabricated from PVC. The cell was compressed by eight evenly distributed bolts, which were tightened to 40 in-lb. of torque during assembly. The electrolyzer had an active area of 5 cm^2 and was operated at 80 ^oC temperature.

The PEMEC cell was attached to an electrolyzer control system with a current range up to 100A and a voltage range of up to 5V. The hardware was connected to Bio-Logic software, EC-Lab, which was used to conduct performance testing and electrochemical impedance spectroscopy (EIS). For controlling the flow, a system of piping was connected to the PEMEC. While the cathode piping was merely intended to safely exhaust hydrogen gas that formed during electrolysis, a diaphragm liquid pump from KNF Neuberger was used to circulate water at a constant volumetric flow rate of 20 ml/min through the anode.

The only difference between two groups of experiments is cathode catalyst fabrication. The experimental group using a conventional catalyst-coated membrane. The catalyst-coated membrane is comprised of Nafion 115, a perfluorosulfonic polymer with a thickness of 125 μm, an anode catalyst layer with an IrRuOx catalyst loading of 3 mg/cm^2, and a cathode layer with a platinum black (Pt/B) catalyst loading of 3 mg/cm^2. The control group using a single side catalyst-coated membrane. The single side catalyst-coated membrane is comprised of Nafion 115, a perfluorosulfonic polymer with a thickness of 125 μm, an anode catalyst layer with an IrRuOx catalyst loading of 3 mg/cm^2. The cathode catalyst Pt was sputtering coated on the LGDL with 15 nm thickness.

The performance comparison is shown in Figure 5.8. Although the PEMEC with catalyst at new fabrication method has worse performance compare to regular one, the difference at current density of 2 A/cm^2 is only 0.117 V, which may be caused by increased interfacial

ohmic resistance due to new fabrication method of cathode catalyst layer. The using of cathode catalyst Pt in control group in only around 1/90 of Pt using in experimental group, which significantly maximum utilizing the catalyst and reduce the cost of PEMECs.

The MEA has been also investigated *ex-situ*. The cathode layers were analyzed by scanning transmission electron microscopy (STEM). The inset HAADF-STEM images show both electrodes contain particle sizes below ten nanometers.

5.3 Results and discussion

A typical image of electrochemical reactions in a PEMEC microchannel with the high-speed and micro-scale visualizations is shown in Figure 5.6 (A). The black parts in the channel are catalyst layer, and the grey shiny areas are LGDLs, which appear between the grey dim parts – lands of microchannel. The thin-film LGDL has uniform triangular pore distribution with a pore height of about 600 μm and a pore wall width of about 150 μm. During operation, the microchannel of the PEMEC is fully filled with deionized water and the PEMEC was operated with a constant current density. The cell voltage is around 2.5V under a current density of 2 A/cm^2 at room temperature, which is close to a conventional cell [132].

The oxygen bubbles are formed on the surfaces of the catalyst layer (black parts), which are adjacent to LGDLs (grey shinny parts). Then due to electrochemical reactions and coalescence, they grow, detach from the catalyst layer surface and merge into each other. Finally, the oxygen bubbles flow out of the PEMEC with deionized water through the microchannel. During this process, several types of liquid/gas two-phase flow, including

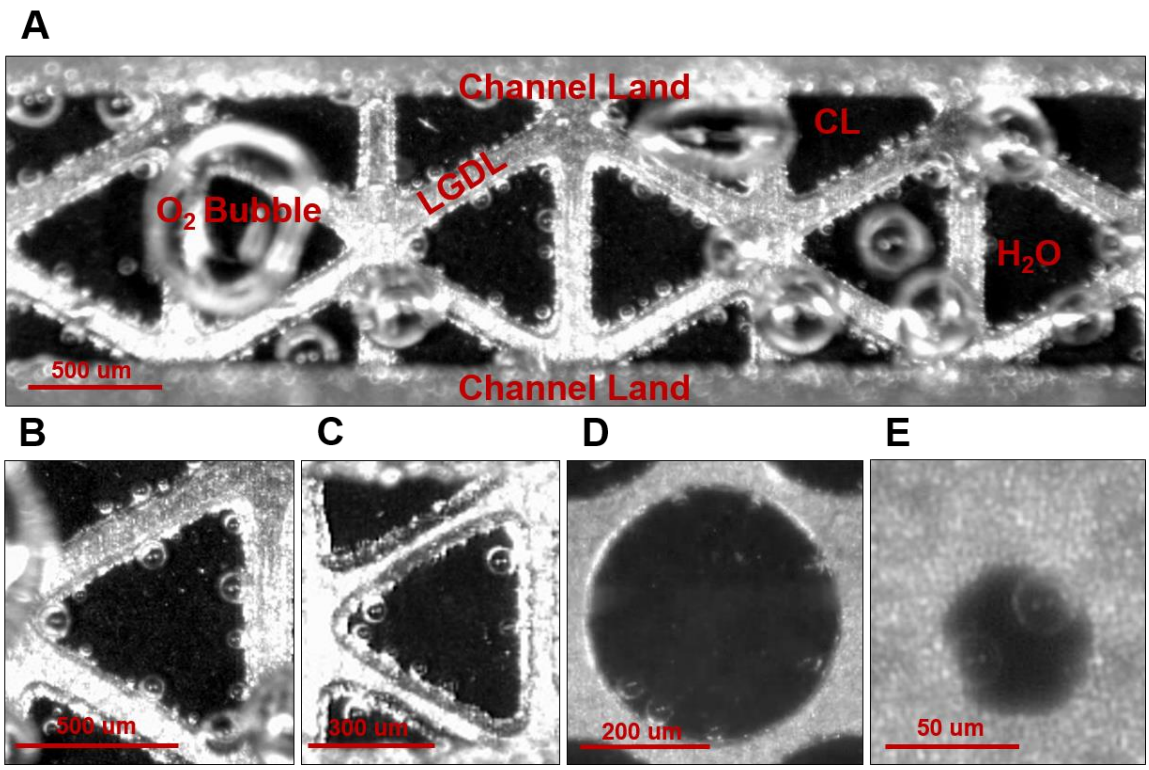


Figure 5.6. Micro-scale electrochemical reactions in PEMECs. (A) Front-view image of electrochemical reactions in the PEMEC microchannel. (B) 600 µm triangular pore; (C) 400 µm triangular pore; (D) 500 µm circular pore; (E) 50 µm circular pore. (Please see the detail from the supplementary material: Movie S1, Movie S2, Movie S3, Movie S4 and Movie S5).

bubbly, plug and slug, are formed in the microchannel. More details with a typical video clip can be viewed at the supplementary material (Movie S1). Surprisingly, the reaction sites, where the oxygen bubbles are generated, have some preferences and did not occupy the catalyst layer surface uniformly. The oxygen bubbles appear to be generated only at the interface of the liquid/gas diffusion layer and catalyst layer. As shown in Figure 5.6 (B) to (C), most of the bubbles are generated along the edge of the pores, even with different pore size from 50 μm to 500 μm and under different pore shapes. Some bubbles in the middle of pores are observed to be moving with the flowing deionized water after they have detached from the catalyst layer.

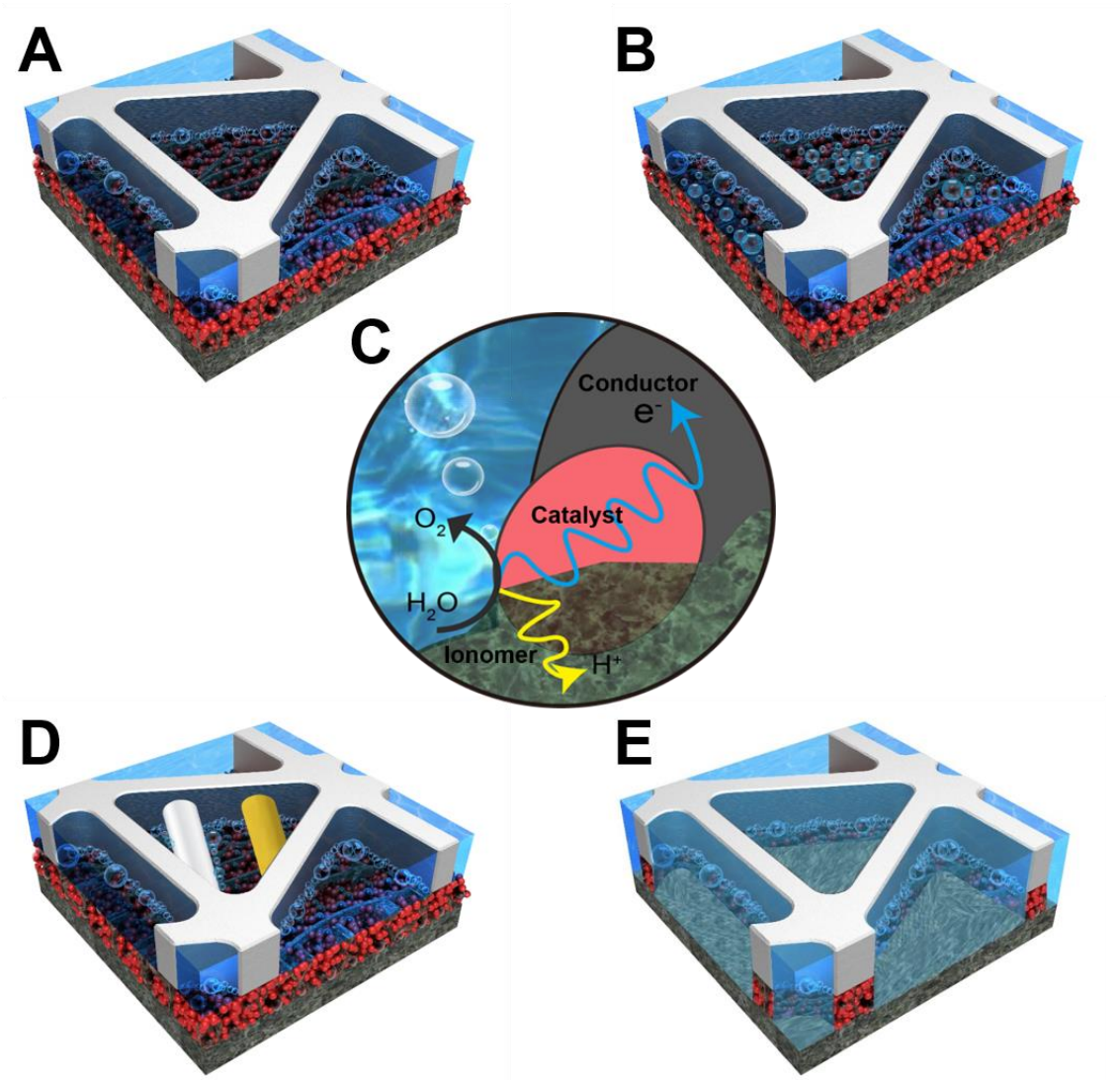
The visualization results indicate that all observable reactions occurred almost exclusively along the catalyst layer-LGDL walls as shown in Figure 5.7 (A). Usually, catalyst layers in PEMEC have been designed and fabricated as reaction sites to conduct electrons, protons, and reactants/products. Until now, it has been assumed that reactions occur across the entire catalyst layer surface as shown in Figure 5.7 (B), which meet the conventional triple-phase boundary requirements as shown in Figure 5.7 (C). The discovery in this article challenges previous assumptions for PEMECs. While most of the catalyst loaded on catalyst layers (the most expensive part in the device) did not function as designed (representing a significant waste). To make sure the bubble generation sites are the same as electrochemical reaction sites. Several experiments were designed and conducted to suppress the interferential phenomena. As shown in Figure 5.7 (D) and supplementary materials movie S6 and S7, both electric conductive wire and nonconductive wire were put between the catalyst layer and LGDL. When the PEMEC was operating in the current density of 2 A/cm^2, there is only bubble generation along the conductive wire, which can

easily conduct electrons for electrochemical reactions. Those two wires have been put in several different locations, the same phenomena are observed. This preclusive experiment further proved the bubble generation sites observed in this research are the same sites of electrochemical reaction. Actually, the roughness of catalyst layer surface is enough for bubble nucleation. This discovery represents a potential opportunity to enhance the multiphase interfacial reactions and significantly reduce the cost for commercial applications through heterogeneous distribution of catalysts along the catalyst layer-LGDL interfaces.

The electrochemical reaction only occurs at locations with all conditions that coexist for triple-phase boundary reaction: pathways for reactant and product, catalyst, and conductors for protons and electrons. Based on the visualization results, it can be assumed that, in PEMECs, the water is only decomposed to protons, electrons and oxygen at the locations where the triple-phase boundary exists in the anode of PEMEC. Meanwhile, the in-plane ohmic resistivity of the IrRuOx catalyst layer has been found to be more than 10,000 times larger than the thin titanium LGDL. The huge in-plane ohmic losses in catalyst layers prevent the electrochemical reactions from occurring in the middle region of pores even at very small pores, as shown in Figure 5.7 (E). No electrochemical reactions in the region result in no oxygen bubble formation and growth there, which explain the phenomena observed in an operating PEMEC. The exclusive experiments have been conducted as aforementioned.

The phenomena caught in the experiments revealed the real situation of electrochemical reactions in a PEMEC, which could be a new instruction of fabrications and optimizations of catalyst layers. For instance: deposit catalyst layers only on the edges of LGDLs or

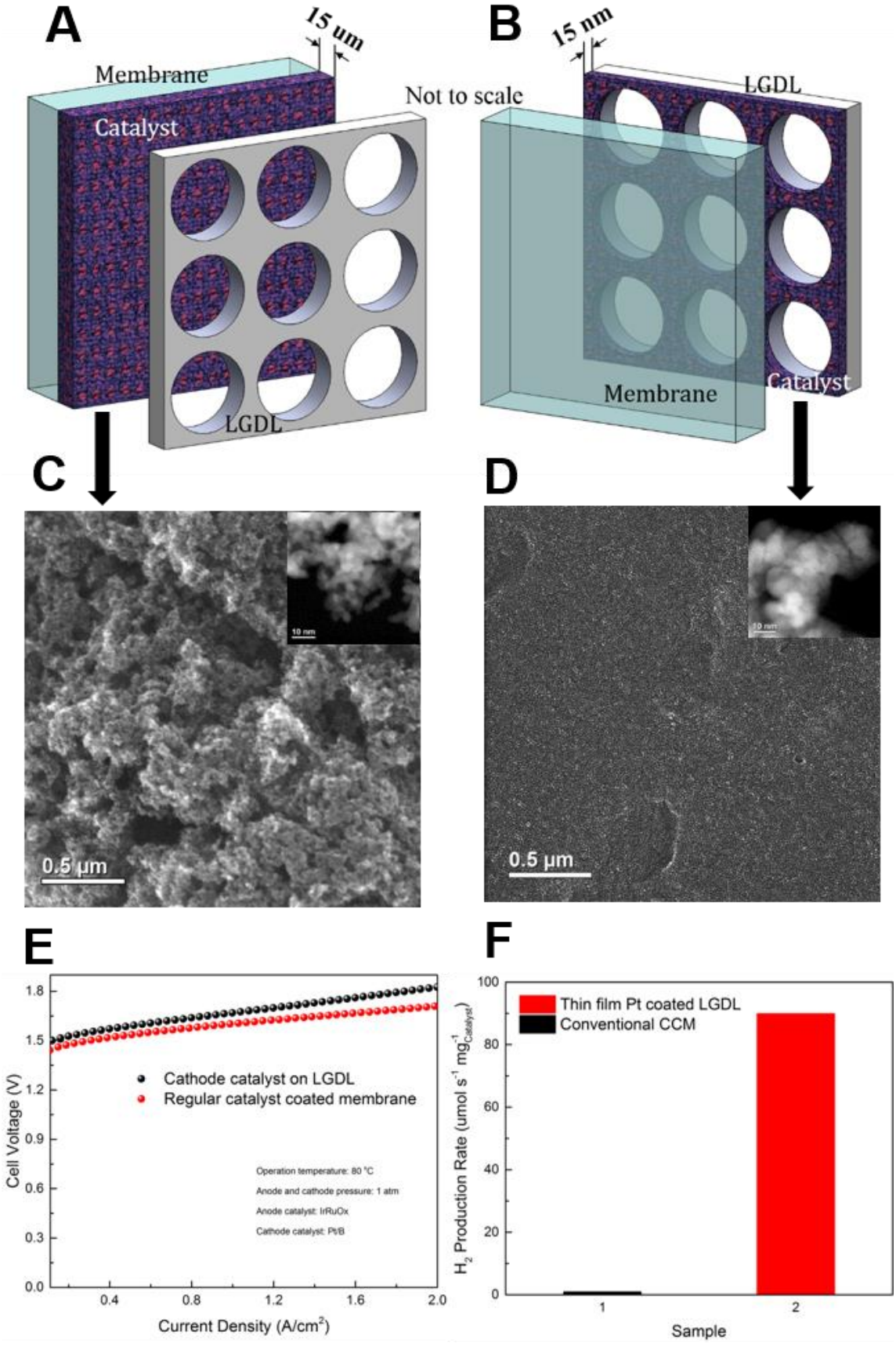
Figure 5.7. Schematic of pore-scale electrochemical reactions occurred in the anode of a PEMEC. (A) True phenomena of electrochemical reactions occurred in PEMECs. (B) Conventional assumption of electrochemical reactions in PEMECs. (C) triple-phase boundary electrochemical reaction in PEMECs. (D) Phenomena of exclusive experiments for electrochemical reaction occurred in the anode of PEMECs (white wire: conductive material, yellow wire: non-conductive material, please see the detail from the supplementary material: Movie S6 and Movie S7). (E) Future design and fabrication of catalyst layer in PEMECs, the catalyst only deposits on the lands of LGDLs.


A
B
C
Conductor
e-
Catalyst
O2
H2O
Ionomer
H+
D
E

promote the in-plane electron conductivities in catalyst layers as shown in Figure 5.7 (E). This discovery can significantly reduce the cost of PEM electrolyzer cells while keep on with excellent performance (same catalyst), which is the major issue in widely commercial application of PEM electrolyzer cells. Fundamental understandings from this research can help to devise a cost-effective path to improve the multiphase interfacial efficiency, increase catalyst utilization, and promote the reaction areas of PEMECs/PEMFCs. In addition, this controlled geometric LGDL and cell architecture enable more direct numerical simulations and validation through simplified and known internal morphology. Moreover, this research will open new possibilities to manipulate triple-phase interfacial effects in multi-scale engineering devices, which enable innovative designs with novel control of capillary transports and rapid reactions for wide applications.

To further confirm the assumption based on phenomena capture in an operational PEMEC, a novel catalyst fabrication was introduced. As shown in Figure 5.8 (A), the conventional method of catalyst loading was directly spayed or brushed on membrane. According to aforementioned assumption, a lot of catalyst was wasted in the middle area of LGDL pores. To maximize the utilization of catalyst, the catalyst was only sputter coated on the LGDL as shown in Figure 5.8 (B). Through the ex-situ investigation on the both catalyst, secondary electron (SE) STEM images were obtained of the backside of the Pt/B electrode and topside of the Pt thin film sputtered directly on the titanium LGDL. The microstructure is presented by SEM images (Figure 5.8 (C) and (D)), which is quite different. The sputter coating catalyst on LGDL has a much smaller crystal structure compared to catalyst with conventional-method loaded on membrane, which also help increase the contact surface area of catalyst. After put this novel fabricated catalyst layer in the PEMEC and testing,

Figure 5.8. Comparison of different catalyst loading method and substrates in the cathode of a PEMEC (one is on membrane and the other one is on LGDL). (A) Schematic of catalyst conventional-method loaded on membrane in PEMECs. (B) Schematic of catalyst sputter coated on LGDL in PEMECs. (C) SEM and zoom-in images of catalyst crystal structure which loaded on the membrane. (D) SEM and zoom-in images of catalyst crystal structure which loaded on the LGDL. (E) Comparison of cell voltage between cathode catalyst with a conventional method loaded on membrane and sputter coated on LGDL. (F) Comparison of H_2 production rate per catalyst loading between conventional method loaded on membrane and sputter coated on LGDL.


A
15 um
Membrane
Catalyst
LGDL
Not to scale
B
15 nm
LGDL
Membrane
Catalyst
C
0.5 µm
D
0.5 µm
E
Cell Voltage (V)
Current Density (A/cm²)
Cathode catalyst on LGDL
Regular catalyst coated membrane
Operation temperature: 80 °C
Anode and cathode pressure: 1 atm
Anode catalyst: IrRuOx
Cathode catalyst: Pt/B
F
H₂ Production Rate (umol s⁻¹ mg⁻¹ Catalyst)
Thin film Pt coated LGDL
Conventional CCM
Sample

the performance result is very close to the one with conventional fabricated catalyst layer (Figure5.8 (E)). It's noteworthy it that the thickness of two catalyst layer is differ greatly, so the H_2 production rate per catalyst loading of sputter coating on LGDL is far greater than the one with conventional method Pt/B loaded on membrane (Figure 5.8 (F)). This preliminary results provide very strong support for the aforementioned assumption, the electrochemical reactions only occur on the locations, which meet the triple-phase boundary requirements and prefer to close to the good conductive material.

Mathematical modeling for equivalent circuit

The visualization result is from in-situ image of a working transparent PEMEC assembled Ti film anode LGDL with etched triangle pore sharp. The height of triangle pore is 240 μm. Figure 5.5 and Figure 5.6 show the bubble generation, distribution and flow pattern in a flow channel and pore of LGDL, respectively. As shown in Figure 5.5, the oxygen bubble only generated along the edge of LGDL pattern where water, catalyst and conductor for proton and electron are all exist, which verify the aforementioned model of electrochemical reaction.

As shown in Figure 5.6, oxygen bubble generated on the catalyst layer and transport through the pore of LGDL. But the site of reaction is not cover the full edge of LGDL pattern, which indicate the catalyst is not loaded on every dot of surface of CCM, which will not affect the performance of PEMEC when current density is relative low.

The performance curve of the transparent PEMEC with 50 Ti mesh anode LGDL is shown in Figure 5.8. Compared to date from a conventional cell, the different of performance is very small. Considering the wettability and stiffness of the transparent block, this performance is acceptable.

An ohmic resistance model, as shown in Figure 5.9, was established for rough estimation of ohmic loss within CL. For better understanding effects of LGDL opening parameters, the CL and LGDL were integrated together into the Electrode. Considering the LGDLs have much better conductivities than the CLs, as detailed in Table 5.1, the CL ohmic loss could be inferred from the electrode ones. The interfacial contact resistances between the components were not considered.

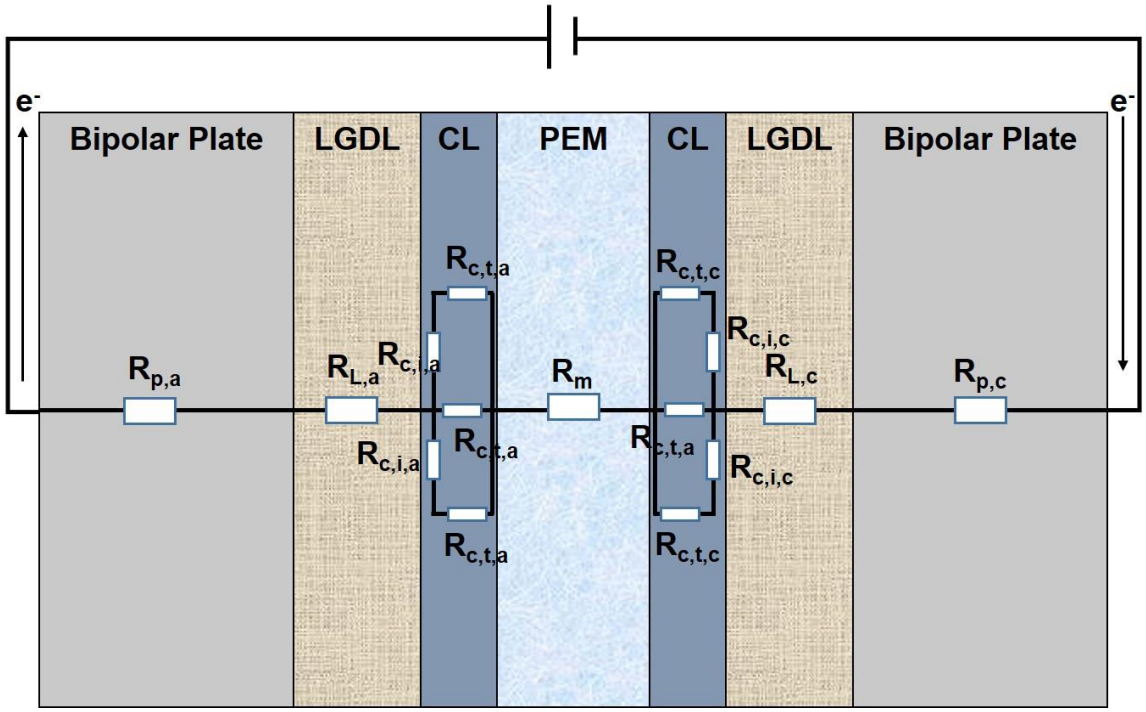


Figure 5.9. Schematic of ohmic distribution inside a PEMEC

The electrochemical performance relationship for a PEMEC should consist of open circuit voltage, activation overpotential, diffusion overpotential, and ohmic loss. The electrochemical performance relationship for a PEMEC should consist of open circuit voltage, activation overpotential, diffusion overpotential, and ohmic loss. The entire

overpotential relationship of a PEMEC, which is used to calculate the cell polarization curves, can be expressed as follows [13, 14].

$$V = V_{ocv} + V_{act} + V_{diff} + V_{ohm} \quad (11)$$

$$V_{ocv} = 1.229 - 0.9\times10^{-3}(T - 298.15) + \frac{RT}{zF} ln\left(\frac{\alpha_{H_2}\alpha_{O_2}^{0.5}}{\alpha_{H_2O}}\right) \quad (12)$$

$$V_{act} = \frac{RT_a}{\alpha_a F} sinh^{-1}\left(\frac{j}{2sj_{0,a}}\right) + \frac{RT_c}{\alpha_c F} sinh^{-1}\left(\frac{j}{2sj_{0,c}}\right) \quad (13)$$

$$V_{diff} = \frac{RT_a}{4F} ln\left(\frac{C_{O_2,m}}{C_{O_2,m0}}\right) + \frac{RT_c}{2F} ln\left(\frac{C_{H_2,m}}{C_{H_2,m0}}\right) \quad (14)$$

$$V_{ohm} = I\times(R_{plate} + R_{electrode} + R_{PEM}) \quad (15)$$

$$R_{electrode} = R_{electrode,c} + R_{electrode,a} = R_{electrode,c} + R_{LGDL,a} + R_{CL,a} \quad (16)$$

The unit resistance of anode catalyst layer $R_{CL,a}$, was considered to have an ohmic model as shown in Figure 5.10.

For instance, when the diameter of opening is 100 μm diameter, in an analyzing unit, the CL in the opening was divided into 50 tori with a width of 1μm for each torus. The in-plate resistance of the *n*th torus of catalyst layer is,

$$R_n = \rho\frac{l}{A_n} \quad (17)$$

Where l, is the width of the torus, A_n, is the in-plane conducting area of each torus. Since the all torus have the same width, l, equals to 1 μm for every torus. r_n, is the radius of each torus.

The through-plane resistance of the *n*th torus catalyst layer is,

$$R_{Mn} = \rho_{PEM}\frac{l_M}{A_{Mn}} \quad (18)$$

Where l_M, is the thickness of the catalyst layer, A_{Mn}, is the through-plane conducting area

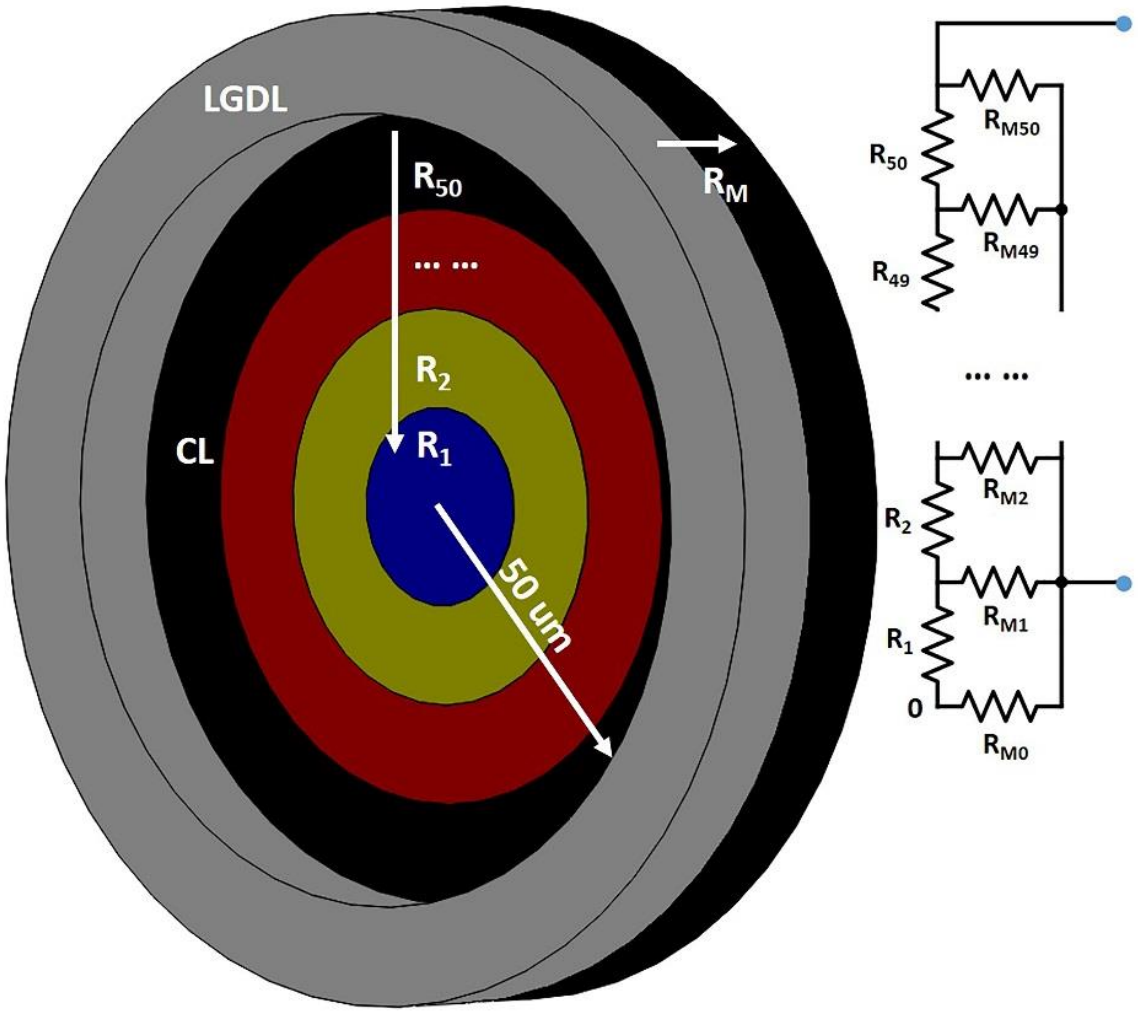


Figure 5.10. Schematic of an analyzing unit with dividing catalyst in a 100 µm diameter opening into 50 torus and equivalent circuit.

of each torus.

Based on the equivalent circuit in Figure 5.9, the total CL resistance of each unit is R_{unit}, which can be calculated by iteration method.

The number of units, which is also the number of openings, can be calculated by,

$$N = \frac{A*\varepsilon}{\pi*r^2} \quad (19)$$

Where A is the total area of the LGDL, ε is the porosity of the LGDL, r is the radius of the opening.

Since the resistance of catalyst layer is much greater than the one of LGDL, all unit can be considered parallel connected in the circuit. Then the resistance of catalyst layer can be calculated by following equation,

$$R_{CL} = R_{unit}/N \quad (20)$$

While for the resistance of LGDL, it can be simply calculated by following equation,

$$R_{LGDL} = \rho_{LGDL}\frac{t}{A*\varepsilon} \quad (21)$$

Where, t, is the thickness of LGDL, which is 25 microns for anode titanium thin film, and 280 microns for cathode carbon paper. A, is the active area. ρ_{LGDL}, is the resistivity of the titanium and carbon paper. And Table 5.1 listed the main parameters for the calculation.

Assume the operation of current density of 2.0 A/cm^2, the current flow into each unit is,

$$I = \frac{iA}{N} \quad (22)$$

The resistance of every resistor in equivalent circuit of Figure 5.10 can be calculated. Using iteration method, the current go through every torus has been calculated by MATLAB software, as shown in Figure 5.11. *L* represents the distance from the edge of the opening to the center, which means when *L* equals to 0 represent the location is at the edge of the

Table 5.1 Main calculation parameters for mathematical modeling of equivalent circuit for catalyst layer in PEMECs

Description, symbol	Value, unit
MEA active area, A	5.0 cm^2
PEM thickness, δ_m	125 μm
Anode LGDL thickness, δ_a	25 μm
Anode LGDL porosity, ε_a	0.3
Cathode LGDL thickness, δ_c	280 μm
Cathode LGDL porosity, ε_c	0.78
Anode LGDL resistivity, $\rho_{LGDL,A}$	$5.4\times10^{-7}\ \Omega \cdot m$
Cathode LGDL resistivity, $\rho_{LGDL,C}$	$8.0\times10^{-4}\ \Omega \cdot m$
Anode CL in-plane resistivity, $\rho_{CL,A}$	$1.52\times10^{-2}\ \Omega \cdot m$
Cathode CL in-plane resistivity, $\rho_{CL,C}$	$7.0\times10^{-5}\ \Omega \cdot m$
PEM resistivity, ρ_{PEM}	$4.41\times10^{-2}\ \Omega \cdot m$
Anode exchange current density, $i_{0,A}$	$6.0\times10^{-7}\ A/cm^2$
Cathode exchange current density, $i_{0,C}$	$1.0\times10^{-2}\ A/cm^2$
Operating pressure (anode), P_A	1 atm
Operating pressure (cathode), P_C	1 atm
Operating temperature, T	80 $°C$
Water molar mass, M_{H_2O}	18 g/mol
Oxygen molar mass, M_{O_2}	32 g/mol

Table 5.1 continued

Description, symbol	Value, unit
Faraday constant, F	96485 C/mol
Liquid water dynamic viscosity, μ_{H_2O}	$3.55\times10^{-4}\ N\cdot s/m^2$
Liquid water density, ρ_{H_2O}	1000 kg/m^3
Oxygen dynamic viscosity, μ_{O_2}	$2.34\times10^{-5}\ N\cdot s/m^2$
Oxygen density, ρ_{O_2}	1.429 kg/m^3

opening and when *L* equals to radius represent the location is at the center of the opening. From the results, it's can be seen that when the distance from the edge of opening is over 3 μm, the current will drop to less than 1% of current flow into this unit, which means over 99% current flow through CL covered by landing of LGDL and within 3 μm distance away from the edge of landing. In this study, we didn't observe bubble generation/nucleation away from the interfacial between LGDL and catalyst layer under current catalyst fabrication method.

The utilization of catalyst can be improved by decreasing the in-plane resistivity of catalyst layer as shown in Figure 5.12, Better current distributions will be obtained with smaller in-plane resistivity in CLs.

As the results shown in Figure 5.12, it can be concluded that the utilization of the conventional catalyst layer is highly controlled by electron transport. The difference of in-plane ohmic resistance between $IrRuO_x$ CL and LGDL is over 10,000 times. So the impact of opening size and porosity of LGDL cannot be ignored. According to the first order

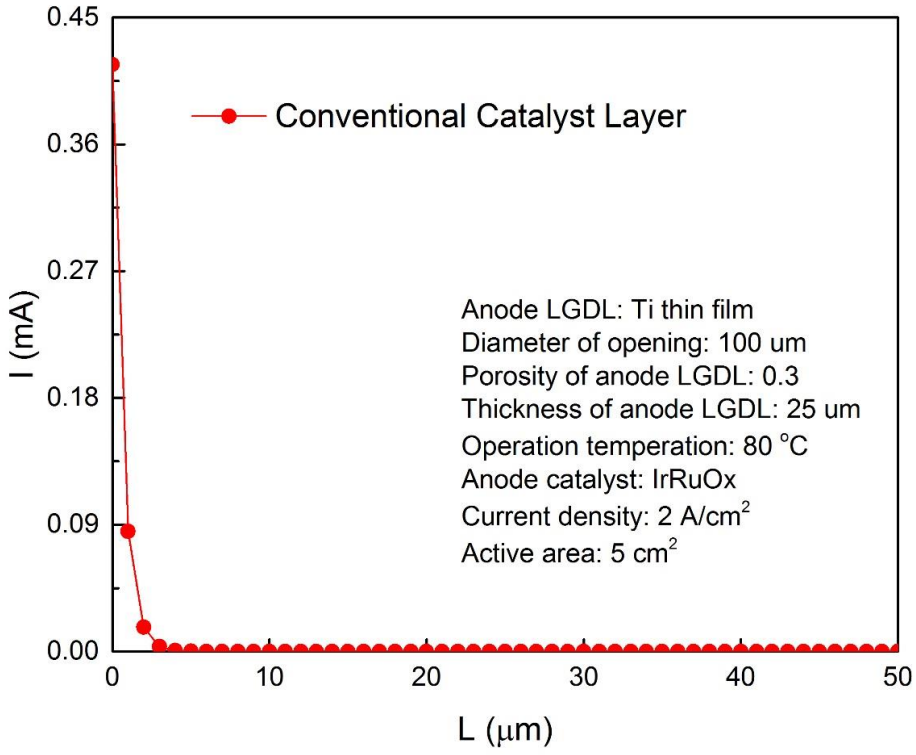


Figure 5.11. The relationship between current and distance away from the edge of opening, L. (L is the distance between torus and the edge of circular pore).

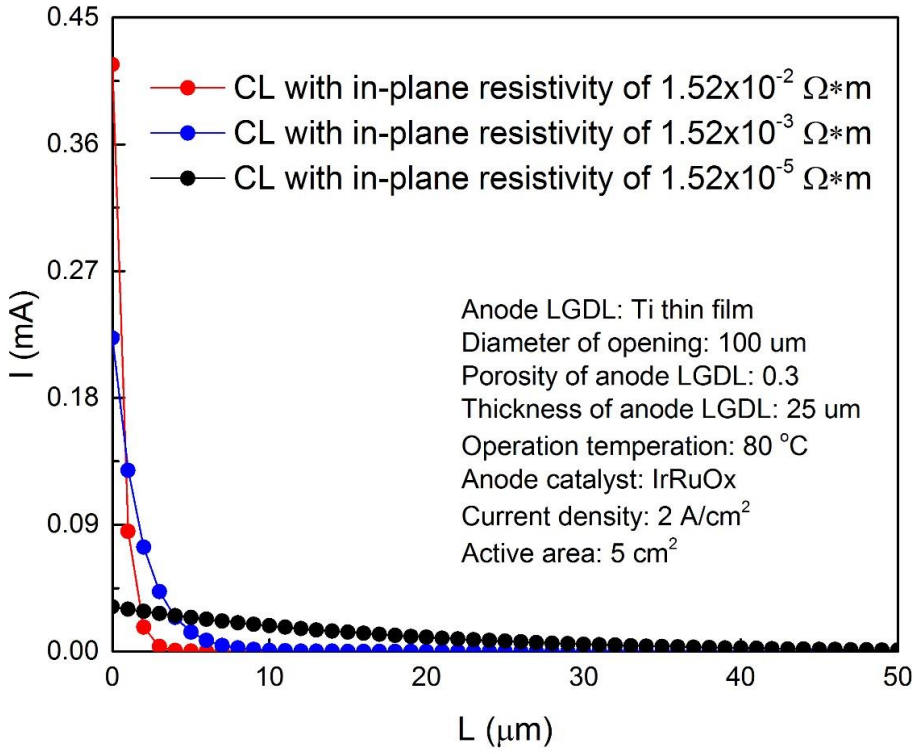


Figure 5.12. The relationship between in-plane resistivity of catalyst layer with current distribution on the surface of catalyzer layer. (Red dot is the results of CL with in-plane resistivity of 1.52×10^{-2} Ω·m, blue dot is the results of CL with in-plane resistivity of 1.52×10^{-3} Ω·m, black dot is the results of CL with in-plane resistivity of 1.52×10^{-5} Ω·m).

estimation, only resistance of LGDL and CL will be affected by the altering parameters of LGDL and the total ohmic resistance increases along with the increase of opening size or decrease of porosity, which means the performance will be improved with a decrease of opening size or increase of porosity.

5.4 Conclusion

The experiments in this research revealed that the in situ electrochemical reaction behaviors in PEMECs could serve as a guide for improved fabrication and optimization of CLs, even PEMECs as a whole. For example, CLs might only be deposited on the edges of LGDLs, as shown in Figure 5.7 (E). Modifications such as this could significantly reduce the use of expensive catalysts in PEMECs while maintaining performance levels, addressing the major barrier to the broad commercial application of PEMECs. Fundamental understandings from this research could also guide research to improve multiphase interfacial efficiency, increase catalyst efficiency, and promote the reaction areas of PEMECs and PEM fuel cells. In addition, controlled geometric LGDLs and cell architectures will enable more direct numerical simulations and validation through simplified and known internal morphology. Moreover, this research will open new possibilities to manipulate triple-phase interfacial effects in multiscale engineering devices, thus enabling innovative designs with novel control of capillary transport and rapid reactions for wide applications.

The real situation of electrochemical reaction locations in operating PEMECs are revealed for the first time by developing a reaction-visible PEMEC, a thin-film with LGDL with known internal morphology, and high-speed and micro-scale visualization system. Surprisingly, reactions preferentially occur on the catalyst layer and LGDL interfaces,

indicating most of the catalysts loaded on catalyst layers do not function and are thus wasted. The results of the mathematical modeling of ohmic equivalent circuit and preliminary results from PEMEC with a novel fabricated catalyst layer has substantiate this visualization results and assumption. Further understanding this real situation in nano or crystallize scale will help to optimize catalyst layer and LGDL designs and fabrications, which will significantly reduce the cost of the PEMEC and speed up its wide commercialization as one of the most efficient way of producing hydrogen and energy storage.

CHAPTER 6

DIRECT VISUALIZATION OF BUBBLE DYNAMICS IN PEMECs

6.1 Introduction

Water electrolysis is considered one of the most attractive methods to generate oxygen/hydrogen with carbon free and high efficiency, and it is also considered a promissing technique to solve the problems of both energy and environment, since this method can store the energy by coupled with intermittent renewable energy resources such as wind, hydro or solar [4]. In the space exploration, a sustained power and oxygen supply is crucial for the space applications. An oxygen generation system based on the water electrolysis has been deployed on international space station to supply oxygen for astronants [133]. Electrolysis of water is to split water into oxygen gas and hydrogen gas by using electricity. The integration of sustainable energy sources and water electrolysis becomes more and more attractive due to its high efficiency, renewable, and purity of products [13, 14, 18, 32, 65]. Compared to traditional technologies, proton exchange membrane electrolyzer cells (PEMECs) have several main advantages, including greater energy efficiency/density, higher production rate, faster response and a more compact design. However, to be widely comercialized in the oxygen/hydrogen production, there are still several barriers need to be broken, including cost, degradation and efficiency [8]. Proton exchange membranes (PEMs) were used as an electrolyte in the PEMEC that permits protons transfer from anode to cathode with high efficientcy, and $RuIrO_x$ and Pt/B were employed as the anode and cathode catalysts, respectively. When a PEMEC was operating, the water is decomposed into oxygen and proton by triple-phase boundary

reactions at the surface of anode catalyst, and meanwhile the liquid water is flowing over the liquid/gas diffusion layer (LGDL) and through microchannel yields two-phase transport conditions, which strongly affect the performance [134, 135]. It is very important to understand the fundamental principle of oxygen evolution reactions in PEMECs [136, 137]. The aim of this study is to reveal the phenomena of the oxygen evolution reaction inside PEMECs, which can optimize the design of catalyst layer and low-cost sustainable energy storage with high performance.

With the fixed active area, the local oxygen production is proportional to the current density, which is directly related to those two major factors: (i) the capillary flow of liquid water and oxygen gas; and (ii) interfacial conduction of protons and electrons. The effects of capillary flow and electrochemical interfaces can be separated by controlling applied currents. As shown in equation (22) below,

$$\dot{n}_{O_2} = \frac{iA}{2F} \qquad (23)$$

At lower current density of i with fixed area of A, both liquid water consumption and oxygen production are very small, and there is no transport limitation of capillary flow for the reactions. The interfacial contacts and conductions will dominate the reactions. The reaction area with better interfacial effects will produce more oxygen. As aforementioned, in PEMECs, the oxygen generated on the catalyst layer at the anode side due to the multi-phase boundary reaction and the water/oxygen transports over the LGDL yield two-phase flow. The microfluidics not only occurs in flow channel, but also in the pores of anode LGDL. Microfluidics in horizontal channel has been studied by lot of scholars. Typical

four two-phase flow patterns as shown in Figure 6.1, such as bubbly, plug, slug, and annular, were observed along the long side of the channel [134, 138].

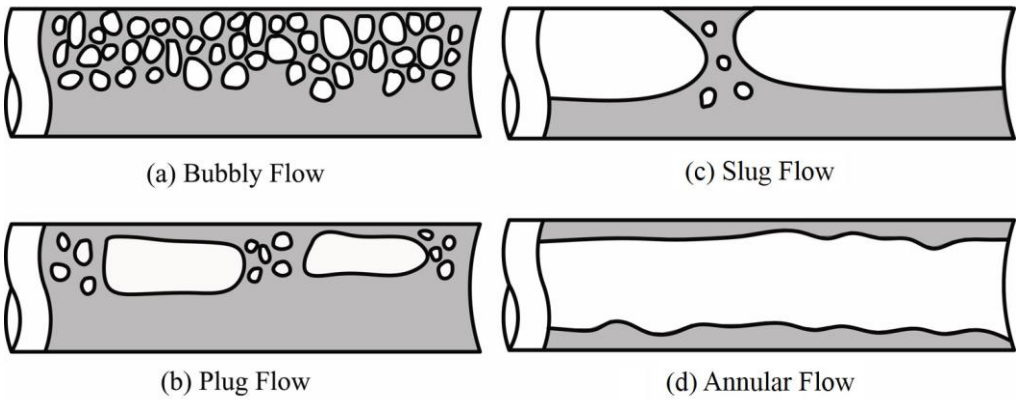


Figure 6.1. Four typical two-phase flow patterns in horizontal microchannel.

For microfluidics inside the pore, the flow pattern is major controlled by capillary pressure, wettability, pore shape and pore size. With the different wettability of the LGDL, the schematic of microfluidics in the pore of LGDL is shown in Figure 6.2.

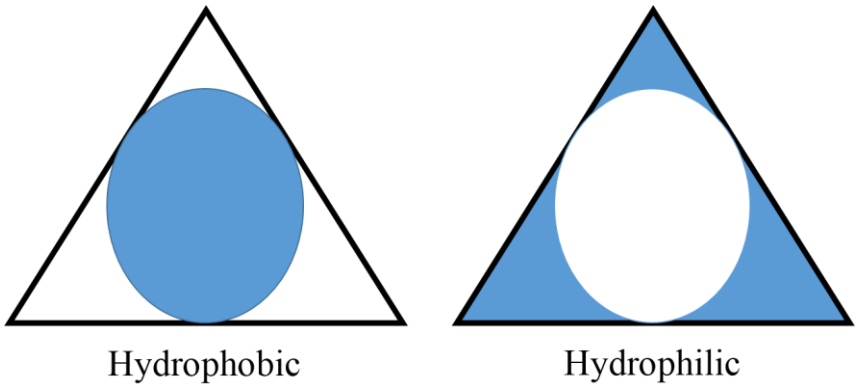


Figure 6.2. Schematic of two-phase flow in a triangle micro-pore in LGDLs with different wettability.

In this study, by taking advantage of the thin and well-tuned titanium LGDLs with straight pores, a novel designed PEMEC with a titanium thin/well-tunable LGDL is introduced to observe directly oxygen evolution reactions on the surface of the anode catalyst layer (CL) through micro LGDL pores and flow channels. Based on the development of a newly designed transparent PEMEC and a high-speed, micro-scale visualization system (HMVS), the relationship between oxygen evolution reaction and current density in an operating electrolyzer cell can be visualized *in-situ* by simultaneous optical imaging. The oxygen micro bubble dynamics, including bubble nucleation, growth and detachment, are revealed. The effect of operating parameters such as current density on rapid oxygen evolution reactions is also investigated. This research captures different flow pattern of microfluidics in flow channel under different parameters. In this research, the channel size, wettability, flow rate effected on the microfluidics pattern are investigated.

6.2 Materials and methods

In a conventional PEMEC, both end plates are made of aluminum. The anode current distributor with a parallel flow field is fabricated from a titanium plate, while the cathode current distributor is a simple titanium plate and flow field is fabricated from graphite. To develop a transparent PEMEC, a rectangle hole is opened in the middle of anode end plate as an observation window. Moreover, to introduce the light when take the optical image, both sides of window is sloped towards the edge of end plate; second, break down the titanium anode current distributor with a parallel flow field into two parts, one is transparent block with flow-in channels, the other one is a thin titanium plate with throughout flow pattern. The anode LGDL is titanium mesh, in this testing set-up, the microfluidics on the surface of catalyst layer and flow in the micro channel can be captured

by high-speed camera. Both anode and cathode gaskets are made from PVC sheets. The cathode LGDL is Toray 090 carbon paper treated with 5% PTFE. The anode LGDL is Titanium mesh. The CCM is Nafion 115 film with Ru/Ir and Pt employed as anode and cathode catalysts loading of 3.0 mg/cm2 respectively. Eight evenly distributed bolts assembled the cell to torque of 40 lb/in [27, 71, 139].

To directly visualize the oxygen evolution reactions in the middle of the PEMEC, some developments were made compared to a conventional PEMEC, as shown in Figure 6.3. First, at anode side, a rectangular hole was machined on the end plate as an observation window, similar to the transparent proton exchange membrane fuel cell in our previous work [111, 130, 131]. Second, the titanium anode current distributor with a parallel flow field was decoupled into two parts: a transparent plate with flow-in holes/channels, and a 0.5 mm thickness titanium plate with chemically etched parallel flow channels of 1 mm in channel width. Local reaction activities can be monitored and quantified based on micro-scale oxygen production in transparent/operational PEMECs by HMVS, as shown in Figure 6.3. In the transparent electrolyzers, the anode LGDL, flow fields with current distributors are made by chemically through etching titanium plates to form flow channels with lands for current distributions. They are capped by transparent plates and visually accessed through a rectangle window in the aluminum end plate.

To overcome the corrosion inside the PEM electrolyzer cell, the anode LGDL is usually made from titanium felt or titanium foam, which block the optical access to the surface of catalyst layer [80, 110]. This problem was solved by choose a novel designed Ti thin/well tunable anode LGDL. This novel Ti thin/well tunable anode LGDL was developed by using micro-/nano-fabrications on thin titanium film with a thickness of less than 50 μm [42, 46].

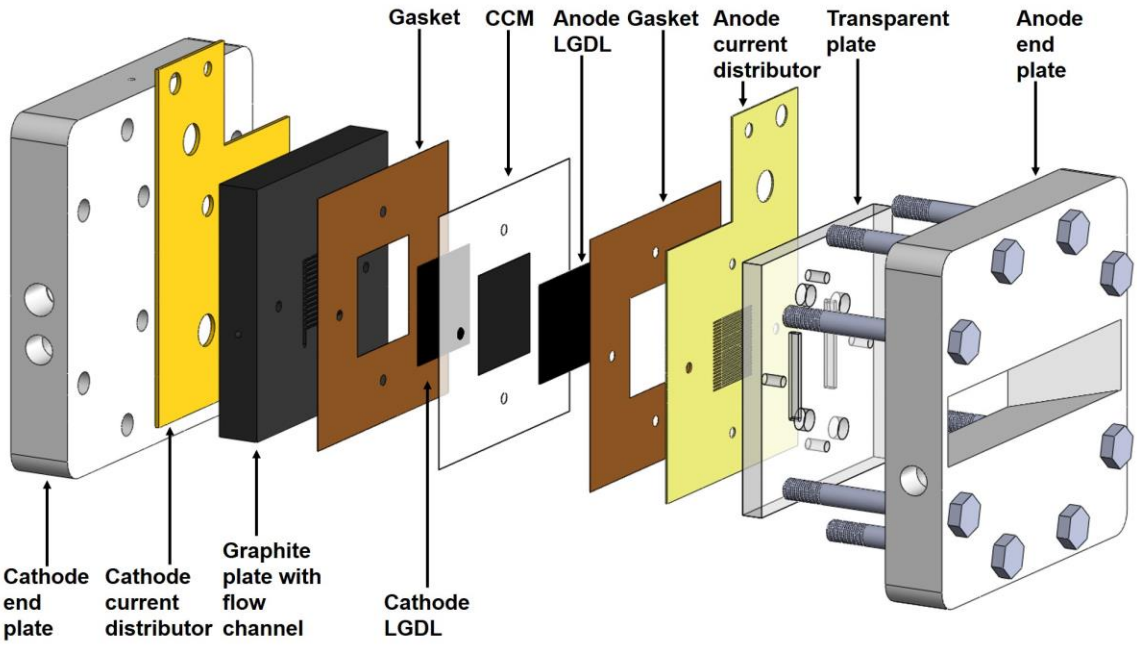


Figure 6.3. Schematics of a transparent proton exchange membrane electrolyzer cell.

Typically, the thin/well-tunable titanium LGDLs are manufactured by lithography, which using lithographically patterned photoresist masks and chemical wet etching thin foils [140]. The main steps include patterning, developing, etching and photoresist removal. More details as show in Figure 6.4 can be found in our previous work [82].

Besides the development of components from conventional PEMEC, a HMVS as shown in Figure 6.5 is also a very critical part of whole system, which includes a high-speed camera Phantom V711 and an in-house assembly long working distance microscope system. With the high-speed camera V711, the system can capture a maximum speed of 1,400,000 frame per second with the FAST option. The in-house optical assembly consists of a main zoom lens body and a series of magnification tube, objective and eye-piece lenses, with a working distance of greater than 70 mm even at high resolution. This feature differentiates it from a conventional microscope, which requires a much smaller working distance at a similar spatial resolution. The HMVS allows a large working distance with a spatial resolution of better than 5 μm and time resolution of 7530 fps at full resolution. Therefore, it provides capabilities to identify reaction activities *in-situ* and quantify oxygen productions in different locations in micro scale with the development of transparent engines/devices.

All equipments was fastened on XYZ stages and positioners with well-designed layout and control. The relative distance between the observation window of transparent PEMEC and HMVS can be fine regulated. Also, a cold light source with gooseneck and adjustable intensity was introduced to this system to make sure getting best quality of video and picture. With all those equipment and design, every phenomenon in each spot of observation window can be caught by this system. So, the local reaction activities inside

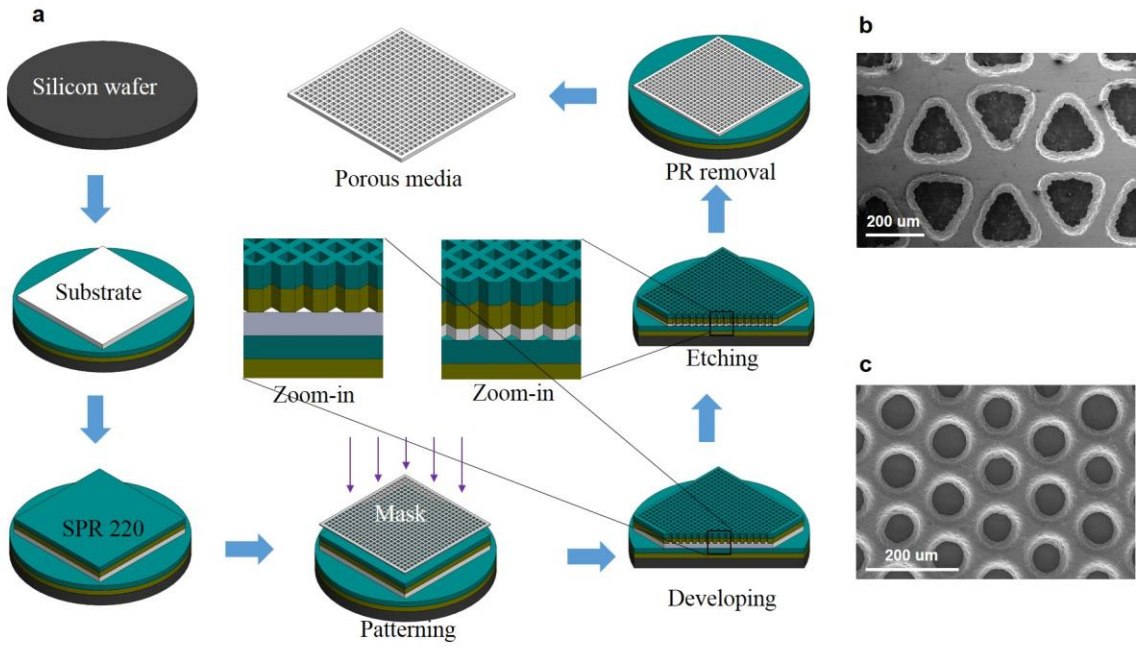


Figure 6.4. Schematic of the thin/well tunable LGDL fabrication process and SEM images of fabricated LGDLs.



Figure 6.5. Schematic of a high-speed, micro-scale visualization system.

an operating PEMEC can be monitored and analyzed based on micro-scale oxygen bubble evolution in a specific designed transparent PEMEC coupled with HMVS.

To continuously supply the deionized water, a specific designed whole plastic piping system, to avoid any metallic contamination was connected to the PEMEC. While the cathode piping was to safely exhaust the hydrogen gas, which generated during electrolysis of water, a diaphragm liquid pump SIMDOS 10 was equipped to circulate the deionized water for electrochemical reactions at a desired volumetric flow rate of 40 ml/min through the anode. During the experiments of PEMECs, all electrochemical parameters were controlled by a Bio-Logic potentiostat of a SP-300 chassis with a 10 A / 5 V booster kit. In order to get the general phenomena of oxygen bubble evolution in PEMECs, the main parameters of the transparent PEMEC as shown in Table 6.1 have been identically the same as the conventional one.

Table 6.1 Main parameters in experiments

Description, symbol	Value, unit
Liquid phase pressure, p_l	$1.013\times10^5\ \mu/m^2$
Contact angle of LGDL, θ	70°
Operating current density, i	$2.0\ A/cm^2$
Operating temperature, T	$20/80\ ^\circ C$
Bubble pressure, P_b	$1\ atm$
Active area, A	$5\ cm^2$
Flow channel width (anode), w_A	$1.0\ mm$
Flow channel depth (anode), d_A	$500\ \mu m$
Flow channel width (cathode), w_C	$1.0\ mm$
Flow channel depth (cathode), d_C	$1.0\ mm$
Flow velocity of liquid water in channel, v	$40\ ml/min$

6.3 Results and discussion

In the experiments, the PEMEC is operated under room temperature which was controlled at 20 ℃. To get the effect of different current densities on phenomena of electrochemical reactions, a set of current densities of 0 – 2 A/cm^2 were applied. The volumetric rate of deionized water circulated through the PEM electrolyzer cell is 40 ml/min. The video and images are captured in an operating PEMEC. The images, as shown in Figure 6.6, are captured in a microchannel with 1000 μm width and 500 μm depth, and the thin/well tunable LGDL is 50 μm in thickness, which has the circular throughout pores with 800 μm in diameter. During operation, the microchannel of PEMEC is fully filled with deionized water. The circular marks in Figure 6.6 indicate the locations of oxygen bubble nucleation, growth and detachment. In Figure 6.6 (i), a small oxygen bubble just nucleate; in Figure 6.6 (ii), the oxygen bubble grows to a bigger one; while in Figure 6.6 (iii), the bubble grows big enough and detaches from the rim of LGDL, start to moving with flowing deionized water from right to left. This phenomenon is the typical type of oxygen bubble nucleation, growth and detachment in the anode microchannel of PEMECs during electrolysis.

From Figure 6.6 a(iii), b(iii) and c(iii), it also can be seen that, the number of oxygen evolution reaction sites increase along with the increment of current density. When the PEMEC is operating under the current density of 0.02 A/cm^2, only one oxygen bubble generation site is observed along the rim of pore, and as shown in Figure 6.6 (a), and the bubble growth rate on red mark is about 14.09 μm/s; while the PEMEC is operating under the current density of 0.2 A/cm^2, there are three oxygen bubble generation sites observed along the rim of pore, which also include the one observed under the current density of 0.02 A/cm^2, and as shown in Figure 6.6 (b), and the bubble growth rate on red mark is

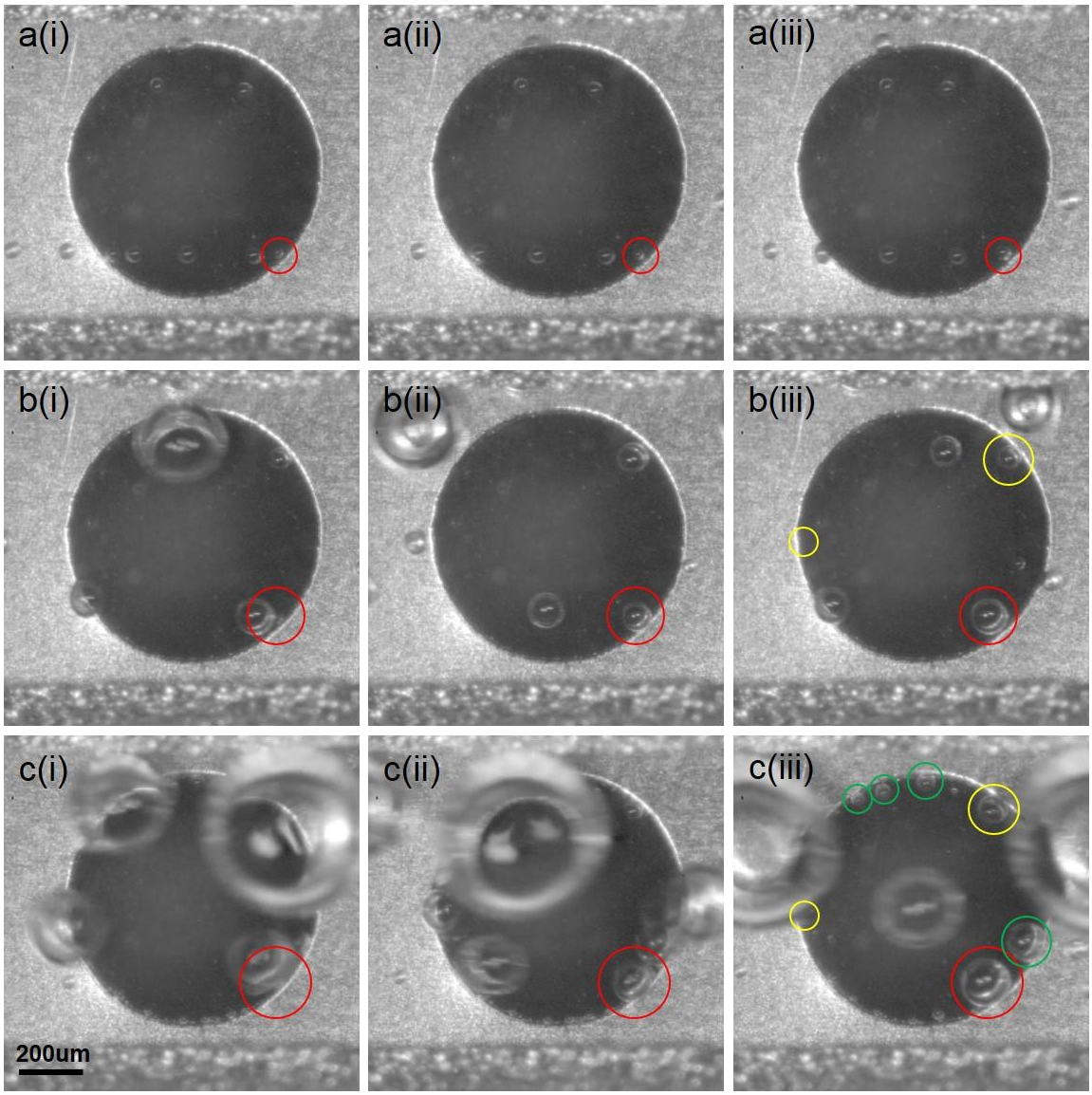


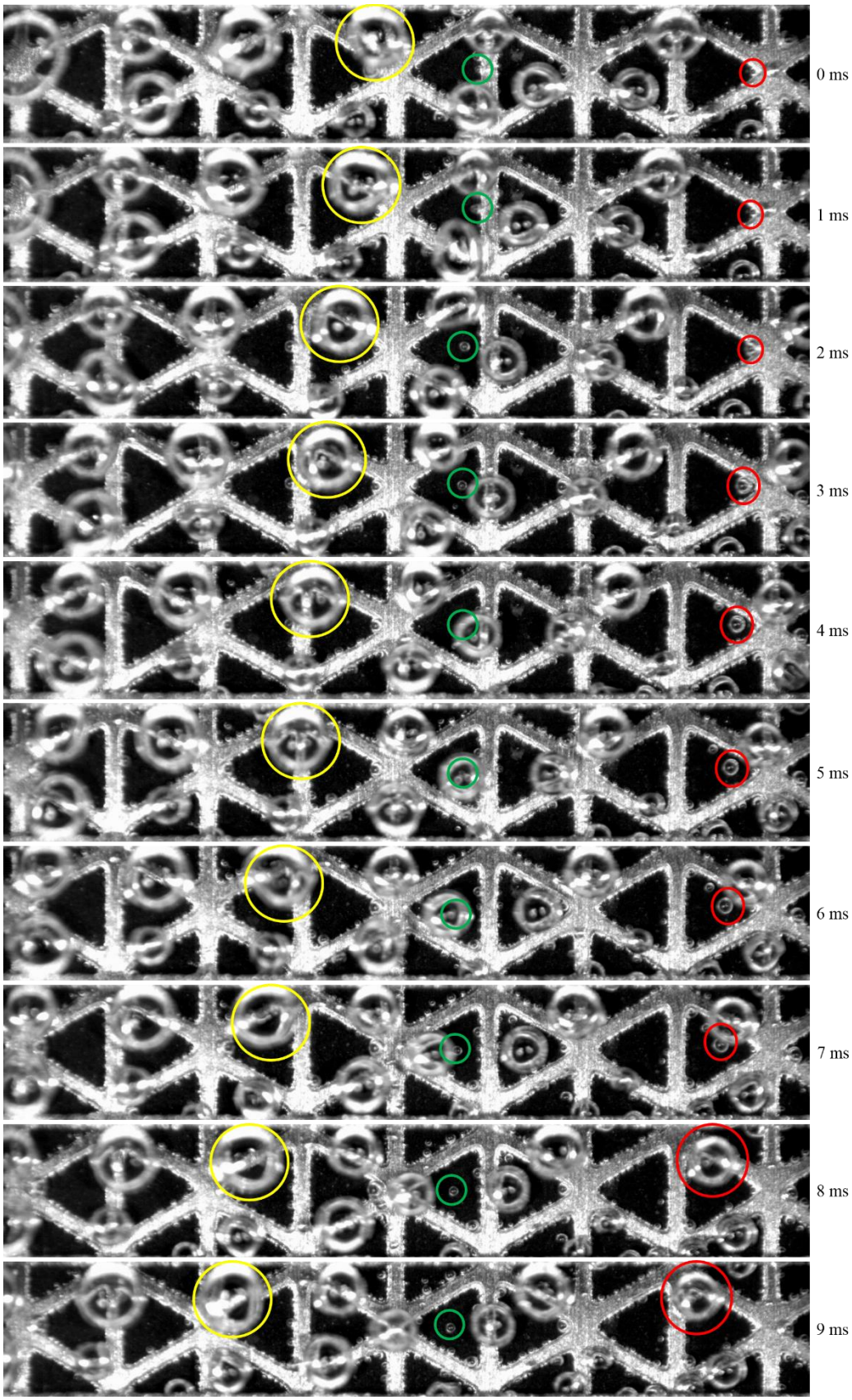
Figure 6.6. Sequence of photos for oxygen bubble generation, growth and detachment in a micro circular pore of an operating PEMEC under different current densities of (a) 0.02 A/cm^2, (b) 0.2 A/cm^2 and (c) 2 A/cm^2; the time interval between each picture (i-ii-iii) in sequence: (a) is 1.0 ms, (b) is 4.7 ms, and (c) is 2.3 ms.

about 23.42 μm; when the PEMEC is operation under the current density of 2.0 A/cm^2, there are about seven oxygen bubble generation sites observed along the rim of pore, which including all the aforementioned oxygen bubble generation sites, and the bubble growth rate on red mark is about 30.46 μm.

The images shown in Figure 6.7 is captured in a microchannel with 1000 um height and 500 um width, and the LGDL is a 50-um thickness thin titanium foil with throughout triangle pores. The microchannel of PEMEC is filled with water at a flow speed of around 5.87 cm/s. The major flow pattern in microchannel of PEMEC is bubbly. The red marks in Figure 6.7 track the phenomena of bubbles generation, growing, detaching and merging into a big bubble. At 0 ms, a small bubble just generated; at 3 ms, the bubble grows big enough and starts to detach from the surface of CL and edge of the land of LGDL; at 7 ms, the bubble just encounters a big flowing from upstream and merged into this big bubble. The capillary pressure is considered to play critical roles for gas bubble detachment, which is similar to liquid water removal in PEM fuel cells [111].

The yellow and green marks in Figure 6.7 show the big bubbles and small bubbles are flowing in different flow planes. The move speed of bubbles is also different, which is closely related to bubbles' location and bubbles' size. At 0 ms, there is a tiny bubble generated, as marked in green; at 1 ms, the bubble starts to detach from the land of LGDL; at 4 ms, the small bubble was caught up by a big bubble from upstream; at 7 ms, the big bubble passed by the small bubble. This phenomenon shows the bubbles are moving along with the flowing water at different flow planes. The move speeds of bubbles in different flow planes are also different, since in this micro flow channel, the water flow should be undeveloped laminar flow. The yellow marks in Figure 6.7 show the deformation of bubble

Figure 6.7. A sequence of images of two-phase flow in the anode microchannel of an operating PEMEC.

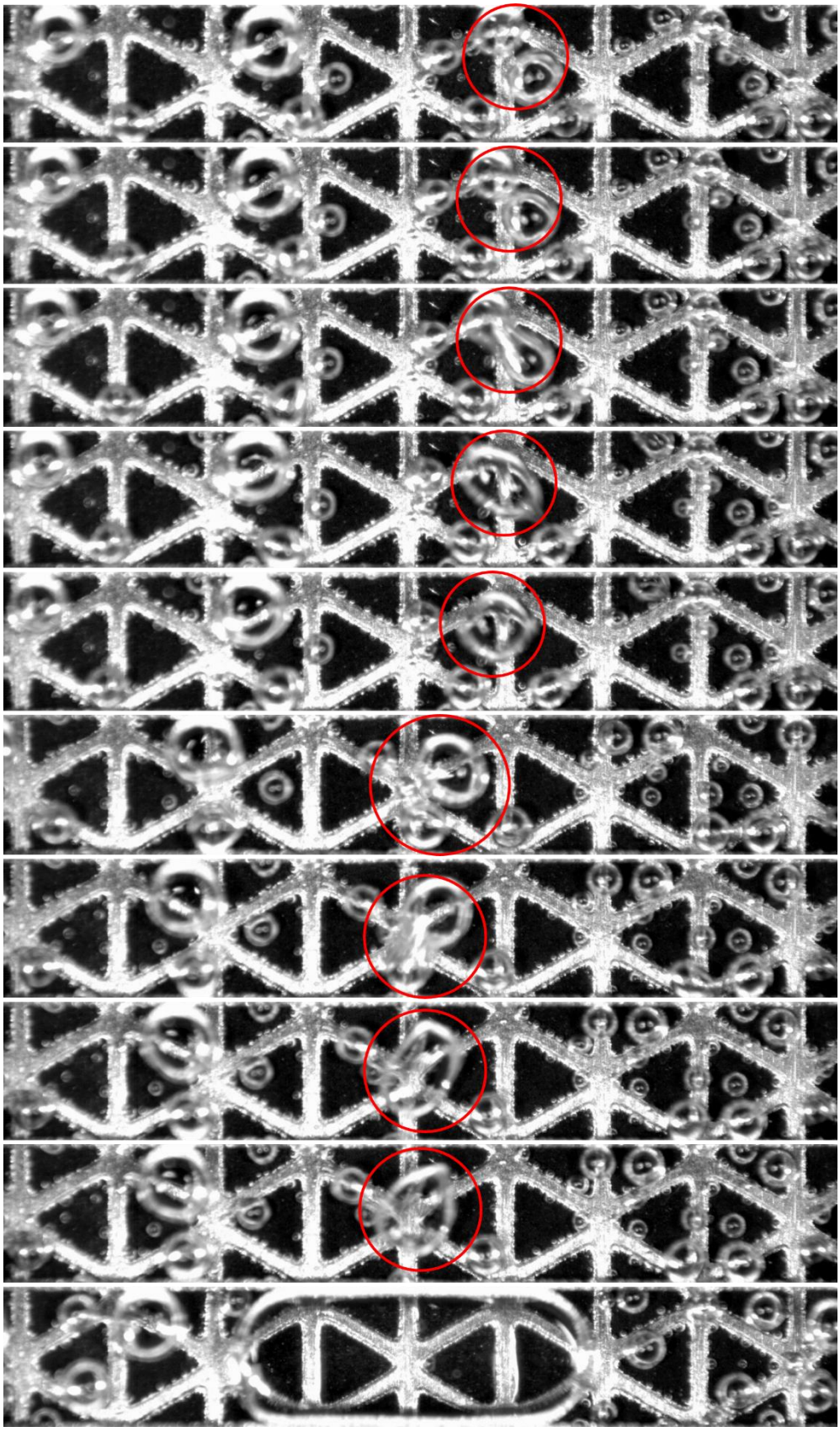

0 ms
1 ms
2 ms
3 ms
4 ms
5 ms
6 ms
7 ms
8 ms
9 ms

when another bubble is merging into the bubble. At 5 ms, there is a big bubble moving close to a small bubble; at 6 ms, the small bubble start to merge into the big bubble, and both two bubbles start to deform; at 7 ms, the small bubble has already merged into a big bubble, however, the big bubble is still in deformation, at 8 ms, the bubble goes back to the stable shape.

Beside the bubbly flow pattern, another major flow pattern in microchannel of PEMEC is slug. As shown in Figure 6.8, the red marks track the bubbles keep merging together and then form a slug in microchannel of a PEMEC.

The visualization results perfectly present the bubble nucleation, growth, detachment and transport. The clips show bubbles nucleation near the edge of titanium thin/well tunable LGDL, which meet the requirements of triple-phase boundary for electrochemical reaction. In our experiments, the early stage of bubble growth is in a very short period and shorter than the period between frames obtained by high speed camera. Under the same current density, the oxygen generate rate at each reaction site will keep at the same a certain level. As shown in Figure 6.9, all frames show bubble detach moment under different current density. All bubbles marked by red circle are generated at the same location. In Figure 6.9 (A), the PEMEC was operated under the current density of 0.02 A/cm^2, while the detach diameter of bubble is 49.58 um; In Figure 6.9 (B), the PEMEC was operated under the current density of 0.2 A/cm^2, while the detach diameter of bubble is 108.17 um; In Figure 6.9 (C), the PEMEC was operated under the current density of 0.4 A/cm^2, while the detach diameter of bubble is 119.44 um; In Figure 6.9 (D), the PEMEC was operated under the current density of 0.8 A/cm^2, while the detach diameter of bubble is 123.94 um; In Figure 6.9 (E), the PEMEC was operated under the current density of 1.6 A/cm^2, while the detach

Figure 6.8. A sequence of two-phase flow pattern changed in the anode microchannel of an operating PEMEC.



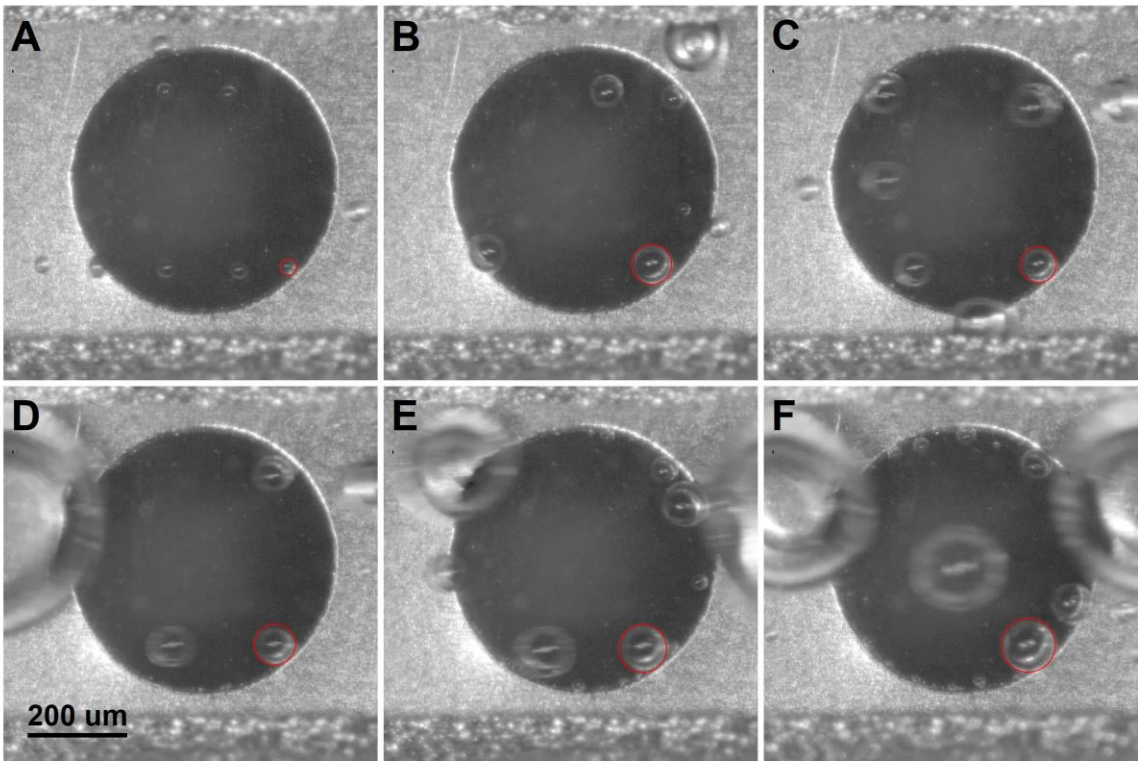


Figure 6.9. Oxygen bubble detach diameters in the microchannel of PEMECs under different current densities of (a) 0.02 A/cm^2, (b) 0.2 A/cm^2, (c) 0.4 A/cm^2, (a) 0.8 A/cm^2, (b) 1.6 A/cm^2, and (c) 2.0 A/cm^2.

diameter of bubble is 144.23 um; In Figure 6.9 (F), the PEMEC was operated under the current density of 2.0 A/cm^2, while the detach diameter of bubble is 162.25 um. According to those experimental result, it can be concluded that, the bubble detach diameter increase along with the increase of operation current density.

6.4 Conclusion

Based on the present observations, it can be concluded that the number of the bubble nucleation sites increase along with the increment of current densities. The bubble nucleation sites are determined by several factors, including triple phase boundary and roughness of surface, which are the two critical essential for oxygen bubble nucleation in PEMECs [122]. The roughness of surface of catalyst layer is enough for bubble nucleation. The surface of catalyst layer exposed to water is meet the requirements of triple phase boundary. However, the oxygen bubble nucleation site only observed along with the rim of pores. It was found out that the sheet resistance of titanium LGDL is much less than the in-plane resistance of anode catalyst layer, which means that electronic conductivity is the threshold of oxygen bubble evolution at anode of PEMEC. In this study, the real phenomena of oxygen bubble evolution are revealed for the first time in a novel designed transparent PEMEC coupled with a high-speed and micro-scale visualization system (HMVS). From the captured photos and clips, the oxygen bubble evolution occurred at the triple phase boundary can be observed clearly, and the relationship between oxygen evolution reaction sites and current density was revealed. The oxygen evolution reaction sites only along the rim of pore of titanium LGDL. With the increasing of the current density, the oxygen bubble growth rate increased, meanwhile, the oxygen bubble detach diameters also increases. The phenomena of triple-phase boundary reactions and oxygen

bubble evolution captured on catalyst layer inside the microchannel of an operating PEMEC can help to understand the behavior of electrochemical reactions and microfluidics, which can be aid to optimize the design of catalyst layer fabrication and the design of flow field, and consequently improve the performance and efficiency of PEMECs. The future work will focus on the quantification investigation of oxygen bubble evolution and modeling of two-phase microfluidics in PEMECs and the influence of flow pattern on the performance. The data of performance and combination of parameters can be an instruction to optimize the design of PEMEC and validate the mathematical modeling of two-phase flow inside PEMECs

CHAPTER 7

MATHMATICAL MODELING INVESTIGATION ON OXYGEN BUBBLE EVOLUTION IN PEMECs

7.1 Introduction

A proton exchange membrane electrolyzer cell (PEMEC), which can produce highly pure hydrogen from water via electrolysis, will play an important role in renewable energy conversion and utilization in the near future. Compared with alkaline and solid oxide electrolysis technologies, a PEMEC has more advantages, such as high energy efficiency/density and environmentally friendly operation [76, 141-145]. Figure 7.1 show a schematic of a single PEMEC and its microstructure, which consists of several key components, including bipolar plates, porous liquid/gas diffusion layers (LGDLs) and catalyst layers where electrochemical reaction and multi-phase transport occur, and PEM. During electrolysis, the liquid water is fed into flow channel at the anode side and then invades into the porous LGDL. As the liquid water reaches the catalyst layer (CL), the electrochemical reaction will occur, which produces oxygen and protons as well as consumes the water, as shown in Figure 7.1. The basic reaction of a PEMEC can be expressed as follows:

$$\textit{Anode: } H_2O \rightarrow 2H^+ + 2e^- + \frac{1}{2}O_2 \qquad (24)$$

$$\textit{Cathode: } 2H^+ + 2e^- \rightarrow H_2 \qquad (25)$$

$$\textit{Total reaction: } H_2O_{(liquid)} \xrightarrow{electricity,\ catalyst} \frac{1}{2}O_2 + H_2 \qquad (26)$$

As water electrolysis progresses, a large number of oxygen bubbles will be produced at

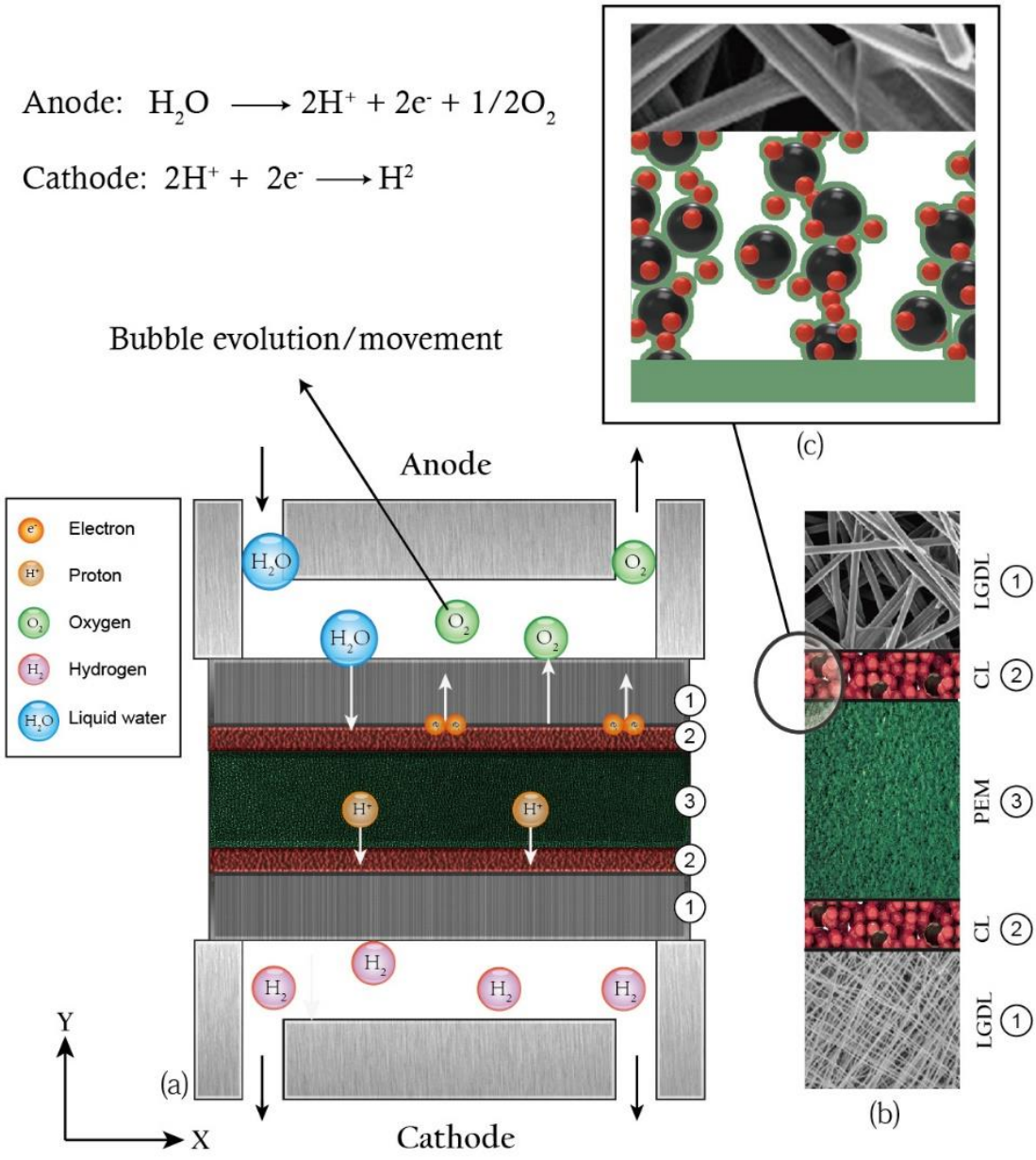


Figure 7.1. Schematics of gas/liquid two-phase transport and microstructure in a PEMEC.

the anode side due to the electrochemical reaction. These bubbles will flow across the liquid/gas diffusion layer and enter the flow channel where the bubbles can get out of the cell under the assistance of the flow liquid water. If the bubbles are not removed properly and adequately, gas will accumulate inside the LGDL and flow channel and form a transport barrier near the CL, which will consequently lead to a poor cell performance. Therefore, it is very important to manage gas bubble transport in a PEMEC. In addition, as mentioned in the previous paper [121, 139, 146-149], characteristics of gas-liquid two-phase transport have a significant effect on the cell performance and design optimizations and gas bubble dynamics is crucial to the fundamental understanding of two-phase transport process. Therefore, gas bubble dynamics and management in the flow channel and LGDL is an important issue in a PEMEC. In order to address this issue, bubble dynamic behaviors including growth and detachment should be investigated under different operating conditions. However, it is still hard to exactly measure the behaviors of bubble growth and detachment in an electrochemical reaction system. An accurate mathematical model is needed to predict and understand the gas bubble evolution in a PEMEC. In the PEMEC, LGDL is located between the catalyst layer and current-distributing layer with flow field. The purpose of the LGDL is to transport electrons, heat, and reactants or products to and from the catalyst layer with minimal voltage, current, thermal, interfacial, and fluidic losses [106-113]. At the anode side of PEMEC, as mentioned before, the multi-phase boundary interfacial reactions need water flow into the LGDL and the generated oxygen gas needs to get out of CLs through the LGDL. During this process, the two-phase flow occurs, which significantly affect the performance. A better fundamental

understanding of interfacial effects becomes critical for controlling two-phase transport and enhancing performance and efficiency.

Theoretically, bubble evolution consists of several stages, including nucleation, growth, and detachment [150-152]. Nucleation is a process that leads to the formation of a new phase in a liquid solution. The new phase is often presented by gas bubble form. The process is related to operating conditions and structure parameters of a system, such as temperature, pressure, and contact angle, which is still difficult to be quantitatively predicted and measured. This paper will focus on the dynamics of growth and detachment of gas bubble. In recent years, models regarding gas bubble dynamics have been also conducted to investigate the gas bubble growth and detachment behaviors in different applications, which are very helpful to the present study. Early models usually used some empirical relationships or a simple force balance analysis that only considered the limited forces acting on the gas bubble, due to the complexity of gas bubble generation. Lubetkin [153] investigate the motion of gas bubble near electrodes. Fritz et al. [154, 155] first proposed an empirical formulas for calculating the detachment diameter of gas bubble. This relation is only suitable for stagnant gas bubble on a surface and the detachment diameter is mainly related to surface tension force and buoyancy. Chen et al. [156] simulated the gas bubble dynamics on a heat surface using a force balance analysis model. In their model, a new force called dynamics force was introduced, which was considered the sum of liquid inertia, gas inertia, and drag force. Klausner et al. [157] and Chen et al. [158] presented a more detailed analysis of different forces acting on a single gas bubble and predicted the bubble detachment diameter. According to their studies, nine forces were taken into account to analyze the bubble dynamic behavior, including body force, surface

tension, buoyancy, capillary pressure, added-mass force, quasi-steady drag force, shear lift force and reaction force. In order to determine the lift-off and departure diameters, the equations in x and y directions were simultaneously solved.

Meanwhile, some experiments have conducted to investigate the phenomena of bubble evolution. Most investigations [14, 159-163] were conducted to macroscopic performance evaluation, optimization of membrane electrode assembly and mass transport, and electro-catalyst. For investigation on dynamics of bubble evolution, most of them are focus on bubble evolution in boiling system or from a nozzle [164, 165]. A few attentions have been paid to gas bubble dynamics during water electrolysis. Sakuma et al. [166] experimentally observed the nucleation and growth of single oxygen bubble in potassium hydroxide solution under microgravity. Their results indicated that the initial bubble diameter ranged from 10 to 30 microns depending on the surface contact angle. Matsushima et al. [167] also reported the growth characteristics of single gas bubble on a platinum micro-electrode surface. The growth rate of bubble during water electrolysis was mainly controlled by the gas evolution efficiency that was related to transient current density and gas volume. Chandran et al. [168] experimentally investigated hydrogen bubble formation and its distribution near the electrode surface during water electrolysis. It was found that the bubble diameter near the electrode would decrease constantly before it reached a steady state. Liu et al. [169] examined the growth and detachment of hydrogen bubble on a 200 μm micro-electrode as the current density ranges from 15.9 to 57.3 A/cm^2. They found that the gas bubble would be easier to release from the electrode surface with the current density increasing without magnetic field. Yang et al. [170] used a microscope by a high-speed camera to observe the lifetime and size of single hydrogen bubble on a platinum

microelectrode. Other investigators [153, 171-175] also analyzed the bubble formation and evolution mechanisms during water electrolysis. Although some work has been conducted to gas bubble dynamics of water electrolysis, it can be seen that most of them are experimental studies and it is still difficult to experimentally measure and capture the detailed bubble evolution process inside the LGDL and CL during PEMEC operation due to the complex of CL structure and cell operating conditions. Because of limitation, a full mathematical model is highly needed to deeper understand the gas bubble evolution in a PEMEC.

Direct visualization of electrochemical reactions that occur in PEMEC necessitates the development of alternative methodologies for *in-situ* characterization and is critical to further develop fundamental understanding of the microfluidics in micro channels and pores and associated transport phenomena [176]. Since the oxygen bubble moves fast inside the micro pores/channels, it's necessary to use high-speed camera to capture the phenomena.

In this paper, based on a detailed force balance analysis and visualization experiment of oxygen bubble evolution in an operating PEMEC, a full mathematical model for gas bubble dynamics is developed and validated to study the growth and detachment behaviors of oxygen bubble generated from the catalyst layer surface at the anode side of a PEMEC, mainly focusing on the effects of key operating parameters on the gas bubble growth and detachment, including the effects of current density, contact angle, flow velocity and local operating temperature and pressure. Results will provide fundamental understanding of bubble evolution in an operating PEMEC and aid further research of gas/liquid two-phase transport in the LGDL and microchannel.

7.2 Methodology

7.2.1 Mathematical model of oxygen bubble growth

For a bubble in a viscous fluid, the growth process is controlled by a series of forces. Initial growth from the critical size is dominated by surface tension forces. When the inertial forces become dominant, growth is driven primarily by the difference between the vapor pressure within the bubble and the external pressure, and the volumetric growth rate is linear with time, and the growth rate of radius may be approximated by the following power law curve fit [177, 178].

$$r = Kt^n \qquad (27)$$

Where r is the diameter of the bubble, t is the growth time, K and n are empirical constants. Those constants are affected by the mass flux, which is the speed of oxygen generation; temperature and pressure. The model of bubble growth with chemical reaction in a stationary liquid has been developed by Fabelukis and Yablonsky (2004). The model assume that all gas generated by chemical reaction enter the bubble and no gas dissolves back into the liquid. In this study, the growing bubble was formed by a constant electrochemical reaction rate under the certain operation parameters. The rate of gas generation is given by,

$$\dot{n} = \frac{iA}{nF} \qquad (28)$$

Where i is current density, F is Faraday constant. The gas inside bubble is considered as ideal gas,

$$PV = nRT \qquad (29)$$

Where, P is the pressure of gas, V is the volume of the bubble, R is the universal gas constant, and T is the absolute temperature. The oxygen bubble nucleate on the surface of substrate, before the bubble detaching form the substrate, the oxygen bubble is not a sphere as shown in Figure 7.2. Based on the contact angle, the volume of bubble before detaching can be calculated as following,

$$V = \frac{1}{3}\pi r^3(2 - 3cos\theta + cos^3\theta) \quad (30)$$

Where θ is contact angle.

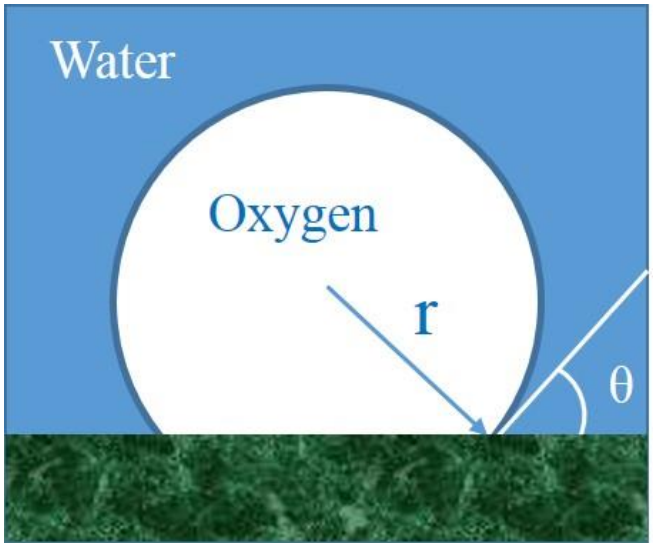


Figure 7.2. Schematic of bubble generate and growth on the surface of substrate.

The ideal gas equation can be differentiated with respected to time and give an expression for the molar flux to the bubble,

$$P_b\frac{1}{3}\pi r^3(2 - 3cos\theta + cos^3\theta) = \dot{n}tR_gT \quad (31)$$

So, the bubble radius can be expressed by,

$$r = (\frac{3}{\pi}\frac{iA}{nF}\frac{R_gT}{P_b(2-3cos\theta+cos^3\theta)}t)^{1/3} \quad (32)$$

And the bubble growth velocity is,

$$\frac{dr}{dt} = \frac{3}{\pi r^2}\frac{iA}{nF}\frac{R_g T}{P_b}(2 - 3cos\theta + cos^3\theta) \quad (33)$$

And the change rate of bubble velocity *is,*

$$\frac{d^2r}{dt^2} = -\frac{6}{\pi r^3}\frac{iA}{nF}\frac{R_g T}{P_b}(2 - 3cos\theta + cos^3\theta) \quad (34)$$

7.2.2 Mathematical model of oxygen bubble detachment

Figure 7.3 shows a schematic of bubble force analysis and detachment on a hydrophilic LGDL surface of a PEMEC. Different forces acting a growing gas bubble are analyzed at x and y directions. As the gas bubble grows, the gas bubble will detach from the original nucleation site when the force balance is broken.

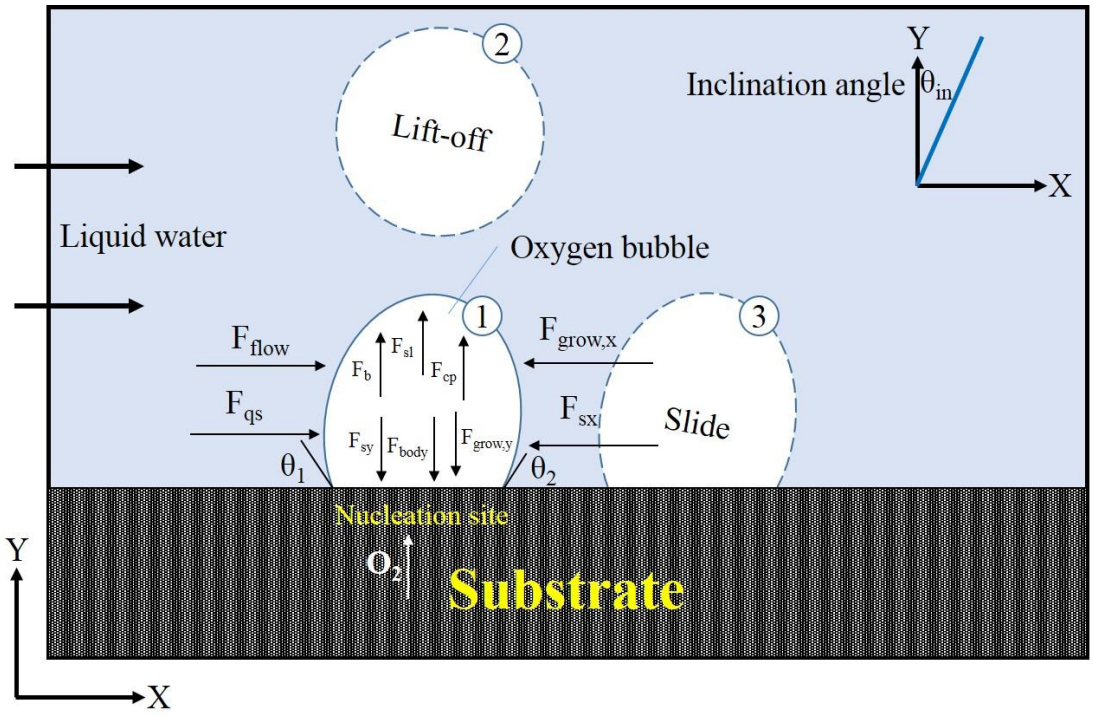


Figure 7.3. Schematic of bubble force analysis and detachment situations on a LGDL surface.

The present detachment model for gas bubble is based on a force balance, which analyzes all forces acting on a growing gas bubble in two directions. The forces acting on the bubble can be expressed as the following general form:

$$\sum \vec{F} = \vec{F}_{body} + \vec{F}_{flow} + \vec{F}_{grow} + \vec{F}_b + \vec{F}_s + \vec{F}_{cp} + \vec{F}_{sl} + \vec{F}_{qs} \quad (35)$$

Where, $\vec{F}_{body}$ is gravity, $\vec{F}_{flow}$ is flow induce force, $\vec{F}_{grow}$ is grow induce force, $\vec{F}_b$ is buoyance fore, $\vec{F}_s$ is surface tension force, $\vec{F}_{cp}$ is contact pressure force, $\vec{F}_{qs}$ is quasi steady drag force. For a growing gas bubble, as shown in Figure 7.3, the following equations based on the force balance can be obtained:

For x direction:

$$\sum F_x = F_{flow} + F_{grow,x} + F_{sx} + F_{qs} \quad (36)$$

The force due to fluid flow [179] can be calculated as:

$$F_{flow} = 2\pi\rho_l r^2 u_x \dot{r} \quad (37)$$

The bubble growth force in x directions [158, 180] is calculated as:

$$F_{grow} = -\pi {r_b}^2 \rho_l (r\ddot{r} + \frac{3}{2}\dot{r}^2) \quad (38)$$

$$F_{grow,x} = F_{grow} \sin\theta_{in} = -\pi {r_b}^2 \rho_l (r\ddot{r} + \frac{3}{2}\dot{r}^2) \sin\theta_{in} \quad (39)$$

The surface tension force in x direction [157] can be calculated as:

$$F_{sx} = -2.5 r_b \sigma \frac{\pi(\theta_1 - \theta_2)}{\pi^2 - (\theta_1 - \theta_2)^2} (\sin\theta_1 + \sin\theta_2) \quad (40)$$

While, the surface tension coefficient [181] is,

$$\sigma = 235.8\times10^{-3}(1 - \frac{T}{T_C})^{1.256}\left[1 - 0.625\left(1 - \frac{T}{T_C}\right)\right] \quad (41)$$

Where, the critical temperature T_C is 647.15 K.

The quasi steady drag force [157]:

$$F_{qs} = 6\pi\mu_l u_x r\left\{\frac{2}{3} + \left[\left(\frac{12}{Re_b}\right)^{0.65} + 0.796^{0.65}\right]^{-1/0.65}\right\} \quad (42)$$

The bubble Reynolds number can be defined as:

$$Re_b = \frac{2u_x r\rho_l}{\mu_l} \quad (43)$$

The total equation for bubble detachment in x direction can be written as:

$$\sum F_x = 2\pi\rho_l r^2 u_x\dot{r} - \pi r^2\rho_l(r\ddot{r} + \frac{3}{2}\dot{r}^2)\,sin\,\theta_{in} - 2.5r_b\sigma\frac{\pi(\theta_1-\theta_2)}{\pi^2-(\theta_1-\theta_2)^2}(sin\,\theta_1 + sin\,\theta_2) +$$

$$6\pi\mu_l u_x r\left\{\frac{2}{3} + \left[\left(\frac{12}{Re_b}\right)^{0.65} + 0.796^{0.65}\right]^{-1/0.65}\right\} \quad (44)$$

For y direction:

$$\sum F_y = F_{body} + F_{grow,y} + F_b + F_{sy} + F_{sl} + F_{cp} \quad (45)$$

The body force can be calculated as:

$$F_{body} = -[\frac{4}{3}\pi r^3 - \frac{1}{6}\pi h(3a^2 + h^2)]\rho_g g \quad (46)$$

The bubble growth force in y directions [158, 180] is calculated as:

$$F_{grow,y} = F_{grow}\,cos\,\theta_{in} = -\pi {r_b}^2\rho_l(r\ddot{r} + \frac{3}{2}\dot{r}^2)\,cos\,\theta_{in} \quad (47)$$

Based on Figure 7.3, the buoyancy force can be calculated as:

$$F_b = [\frac{4}{3}\pi r^3 - \frac{1}{6}\pi h(3a^2 + h^2)]\rho_l g \quad (48)$$

The surface tension force [157] can be calculated as:

$$F_{sy} = -2.5r_b\sigma\frac{\pi}{\theta_1-\theta_2}(cos\,\theta_2 - cos\,\theta_1) \quad (49)$$

The shear lift force [157]:

$$F_{sl} = \frac{1}{2}\rho_l u_x^2\pi r^2 C_l \quad (50)$$

$$C_l = 3.877G^{1/2}\left[Re_b^{-2} + \left(0.344G^{1/2}\right)^4\right]^{1/4} \quad (51)$$

$$G = \left|\frac{du_x}{dy}\right|\frac{r}{u_x} \quad (52)$$

The contact pressure [179] is:

$$F_{cp} = 2\pi r_b^2 \frac{\sigma}{r_c} \quad (53)$$

The total equation for bubble detachment in y direction can be written as:

$$\sum F_y = -\left[\frac{4}{3}\pi r^3 - \frac{1}{6}\pi h(3a^2 + h^2)\right]\rho_g g - \pi r^2 \rho_l \left(r\ddot{r} + \frac{3}{2}\dot{r}^2\right) cos\,\theta_{in} + \left[\frac{4}{3}\pi r^3 - \frac{1}{6}\pi h(3a^2 + h^2)\right]\rho_l g - 2r_b\sigma\frac{\pi}{\theta_1 - \theta_2}(cos\,\theta_2 - cos\,\theta_1) + \frac{1}{2}\rho_l u_x^2 \pi r^2 C_l + 2\pi r_b^2 \frac{\sigma}{r_c} \quad (54)$$

7.3 Results and discussion

Understanding the microfluidics in the pores of LGDLs and flow channels is vital for promoting performance and optimizing design of the PEMEC. The results will also can be used to validate the mathematics model in the future. Moreover, discovering the behavior of microfluidics in micro pores/channels has lot of applications in energy, environment and defense research fields.

The evolution and movement of gas bubble in a PEMEC involve four steps: initial nucleation, growth, detachment and transport. To understand the evolution mechanisms of gas bubble on an electrode surface in a PEMEC, the bubble growth and detachment model that are developed in the above section is used to calculate and analyze the effects of operating conditions and physical parameters on the oxygen bubble evolution behaviors on a LGDL surface, including operating pressure, temperature, and current density. It is found that when the oxygen bubble is caused by the electrochemical reaction and generated on a triple-phase boundary site, cell operating conditions and structure parameters will have significant effects on the bubble growth and detachment process and contribute significantly to gas/liquid two-phase transport behaviors in a PEMEC.

As shown in the model development, the variation of oxygen bubble radius with time can be obtained by directly solving the equation (32). In order to get the detachment diameter of oxygen bubble, equations (44) and (54) should be properly solved at two different conditions. When $\sum F_x > 0$ and $\sum F_y < 0$, bubble will depart from the initial nucleation site and slide along the LGDL surface. When $\sum F_x < 0$ and $\sum F_y > 0$, bubble will lift off the LGDL surface. In the present model, a detachment diameter of oxygen bubble can be obtained by performing an iterative computation to solve $\sum F_x > 0 \; or \; \sum F_y > 0$. The parameters used for modeling of bubble growth and detachment are shown in Table 7.1, including PEMEC geometry, material and fluid properties, and general physical parameters.

7.3.1 Effects of parameters on the bubble growth

In a PEMEC, modeling the growth of gas bubble will provide a fundamental understanding of gas removal mechanisms and the effects of gas/liquid two-phase flow. After solving equation (32), modeling of oxygen bubble growth on a LGDL surface is investigated under different initial conditions in this section, focusing on the effects of operating temperature, operating pressure, and current density.

The present calculation is based on a theoretical model for the growth of a spherical gas bubble. In this model, the gas bubble dynamics is controlled by ideal gas state equation and Young-Laplace equation. It is assumed that all gas produced by the chemical reaction enters the bubble. Since the initial stage of gas bubble growth is in a super short period, it is still difficult to observe the process of its growth.

In a PEMEC, operating temperature and pressure play important roles on the cell performance and efficiency. According to the electrochemical performance analysis of a

Table 7.1 Parameters in calculation of bubble dynamics

Description, symbol	Value, unit
Liquid water density, ρ_{H_2O}	$998.2\ kg/m^3\ \ (T = 20\ ^{\circ}C)$
Oxygen density, ρ_{O_2}	$1.1 kg/m^3$
Gravity acceleration, g	$9.8\ m/s^2$
Liquid phase pressure, p_l	$1.013\times10^5\ \mu/m^2$
Contact angle, θ	70°
Liquid water dynamic viscosity, μ_l	$0.355\times10^{-3}\ kg/(m \cdot s\ )$
Operating current, i	$2.0\ A/cm^2$
Operating temperature, T	$20\ ^{\circ}C$
Faraday constant, F	$96485.0\ \ c/mol$
Gas constant, R	$8.314\ J/(mol\ k)$
Bubble pressure, P_b	$1.01325\times10^5\ Pa$
Active area, A	$5\ cm^2$
Flow channel width (anode), w_A	$1\ mm$
Flow channel depth (anode), d_A	$500\ \mu m$
Flow channel width (cathode), w_C	$1\ mm$
Flow channel depth (cathode), d_C	$1\ mm$
Flow velocity of liquid water in channel, v	$40\ ml/min$
Bubble growth time, t_g	$10\ ms$

PEMEC, open circuit voltage, activation and diffusion over-potential, and ohmic loss are closely related to the operating temperature. Calculations confirm that increasing the operating temperature will decrease the total cell voltage and consequently improve the PEMEC performance. Further analysis shows that the activation over-potential will decrease with increasing the operating temperature, which might be related to gas/liquid two-phase transport dynamics. In the present model, the bubble growth rate is closely related to the operating temperature according to equation (32). Before we use this mathematical model to predict the trend of bubble growth and detachment, the model is computed and validated with our previous visualization experimental data. Figure 7.4 presents the comparison of the model data and experimental data for oxygen bubble growth inside a PEMEC, under the same operation parameters. The numerical results obtained from the model show good agreement with the experimental results.

As shown in Figure 7.5, the effects of cell operating temperature on the bubble growth radius are presented with three different values of 20°C, 50°C, and 80°C. When the time is equal to 10 ms, comparing bubble growth radius at a temperature of 20°C and at a temperature of 80°C, the bubble radius at 80°C is larger than one at 20°C, but the difference is relatively small. A similar trend can be obtained as the time gradually increases. For the time of 10 ms, the bubble radius only increases by around 8.4 μm as the operating temperature ranges from 20°C to 80°C. The results indicate that the operating temperature has little influence on the oxygen bubble growth. Figure 7.6 shows that the effects of cell operating pressure on the oxygen bubble growth radius. Three different pressure values including 1 atm, 2 atm, and 4 atm are investigated. Comparing the effects of temperature, it can be found that the cell operating pressure has a more significant influence on the

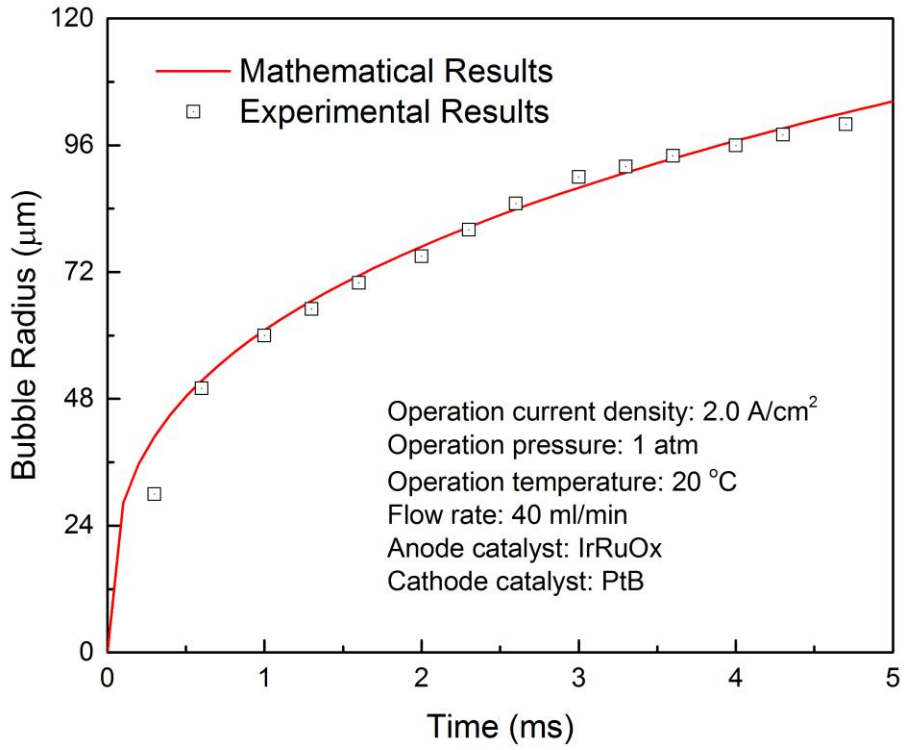


Figure 7.4. Comparison of the modeling data and experimental data for oxygen bubble growth in PEMECs.

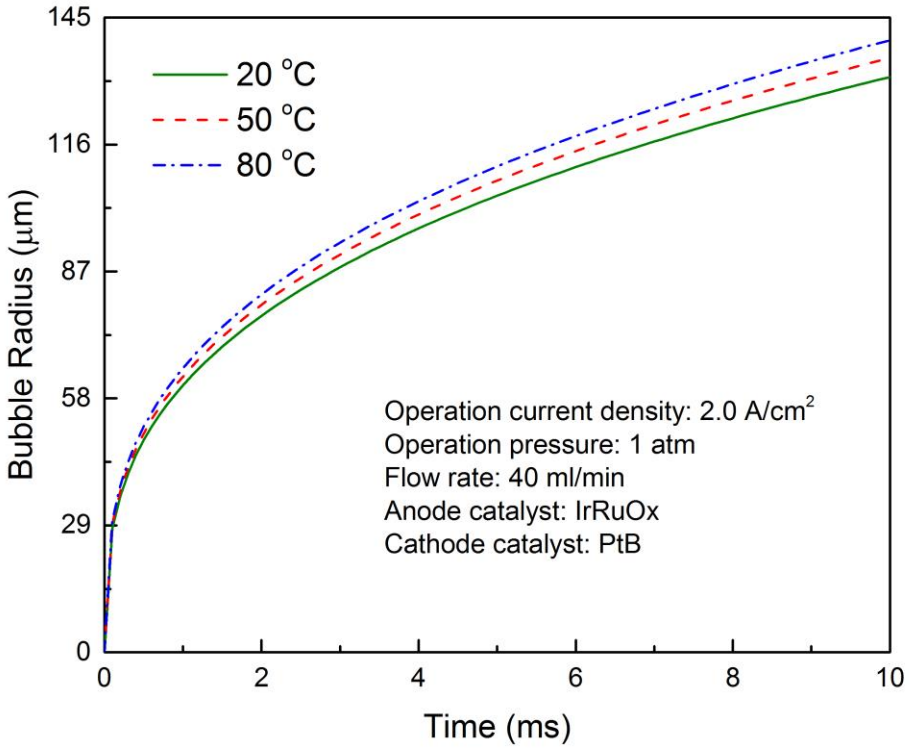


Figure 7.5. Effect of temperature on oxygen bubble growth.

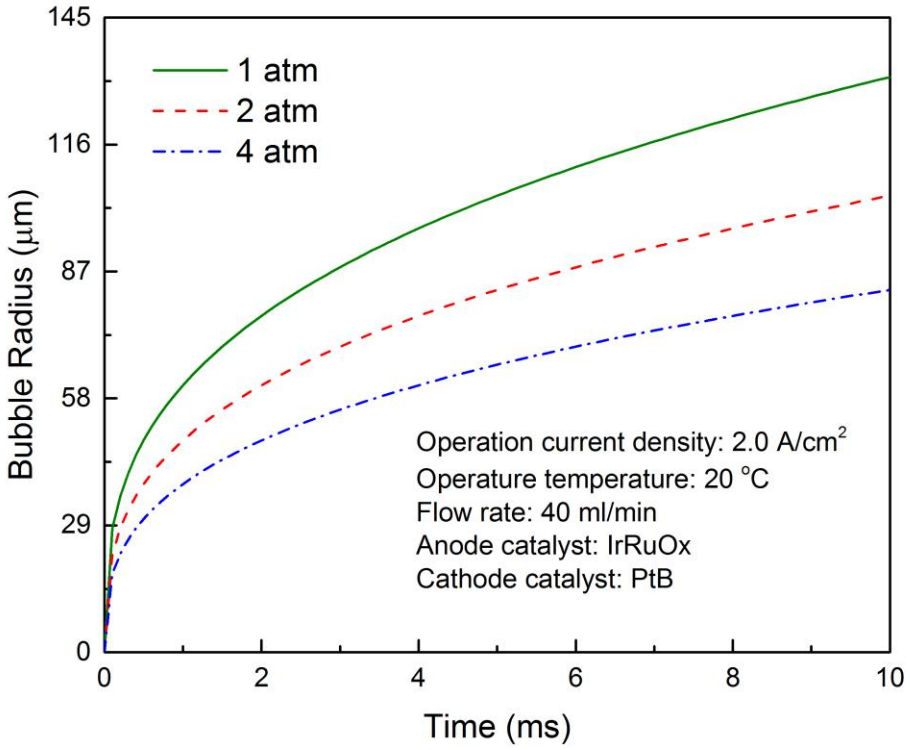


Figure 7.6. Effect of pressure on oxygen bubble growth.

oxygen bubble growth. For example, at the time of 10 ms, when the cell operating pressure is set to 1 atm, the oxygen bubble radius is 131.4 μm. As the cell operating pressure increases to 4 atm, the oxygen bubble radius is 82.8 μm. The result clearly shows that higher pressure makes it more difficult for gas bubble to grow on a nucleation site.

To get further understanding into the process of bubble growth due to the electrochemical reaction, the effects of current density on the bubble growth radius are examined. According to equation (32), gas generation rate will change with the local current density. Since the higher current density can result in more gas production caused by electrochemical reaction, it can be expected that the gas bubble will grow bigger as the current density become higher at the same time step. Figure 7.7 presents the time evolution of bubble growth radius at three different current density parameters of 0.5 A/cm^2, 1.0 A/cm^2, and 2.0 A/cm^2. It can be seen that current density has a significant influence on the oxygen bubble growth. At a low current density of 0.5 A/cm^2, the bubble radius is relatively small due to slow process of electrochemical reaction. As the current density increases, the electrochemical reaction in a CL will become faster and more gas will be generated from a nucleation site, so the gas bubble radius increases. In practice, if the current density continues to increase, more gas bubbles will be released from different nucleation sites. Therefore, in an operating PEMEC, current density should be adjusted to properly control the transport process of gas bubble.

7.3.2 Effects of parameters on the bubble detachment

The bubble detachment diameter is one of the most important parameters in the bubble evolution process. It is difficult to be measured and captured by the experimental method due to the complexity of operating condition and micro-structure in a PEMEC. This

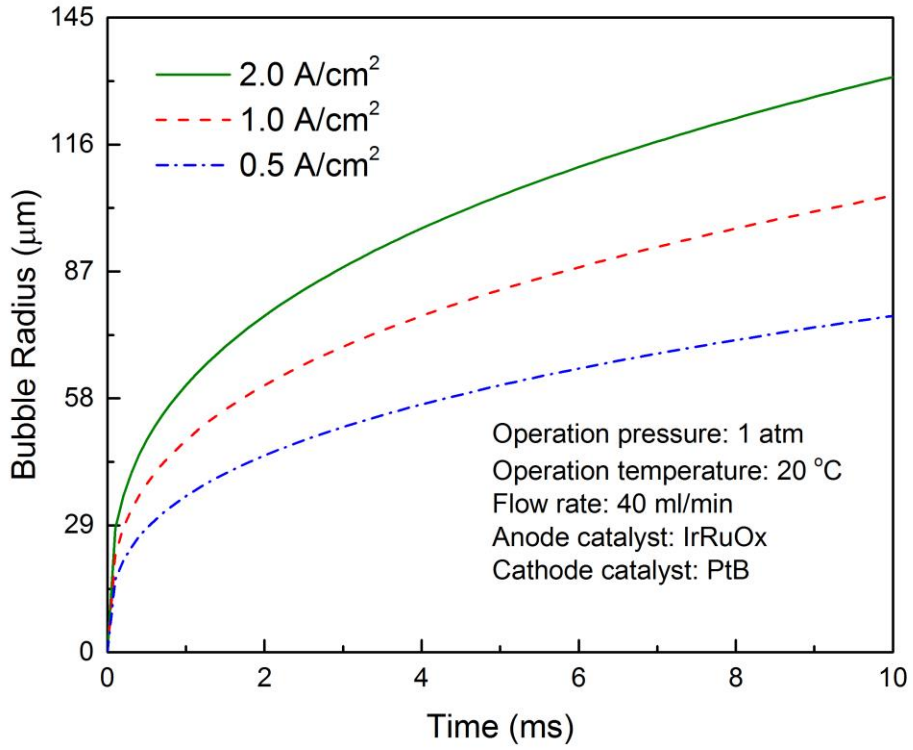


Figure 7.7. Effect of current density on oxygen bubble growth.

section will discuss the effects of cell operating parameters and flow conditions on the bubble detachment, obtained from the force balance analysis model developed in the previous section. As shown in Figure 7.3, the bubble detach diameter can be predicted by the previous mathematical model. There are two situations to define the detachment diameter, one is the diameter of bubble immediately after the first sign of sliding from the nucleation site, $\Sigma F_x > 0$, the other one is the lift off diameter, which is immediately after the bubble detaches from the surface of catalyst layer, $\Sigma F_y > 0$. In this research, bubble detach diameter is the one of those two situations which come first.

For a PEMEC, the total reaction area is 5 cm^2 ($5\times10^{-4} m^2$). In the present modeling, a reaction area of πr^2 is used to calculate the current, which makes the electrochemical reaction and produces the gas for single bubble growth. Here, r is the effective reaction radius for bubble generation and growth. Generally, since LGDL pore diameter ranges from around 100 to 1000 μm and a single bubble on the LGDL surface might be produced or fed from multiple pores, it is reasonable to choose the reaction radius of more than 1000 μm when the pore diameter is around 1000 μm. In addition, it also should be noted that the bubble detachment diameter observed from an experiment on a LGDL surface might be much larger than one from theoretical calculation, this is because bubbles generated at different nucleation sites could merge into a large bubble in an extremely short time and then detach from the LGDL surface and it is still difficult to exactly measure the detachment diameter of a single bubble from initial nucleation site inside a catalyst layer. The following modeling results will present the bubble detachment characteristics on a LGDL surface.

Figure 7.8 and Figure 7.9 present the effects of cell operating temperature and pressure on the bubble detachment. On one hand, since the velocity and acceleration of bubble growth in the detachment model is determined from the present growth model, which is related to cell operating temperature and pressure. On the other hand, the properties of gas and liquid phase are strongly corrected to local temperature and pressure. For example, the water dynamic viscosity is $1.002\times10^{-3}\ N\cdot S/m^2$ at 20°C and 1 atm. When the operating temperature increases to 80°C, the water dynamic viscosity will be $0.335\times10^{-3}\ N\cdot S/m^2$, at 1 atm. Therefore, it can be expected that the operating temperature and pressure will have an important effect on the bubble detachment. As shown in Figure 7.8, when the current density is 0.5 A/cm^2, the detachment diameter of oxygen bubble changes relatively small with increasing the temperature from 20°C to 80°C. As the current density increases, the variation of bubble detachment diameter with temperature becomes relatively significant and the detachment diameter increases as the operating temperature increases. From the modeling results in Figure 7.9, the bubble detachment diameter will significantly decrease as the operating pressure increases, which means that gas bubbles can be got out of flow channel easier. Therefore, it can be concluded that a high-pressure operation condition is beneficial to cell performance improvement.

7.4 Conclusion

To maintain the cell performance and efficiency, oxygen generated from reaction sites need to be removed from the cell in time. Excessive gas, especially large amount of gas bubbles in the microchannel and LGDL, can impede the liquid water transport and consequently lead to low cell performance and efficiency. In this study, a mathematical model for oxygen

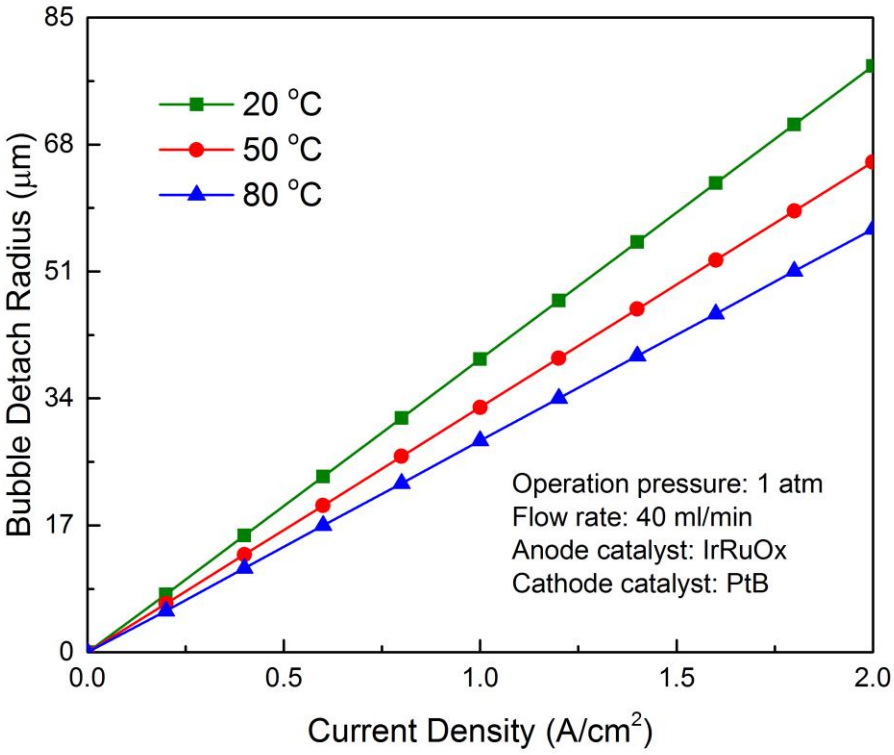


Figure 7.8. Effect of temperature on the oxygen bubble detachment.

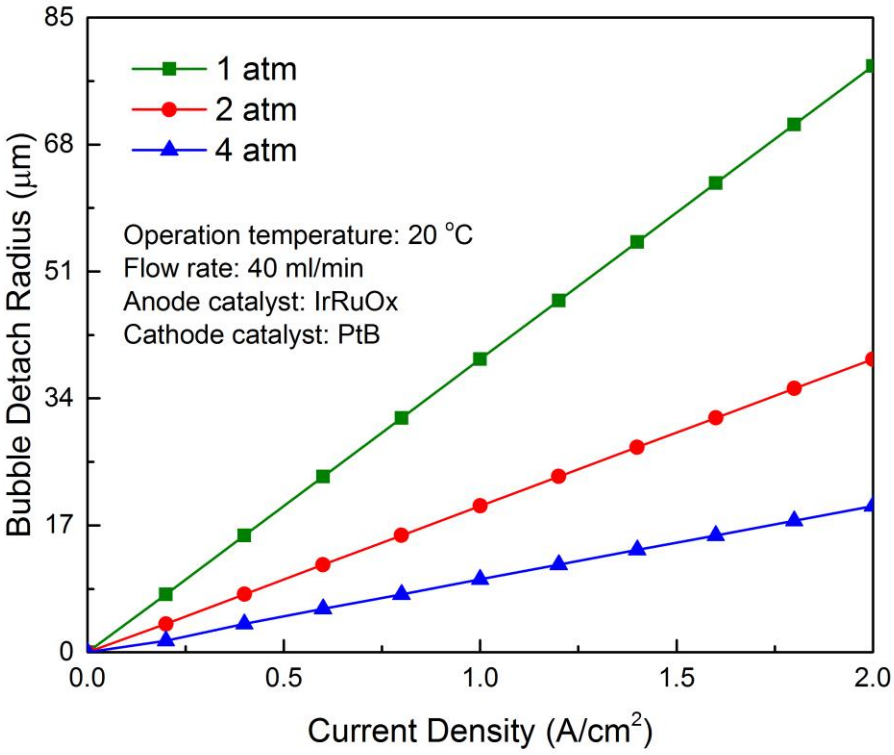


Figure 7.9. Effect of pressure on the oxygen bubble detachment.

bubble evaluation on the surface of anode LGDL in a PEMEC is developed. The model is carried out to investigate the effects of important parameters including current density, temperature, and pressure on the bubble growth and detachment. The results show that operating parameters have significant effects on the bubble dynamic behaviors.

The visualization results in chapter 6 perfectly present the bubble nucleation, growth, detachment and transport. The clips show bubbles nucleation near the edge of titanium thin/well tunable LGDL, which meet the requirements of triple-phase boundary for electrochemical reaction. In our experiments, the early stage of bubble growth is in a very short period. And the experimental results validate the modeling results.

As the operating temperature, and current density increase, the bubble radius will become larger at the same time step. While the bubble growth radius will get smaller with higher operating pressure. All forces acting on a single growing bubble in the liquid water are analyzed to calculate the bubble detachment diameters on the hydrophilic LGDL surface. Modeling results show that the bubble detachment diameter will increase as the current density increases and operating temperature, pressure.

Results obtained from the present model will provide fundamental understandings of oxygen bubble evolution and gas/liquid two-phase transport behaviors in a PEMEC and great insights into pore-scale multiphase transport mechanism, which will greatly help optimize the cell mass transport process and performance. Future work will be conducted on the modeling of bubble initial nucleation and evolution dynamics inside a CL coupled with the polarization curve of PEMECs.

CHAPTER 8

CONCLUSIONS AND SUGGESTIONS FOR FUTURE WORK

The performance of PEMEC is determined by activation overpotential, ohmic overpotential and concentration overpotential. The mechanism of triple phase boundary reactions inside an operating PEMECs have never been revealed before. This work discovered the true phenomena of electrochemical reaction and microfluidics behaviors inside microchannel of PEMEC *in-situ* for the first time by taking advantages of developing a titanium thin/well tunable LGDL, designing and fabricating a novel transparent PEMEC and setting up a long working distance high-speed and micro-scale visualization system.

To develop a LGDL with good performance and optical access through the LGDL, this work tried stainless steel woven mesh LGDL, additive fabricated titanium LGDL and titanium thin/well tunable LGLD. And found out that titanium thin/well tunable LGDL meet our requirements.

During the testing of stainless steel woven mesh LGLDL, the performance suddenly gets significantly drop. After characterization and compared the fresh LGDL and tested LGDL. We found out that there is serious corrosion inside anode of PEMEC. For a better understanding of the corrosion mechanisms and ion transitions in electrochemical devices, a stainless-steel mesh was purposely used as anode gas diffusion layer and was operated in a PEMEC with intentionally higher positive potentials under harsher oxidative environments. Large amount of iron is found to transport from anode to cathode, through the anode catalyst layer, the proton exchange membrane and the cathode catalyst layer. The formation of iron oxide and nickel oxide on single carbon fibers of a carbon paper gas

diffusion layer on the cathode side is observed by both scanning electron microscope and x-ray diffraction. A visual comparison between SEM images shows that high levels of oxidation occur in PEMECs at room temperature, especially at the anode side. The XRD pattern not only identifies the mechanism of oxidation on LGDLs, but also tracks the transportation pathways of corrosion from the anode to the cathode through the membrane along with SEM. The results indicate the corrosion elements of iron and nickel are transported from anode to cathode across through the catalyst-coated membrane, and deposited on carbon fibers. The test method and characterization have been demonstrated to be an effective approach to investigate corrosion mechanisms (transport and reformation) across MEAs in both quantitative and qualitative aspects. The addressed method could also open a new opportunity to fabricate multifunctional devices with single carbon fiber. In addition, this study has demonstrated a new accelerated test method, which can be easily for investigating the electrochemical corrosion and durability of various metallic materials. For additive manufacturing titanium LGDL, a novel low-cost technique of the electron beam melting (EBM) additive manufacturing for fabricating titanium liquid/gas diffusion media with high-corrosion resistance and well-tunable multifunctional parameters, including two-phase transport and improved electric/thermal conductivities, has been demonstrated for the first time. Their applications in proton exchange membrane electrolyzer cells have been explored. By taking advantage of the additive manufacturing, the EBM technology makes it possible to fabricate a three-dimensional and complicated object of virtually any shape from a digital model faster, cheaper, and easier than conventional methods, especially for titanium. In addition, compared with conventional woven LGDLs, increased performance and efficiency of up to 8% at room temperature

with EBM Ti-6Al-4V LGDLs is obtained due to their significant reduction of ohmic losses. More importantly, this process can enable manufacturing of LGDLs with control of pore size, pore shape, pore distribution, and therefore porosity and permeability, which will be valuable in developing sophisticated PEMEC models, which will in turn allow the optimization of the LGDL for maximum performance. Further, it will lead to a manufacturing solution to couple the LGDLs with other parts, since they can be easily integrated together with this advanced manufacturing process. Further optimal investigations and improvements of the EBM Ti-6Al-4V LGDLs and other components are underway.

Titanium thin and well-tunable liquid/gas diffusion layers (LGDLs) with flat interfacial surfaces are developed and are introduced into a PEMEC for the first time, and exhibit superior multifunctional performance over conventional LGDLs. Based on the electropotential performance tests, the operating voltages at a current density of 2.0 A/cm2 were as low as 1.69 V with an efficiency of up to 87.80%. In order to gain better understanding the mechanisms, both the ex-situ and in-situ characterizations were conducted and they showed the thin and well-tunable LGDL with flat surface features remarkably reduced its total resistances, and significantly promoted the PEMEC performance and efficiency by over 9%. It has also been shown that the total ohmic resistance plays a dominant role in the PEMFC performance, and a better efficiency can be obtained by reducing the LGDL thickness and further enhancing interfacial contacts between LGDLs with other components. In addition, the LGDL thickness reduction from 300 μm of conventional LGDLs to 25 μm will greatly decrease the weight and volume of PEMEC stacks, which can lead to new directions for future developments of low-cost

PEMECs with high performance. Its well-tunable features, including pore size, pore shape, pore distribution, and thus porosity and permeability, will be very valuable to develop PEMEC modeling and to validate simulations of PEMECs with optimal and repeatable performance.

After developed a desirable LGDL, we also designed and fabricated a transparent PEMEC and in-house assembled a long working distance high-speed, micro-scale visualization system. This set up help us able to optical access the surface of catalyst layer of PEMEC and capture rapid and micro-scale phenomena of electrochemical reaction and microfluidics behaviors.

The real situation of electrochemical reaction locations in operating PEMECs are revealed for the first time by developing a reaction-visible PEMEC, a thin-film with LGDL with known internal morphology, and high-speed and micro-scale visualization system. Surprisingly, reactions preferentially occur on the catalyst layer and LGDL interfaces, indicating most of the catalysts loaded on catalyst layers do not function and are thus wasted. A preliminary result from PEMEC with a novel fabricated catalyst layer has substantiate this visualization results and assumption. Further understanding this real situation in nano or crystallize scale will help to optimize catalyst layer and LGDL designs and fabrications, which will significantly reduce the cost of the PEMEC and speed up its wide commercialization as one of the most efficient way of producing hydrogen and energy storage.

In this study, besides the real phenomena of oxygen evolution reactions were revealed for the first time in a novel designed transparent PEMEC coupled with a high-speed and micro-scale visualization system (HMVS). From the captured photos and clips, the relationship

between oxygen evolution reaction sites and current density was revealed. The oxygen evolution reaction sites only along the rim of pore of titanium LGDL. With the increasing of the current density, the number of oxygen evolution reaction site also increased. This research captured different flow pattern of microfluidics in microchannel and inside the pore of LGDL under different operating parameters such as current density, temperature and pressure.

To maintain the cell performance and efficiency, oxygen and hydrogen generated from reaction sites need to be removed from the cell in time. Excessive gas, especially large amount of gas bubbles in the flow channel and LGDL, can impede the liquid water transport and consequently lead to low cell performance and efficiency. In this study, a mathematical model for oxygen bubble evaluation on the anode LGDL surface of a PEMFC is developed. Then the model is carried out to investigate the effects of important parameters including current density, temperature, pressure, flow velocity and contact angle on the bubble growth and detachment. The results show that operating parameters have significant effects on the bubble dynamic behaviors. Based on the results of mathematical model of bubble growth and detachment, as the operating temperature, and current density increase, the bubble radius will become larger at the same time step. While the bubble growth radius will get smaller with higher operating pressure. All forces acting on a single growing bubble in the liquid water are analyzed to calculate the bubble detachment diameters on the hydrophilic LGDL surface. Modeling results show that the bubble detachment diameter will increase as the current density increases and operating temperature, pressure.

The phenomena of triple-phase boundary reactions, behavior of two-phase flow, and dynamics of oxygen bubble evolution captured on catalyst layer inside the microchannel of an operating PEMEC can help to understand the behavior of electrochemical reactions and microfluidics in PEMECs, which can aid to optimize the design of cells, and consequently improve performance and efficiency of PEMECs. The future work will focus on the quantification investigation of oxygen bubble evolution and modeling of two-phase microfluidics in PEMECs. The effects of property of material, such as porosity and pore size of LGDLs, the land channel ratio, channel size, wettability of each layer; and behavior of microfluidics will be also investigated coupled with the performance and impedance. The modeling of bubble initial nucleation and evolution dynamics inside PEMECs will be studied. The results will provide fundamental understandings of gas/liquid two-phase transport behaviors in a PEMEC and great insights into pore-scale multiphase transport mechanism, which will greatly help optimize the cell mass transport process and performance.

REFERENCES

[1] W. Winsche, K. C. Hoffman, F. Salzano. Hydrogen: its future role in the nation's energy economy. *Science*. 1973;**180**:1325-32.

[2] T. N. Veziroglu, F. Barbir. Solar Hydrogen Energy System - the Choice of the Future. *Environmental Conservation*. 1991;**18**:304-12.

[3] J. A. Turner. Sustainable hydrogen production. *Science*. 2004;**305**:972-4.

[4] H. A. Gasteiger, N. M. Markovic. Just a Dream-or Future Reality? *Science*. 2009;**324**:48-9.

[5] B. Rausch, M. D. Symes, G. Chisholm, L. Cronin. Decoupled catalytic hydrogen evolution from a molecular metal oxide redox mediator in water splitting. *Science*. 2014;**345**:1326-30.

[6] M. M. Mench. Fuel cell engines: *John Wiley & Sons*; 2008.

[7] A. Marshall, B. Borresen, G. Hagen, M. Tsypkin, R. Tunold. Hydrogen production by advanced proton exchange membrane (PEM) water electrolysers - Reduced energy consumption by improved electrocatalysis. *Energy*. 2007;**32**:431-6.

[8] F. Barbir. PEM electrolysis for production of hydrogen from renewable energy sources. *Sol Energy*. 2005;**78**:661-9.

[9] M. M. Mench, F.-Y. Zhang. Fuel Cells. *Mechanical Engineers' Handbook IV:2:31:1–34*. 2015.

[10] M. I. Hoffert, K. Caldeira, G. Benford, D. R. Criswell, C. Green, H. Herzog, A. K. Jain, H. S. Kheshgi, K. S. Lackner, J. S. Lewis, H. D. Lightfoot, W. Manheimer, J. C. Mankins, M. E. Mauel, L. J. Perkins, M. E. Schlesinger, T. Volk, T. M. L. Wigley. Advanced technology paths to global climate stability: Energy for a greenhouse planet. *Science*. 2002;**298**:981-7.

[11] G. Chisholm, P. J. Kitson, N. D. Kirkaldy, L. G. Bloor, L. Cronin. 3D printed flow plates for the electrolysis of water: an economic and adaptable approach to device manufacture. *Energy & Environmental Science*. 2014;**7**:3026-32.

[12] S. D. Song, H. M. Zhang, X. P. Ma, Z. G. Shao, R. T. Baker, B. L. Yi. Electrochemical investigation of electrocatalysts for the oxygen evolution reaction in PEM water electrolyzers. *International Journal of Hydrogen Energy*. 2008;**33**:4955-61.

[13] M. Carmo, D. L. Fritz, J. Merge, D. Stolten. A comprehensive review on PEM water electrolysis. *International Journal of Hydrogen Energy*. 2013;**38**:4901-34.

[14] B. Han, S. M. Steen, J. Mo, F.-Y. Zhang. Electrochemical performance modeling of a proton exchange membrane electrolyzer cell for hydrogen energy. *International Journal of Hydrogen Energy*. 2015;**40**:7006-16.

[15] W. Kreuter, H. Hofmann. Electrolysis: the important energy transformer in a world of sustainable energy. *International Journal of Hydrogen Energy*. 1998;**23**:661-6.

[16] W. Xu, K. Scott, S. Basu. Performance of a high temperature polymer electrolyte membrane water electrolyser. *Journal of Power Sources*. 2011;**196**:8918-24.

[17] S.-Y. Lee, S. T. Wereley, L. Gui, W. Qu, I. Mudawar. Microchannel flow measurement using micro particle image velocimetry. in *ASME 2002 International Mechanical Engineering Congress and Exposition*. 2002. American Society of Mechanical Engineers.

[18] H. C. Zhang, G. X. Lin, J. C. Chen. Evaluation and calculation on the efficiency of a water electrolysis system for hydrogen production. *International Journal of Hydrogen Energy*. 2010;**35**:10851-8.

[19] S. Song, H. Zhang, X. Ma, Z. Shao, R. T. Baker, B. Yi. Electrochemical investigation of electrocatalysts for the oxygen evolution reaction in PEM water electrolyzers. *International Journal of Hydrogen Energy*. 2008;**33**:4955-61.

[20] L. R. Ma, S. Sui, Y. C. Zhai. Investigations on high performance proton exchange membrane water electrolyzer. *International Journal of Hydrogen Energy*. 2009;**34**:678-84.

[21] H. L. Wang, J. A. Turner. The influence of metal ions on the conductivity of Nafion 112 in polymer electrolyte membrane fuel cell. *Journal of Power Sources*. 2008;**183**:576-80.

[22] H. Wang, J. A. Turner. Reviewing Metallic PEMFC Bipolar Plates. *Fuel Cells*. 2010;**10**:510-9.

[23] M. P. Brady, H. Wang, J. A. Turner, H. M. Meyer, K. L. More, P. F. Tortorelli, B. D. McCarthy. Pre-oxidized and nitrided stainless steel alloy foil for proton exchange membrane fuel cell bipolar plates: Part 1. Corrosion, interfacial contact resistance, and surface structure. *Journal of Power Sources*. 2010;**195**:5610-8.

[24] C. Y. Du, P. F. Shi, X. Q. Cheng, G. P. Yin. Effective protonic and electronic conductivity of the catalyst layers in proton exchange membrane fuel cells. *Electrochemistry Communications*. 2004;**6**:435-40.

[25] W. Xu, K. Scott. The effects of ionomer content on PEM water electrolyser membrane electrode assembly performance. *International Journal of Hydrogen Energy*. 2010;**35**:12029-37.

[26] T. Ahmad, I. Hassan. Experimental analysis of microchannel entrance length characteristics using microparticle image velocimetry. *Journal of Fluids Engineering*. 2010;**132**:041102.

[27] S. D. Song, H. M. Zhang, X. P. Ma, Z. G. Shao, Y. N. Zhang, B. L. Yi. Bifunctional oxygen electrode with corrosion-resistive gas diffusion layer for unitized regenerative fuel cell. *Electrochemistry Communications*. 2006;**8**:399-405.

[28] H. Liu, B. L. Yi, M. Hou, J. F. Wu, Z. J. Hou, H. M. Zhang. Composite electrode for unitized regenerative proton exchange membrane fuel cell with improved cycle life. *Electrochemical and Solid State Letters*. 2004;**7**:A56-A9.

[29] K. E. Ayers, C. Capuano, E. B. Anderson. Recent advances in cell cost and efficiency for PEM-based water electrolysis. *ECS Transactions*. 2012;**41**:15-22.

[30] P. Millet, N. Mbemba, S. A. Grigoriev, V. N. Fateev, A. Aukauloo, C. Etievant. Electrochemical performances of PEM water electrolysis cells and perspectives. *International Journal of Hydrogen Energy*. 2011;**36**:4134-42.

[31] A. Biyikoglu. Review of proton exchange membrane fuel cell models. *International Journal of Hydrogen Energy*. 2005;**30**:1181-212.

[32] S. A. Grigoriev, V. I. Porembsky, V. N. Fateev. Pure hydrogen production by PEM electrolysis for hydrogen energy. *International Journal of Hydrogen Energy*. 2006;**31**:171-5.

[33] H. Wang, T. Deutsch, J. A. Turner. Direct water splitting under visible light with nanostructured hematite and WO3 photoanodes and a GaInP2 photocathode. *Journal of the Electrochemical Society*. 2008;**155**:F91-F6.

[34] J. Fall, D. Humphreys, S. M. Guo. Design and Testing of a Unitized Regenerative Fuel Cell. *J Fuel Cell Sci Tech*. 2009;**6**.

[35] A. Strand, H. Weydahl. Regenerative Fuel Cell Systems for Satellites. in *8th European Space Power Conference*. 2008.

[36] D. Shapiro, J. Duffy, M. Kimble, M. Pien. Solar-powered regenerative PEM electrolyzer/fuel cell system. *Solar Energy*. 2005;**79**:544-50.

[37] N. Muradov. Emission-free fuel reformers for mobile and portable fuel cell applications. *Journal of power Sources*. 2003;**118**:320-4.

[38] T. J. Toops, M. P. Brady, F.-Y. Zhang, H. M. Meyer, K. Ayers, A. Roemer, L. Dalton. Evaluation of Nitrided Titanium separator plates for proton exchange membrane electrolyzer cells. *Journal of Power Sources*. 2014:954-60.

[39] S. M. Steen, F.-Y. Zhang. In-situ and Ex-situ Characterizations of Electrode Interfaces in Energy Storage Electrolyzers. *ECS Transactions*. 2014;**59**:95-102.

[40] W. Partridge, T. J. Toops, J. Green, T. R. Armstrong. Intra-fuel cell stack measurements of transient concentration distributions. *Journal of Power Sources*. 2006;**160**:454-61.

[41] S. J. Peighambardoust, S. Rowshanzamir, M. Amjadi. Review of the proton exchange membranes for fuel cell applications. *International Journal of Hydrogen Energy*. 2010;**35**:9349-84.

[42] F.-Y. Zhang, S. G. Advani, A. K. Prasad. Performance of a metallic gas diffusion layer for PEM fuel cells. *Journal of Power Sources*. 2008;**176**:293-8.

[43] T. Matsuura, M. Kato, M. Hori. Study on metallic bipolar plate for proton exchange membrane fuel cell. *Journal of Power Sources*. 2006;**161**:74-8.

[44] S. Arisetty, A. K. Prasad, S. G. Advani. Metal foams as flow field and gas diffusion layer in direct methanol fuel cells. *Journal of Power Sources*. 2007;**165**:49-57.

[45] H. Tawfik, Y. Hung, D. Mahajan. Metal bipolar plates for PEM fuel cell—a review. *Journal of Power Sources*. 2007;**163**:755-67.

[46] F.-Y. Zhang, A. K. Prasad, S. G. Advani. Investigation of a copper etching technique to fabricate metallic gas diffusion media. *Journal of Micromechanics and Microengineering*. 2006;**16**:N23.

[47] S. Joseph, J. C. McClure, R. Chianelli, P. Pich, P. J. Sebastian. Conducting polymer-coated stainless steel bipolar plates for proton exchange membrane fuel cells (PEMFC). *International Journal of Hydrogen Energy*. 2005;**30**:1339-44.

[48] A. Kumar, M. Ricketts, S. Hirano. Ex situ evaluation of nanometer range gold coating on stainless steel substrate for automotive polymer electrolyte membrane fuel cell bipolar plate. *Journal of Power Sources*. 2010;**195**:1401-7.

[49] F.-Y. Zhang, S. G. Advani, A. K. Prasad. Advanced High Resolution Characterization Techniques for Degradation Studies in Fuel Cells. *Polymer Electrolyte Fuel Cell Degradation*. 2011:365.

[50] F. Y. Zhang, S. G. Advani, A. K. Prasad, T. P. Beebe, Z. S. Khalifa, S. I. Shah. Investigation of freeze/thaw effects on catalyst layer degradation in fuel cells with XPS and XRD. *Fuel Cell Seminar*. 2009.

[51] J. Mo, S. M. Steen III, F.-Y. Zhang. X-Ray Diffraction Studies on Material Corrosions in Renewable Energy Storage Electrolyzers. in *Journal of Physics: Conference Series*. 2014. IOP Publishing.

[52] W. Fredriksson, S. Malmgren, T. Gustafsson, M. Gorgoi, K. Edström. Full depth profile of passive films on 316L stainless steel based on high resolution HAXPES in combination with ARXPS. *Applied Surface Science*. 2012;**258**:5790-7.

[53] X. Gao, X. Wu, Z. Zhang, H. Guan, E.-h. Han. Characterization of oxide films grown on 316L stainless steel exposed to H 2 O 2-containing supercritical water. *The Journal of supercritical fluids*. 2007;**42**:157-63.

[54] J. Zhang, N. Li, Y. Chen, A. Rusanov. Corrosion behaviors of US steels in flowing lead–bismuth eutectic (LBE). *Journal of Nuclear Materials*. 2005;**336**:1-10.

[55] M. Son, N. Akao, N. Hara, K. Sugimoto. Electrochemical and Corrosion Properties of Fe2O3Cr2O3MoO2 Artificial Passivation Films in HCl Solutions. *Journal of The Electrochemical Society*. 2001;**148**:B43-B50.

[56] K. Sugimoto, M. Son, Y. Ohya, N. Akao, N. Hara. Corrosion Science–A Retrospective and Current Status in Honor of Robert P. *Frankenthal, Electrochemical Society Proceedings*.**2002**:13.

[57] X. Luo, R. Tang, C. S. Long, Z. Miao, Q. Peng, C. Li. Corrosion behavior of austenitic and ferritic steels in supercritical water. *Nucl Eng Technol*. 2008;**40**:147-54.

[58] N. Solomon, I. Solomon. Deformation induced martensite in AISI 316 stainless steel. *Rev Metal Madrid*. 2010;**46**:121-8.

[59] Z. Q. Li, C. J. Lu, Z. P. Xia, Y. Zhou, Z. Luo. X-ray diffraction patterns of graphite and turbostratic carbon. *Carbon*. 2007;**45**:1686-95.

[60] H. T. Cui, Y. Liu, W. Z. Ren. Structure switch between alpha-Fe2O3, gamma-Fe2O3 and Fe3O4 during the large scale and low temperature sol-gel synthesis of

nearly monodispersed iron oxide nanoparticles. *Adv Powder Technol*. 2013;**24**:93-7.

[61] J. Vanhanen, P. Lund, J. Tolonen. Electrolyser-metal hydride-fuel cell system for seasonal energy storage. *International journal of hydrogen energy*. 1998;**23**:267-71.

[62] J. Turner, G. Sverdrup, M. K. Mann, P. C. Maness, B. Kroposki, M. Ghirardi, R. J. Evans, D. Blake. Renewable hydrogen production. *International Journal of Energy Research*. 2008;**32**:379-407.

[63] K. E. Ayers, E. B. Anderson, C. Capuano, B. Carter, L. Dalton, G. Hanlon, J. Manco, M. Niedzwiecki. Research advances towards low cost, high efficiency PEM electrolysis. *ECS Transactions*. 2010;**33**:3-15.

[64] M. K. Debe, S. M. Hendricks, G. D. Vernstrom, M. Meyers, M. Brostrom, M. Stephens, Q. Chan, J. Willey, M. Hamden, C. K. Mittelsteadt, C. B. Capuano, K. E. Ayers, E. B. Anderson. Initial Performance and Durability of Ultra-Low Loaded NSTF Electrodes for PEM Electrolyzers. *Journal of the Electrochemical Society*. 2012;**159**:K165-K76.

[65] T. J. Toops, M. P. Brady, F. Y. Zhang, H. M. Meyer, K. Ayers, A. Roemer, L. Dalton. Evaluation of nitrided titanium separator plates for proton exchange membrane electrolyzer cells. *Journal of Power Sources*. 2014;**272**:954-60.

[66] E. Zoulias, E. Varkaraki, N. Lymberopoulos, C. N. Christodoulou, G. N. Karagiorgis. A review on water electrolysis. *TCJST*. 2004;**4**:41-71.

[67] J. H. Russell, L. J. Nuttal, A. P. Fickett. Hydrogen Generation by Solid Polymer Electrolyte Water Electrolysis. *Abstracts of Papers of the American Chemical Society*. 1973:2-.

[68] I. Zenyuk, E. Kumbur, S. Litster. Deterministic contact mechanics model applied to electrode interfaces in polymer electrolyte fuel cells and interfacial water accumulation. *Journal of Power Sources*. 2013;**241**:379-87.

[69] T. Swamy, E. Kumbur, M. Mench. Characterization of interfacial structure in PEFCs: water storage and contact resistance model. *Journal of the Electrochemical Society*. 2010;**157**:B77-B85.

[70] A. Kalidindi, R. Taspinar, S. Litster, E. Kumbur. A two-phase model for studying the role of microporous layer and catalyst layer interface on polymer electrolyte fuel cell performance. *International Journal of Hydrogen Energy*. 2013;**38**:9297-309.

[71] J. Mo, S. M. Steen III, B. Han, F.-Y. Zhang. High-speed and micro-scale measurements of flow and reaction dynamics for sustainable energy storage. in *13th International Energy Conversion Engineering Conference*. 2015. AIAA 2015-3913.

[72] N. Briguglio, G. Brunaccini, S. Siracusano, N. Randazzo, G. Dispenza, M. Ferraro, R. Ornelas, A. Arico, V. Antonucci. Design and testing of a compact PEM electrolyzer system. *International Journal of Hydrogen Energy*. 2013;**38**:11519-29.

[73] H. Y. Jung, S. Y. Huang, B. N. Popov. High-durability titanium bipolar plate modified by electrochemical deposition of platinum for unitized regenerative fuel cell (URFC). *Journal of Power Sources*. 2010;**195**:1950-6.

[74] J. Fall, D. Humphreys, S. M. Guo. Design and Testing of a Unitized Regenerative Fuel Cell. *J Fuel Cell Sci Tech*. 2009;**6**:031003.

[75] G. Y. Chen, C. C. Waraksa, H. G. Cho, D. D. Macdonald, T. E. Mallouk. EIS studies of porous oxygen electrodes with discrete particles - I. Impedance of oxide catalyst supports. *Journal of the Electrochemical Society*. 2003;**150**:E423-E8.

[76] J. O. Bockris. Hydrogen. *Materials*. 2011;**4**:2073-91.

[77] A. V. Nikiforov, I. M. Petrushina, E. Christensen, A. L. Tomas-Garcia, N. J. Bjerrum. Corrosion behaviour of construction materials for high temperature steam electrolysers. *International Journal of Hydrogen Energy*. 2011;**36**:111-9.

[78] R. E. Fuentes, J. Farell, J. W. Weidner. Multimetallic Electrocatalysts of Pt, Ru, and Ir Supported on Anatase and Rutile TiO2 for Oxygen Evolution in an Acid Environment. *Electrochemical and Solid State Letters*. 2011;**14**:E5-E7.

[79] S. S. Dihrab, K. Sopian, M. A. Alghoul, M. Y. Sulaiman. Review of the membrane and bipolar plates materials for conventional and unitized regenerative fuel cells. *Renewable & Sustainable Energy Reviews*. 2009;**13**:1663-8.

[80] J. Mo, S. M. Steen, F.-Y. Zhang, T. J. Toops, M. P. Brady, J. B. Green. Electrochemical investigation of stainless steel corrosion in a proton exchange membrane electrolyzer cell. *International Journal of Hydrogen Energy*. 2015;**40**:12506-11.

[81] J. Cho, J. Park, H. Oh, K. Min, E. Lee, J.-Y. Jyoung. Analysis of the transient response and durability characteristics of a proton exchange membrane fuel cell with different micro-porous layer penetration thicknesses. *Applied energy*. 2013;**111**:300-9.

[82] J. Mo, S. M. Steen, S. Retterer, D. A. Cullen, A. Terekhov, F.-Y. Zhang. Mask-Patterned Wet Etching of Thin Titanium Liquid/Gas Diffusion Layers for a PEMEC. *ECS Transactions*. 2015;**66**:3-10.

[83] P. C. Joshi, R. R. Dehoff, C. E. Duty, W. H. Peter, R. D. Ott, L. J. Love, C. A. Blue. Direct digital additive manufacturing technologies: Path towards hybrid integration. in *Future of Instrumentation International Workshop (FIIW), 2012*. 2012. IEEE.

[84] W. J. Sames, K. A. Unocic, R. R. Dehoff, T. Lolla, S. S. Babu. Thermal effects on microstructural heterogeneity of Inconel 718 materials fabricated by electron beam melting. *Journal of Materials Research*. 2014;**29**:1920-30.

[85] R. B. Dinwiddie, R. R. Dehoff, P. D. Lloyd, L. E. Lowe, J. B. Ulrich. Thermographic in-situ process monitoring of the electron-beam melting technology used in additive manufacturing. in *SPIE Defense, Security, and Sensing*. 2013. International Society for Optics and Photonics.

[86] O. Cansizoglu, O. Harrysson, D. Cormier, H. West, T. Mahale. Properties of Ti–6Al–4V non-stochastic lattice structures fabricated via electron beam melting. *Materials Science and Engineering: A*. 2008;**492**:468-74.

[87] S. Gaytan, L. Murr, F. Medina, E. Martinez, M. Lopez, R. Wicker. Advanced metal powder based manufacturing of complex components by electron beam melting. *Materials Science and Technology*. 2009;**24**:180-90.

[88] D. Ramirez, L. Murr, S. Li, Y. Tian, E. Martinez, J. Martinez, B. Machado, S. Gaytan, F. Medina, R. Wicker. Open-cellular copper structures fabricated by additive manufacturing using electron beam melting. *Materials Science and Engineering: A*. 2011;**528**:5379-86.

[89] F. List, R. R. Dehoff, L. E. Lowe, W. J. Sames. Properties of Inconel 625 mesh structures grown by electron beam additive manufacturing. *Materials Science and Engineering: A*. 2014;**615**:191-7.

[90] L. Murr, S. Quinones, S. Gaytan, M. Lopez, A. Rodela, E. Martinez, D. Hernandez, E. Martinez, F. Medina, R. Wicker. Microstructure and mechanical behavior of Ti–6Al–4V produced by rapid-layer manufacturing, for biomedical applications. *Journal of the Mechanical Behavior of Biomedical Materials*. 2009;**2**:20-32.

[91] X. Gong, T. Anderson, K. Chou. Review on powder-based electron beam additive manufacturing technology. in *ASME/ISCIE 2012 International Symposium on Flexible Automation*. 2012. American Society of Mechanical Engineers.

[92] A. Safdar, L.-Y. Wei, A. Snis, Z. Lai. Evaluation of microstructural development in electron beam melted Ti-6Al-4V. *Materials Characterization*. 2012;**65**:8-15.

[93] L. E. Murr, S. Gaytan, A. Ceylan, E. Martinez, J. Martinez, D. Hernandez, B. Machado, D. Ramirez, F. Medina, S. Collins. Characterization of titanium aluminide alloy components fabricated by additive manufacturing using electron beam melting. *Acta Materialia*. 2010;**58**:1887-94.

[94] V. Juechter, T. Scharowsky, R. Singer, C. Körner. Processing window and evaporation phenomena for Ti–6Al–4V produced by selective electron beam melting. *Acta Materialia*. 2014;**76**:252-8.

[95] N. P. Kulkarni. Design and development of manufacturing methods for manufacturing of PEM fuel cell MEA's. 2011.

[96] H. Y. Zheng, H. Ito, T. H. Okabe. Production of titanium powder by the calciothermic reduction of titanium concentrates or ore using the preform reduction process. *Materials Transactions*. 2007;**48**:2244-51.

[97] L. Zeng, T. S. Zhao. Integrated inorganic membrane electrode assembly with layered double hydroxides as ionic conductors for anion exchange membrane water electrolysis. *Nano Energy*. 2015;**11**:110-8.

[98] X. L. Fan, X. Z. Xiao, J. Shao, L. T. Zhang, S. Q. Li, H. W. Ge, Q. D. Wang, L. X. Chen. Size effect on hydrogen storage properties of NaAlH4 confined in uniform porous carbons. *Nano Energy*. 2013;**2**:995-1003.

[99] K. E. Ayers, L. T. Dalton, E. B. Anderson. (Invited) Efficient Generation of High Energy Density Fuel from Water. *ECS Transactions*. 2012;**41**:27-38.

[100] D. Pukazhselvan, V. Kumar, S. K. Singh. High capacity hydrogen storage: Basic aspects, new developments and milestones. *Nano Energy*. 2012;**1**:566-89.

[101] S. L. Candelaria, Y. Y. Shao, W. Zhou, X. L. Li, J. Xiao, J. G. Zhang, Y. Wang, J. Liu, J. H. Li, G. Z. Cao. Nanostructured carbon for energy storage and conversion. *Nano Energy*. 2012;**1**:195-220.

[102] S. A. Grigoriev, P. Millet, S. A. Volobuev, V. N. Fateev. Optimization of porous current collectors for PEM water electrolysers. *International Journal of Hydrogen Energy*. 2009;**34**:4968-73.

[103] H. Yang, L. Guo, W. Yan, H. Liu. A novel composite photocatalyst for water splitting hydrogen production. *Journal of Power Sources*. 2006;**159**:1305-9.

[104] K. Gong, F. Du, Z. Xia, M. Durstock, L. Dai. Nitrogen-doped carbon nanotube arrays with high electrocatalytic activity for oxygen reduction. *science*. 2009;**323**:760-4.

[105] J. Mo, R. R. Dehoff, W. H. Peter, T. J. Toops, J. B. Green, F.-Y. Zhang. Additive manufacturing of liquid/gas diffusion layers for low-cost and high-efficiency hydrogen production. *International Journal of Hydrogen Energy*. 2016;**41**:3128-35.

[106] P. M. Wilde, M. Maendle, M. Murata, N. Berg. Structural and physical properties of GDL and GDL/BPP combinations and their influence on PEMFC performance. *Fuel Cells*. 2004;**4**:180-4.

[107] K. Eom, E. Cho, J. Jang, H.-J. Kim, T.-H. Lim, B. K. Hong, J. H. Lee. Optimization of GDLs for high-performance PEMFC employing stainless steel bipolar plates. *International Journal of Hydrogen Energy*. 2013;**38**:6249-60.

[108] M. Prasanna, H. Ha, E. Cho, S.-A. Hong, I.-H. Oh. Influence of cathode gas diffusion media on the performance of the PEMFCs. *Journal of Power Sources*. 2004;**131**:147-54.

[109] F. Y. Zhang, A. K. Prasad, S. G. Advani. Investigation of a copper etching technique to fabricate metallic gas diffusion media. *Journal of Micromechanics and Microengineering*. 2006;**16**:N23-N7.

[110] F. Y. Zhang, S. G. Advani, A. K. Prasad. Performance of a metallic gas diffusion layer for PEM fuel cells. *Journal of Power Sources*. 2008;**176**:293-8.

[111] F. Y. Zhang, X. G. Yang, C. Y. Wang. Liquid water removal from a polymer electrolyte fuel cell. *Journal of the Electrochemical Society*. 2006;**153**:A225-A32.

[112] Y. Wang, K. S. Chen, J. Mishler, S. C. Cho, X. C. Adroher. A review of polymer electrolyte membrane fuel cells: technology, applications, and needs on fundamental research. *Applied Energy*. 2011;**88**:981-1007.

[113] E. Kumbur, K. Sharp, M. Mench. On the effectiveness of Leverett approach for describing the water transport in fuel cell diffusion media. *Journal of Power Sources*. 2007;**168**:356-68.

[114] A. Higier, H. Liu. Optimization of PEM fuel cell flow field via local current density measurement. *International Journal of Hydrogen Energy*. 2010;**35**:2144-50.

[115] T. Zhou, H. Liu. Effects of the electrical resistances of the GDL in a PEM fuel cell. *Journal of Power Sources*. 2006;**161**:444-53.

[116] W. K. Epting, J. Gelb, S. Litster. Resolving the Three-Dimensional Microstructure of Polymer Electrolyte Fuel Cell Electrodes using Nanometer-Scale X-ray Computed Tomography. *Advanced Functional Materials*. 2012;**22**:555-60.

[117] S. Park, J.-W. Lee, B. N. Popov. A review of gas diffusion layer in PEM fuel cells: materials and designs. *International Journal of Hydrogen Energy*. 2012;**37**:5850-65.

[118] E. B. Anderson. Latest Advancements in PEM Electrolysis. *Technical Forum of Hydrogen-Fuel Cells-Batteries, International Association of Hydrogen Energy*. 2014.

[119] J. Xu, G. Liu, J. Li, X. Wang. The electrocatalytic properties of an IrO 2/SnO 2 catalyst using SnO 2 as a support and an assisting reagent for the oxygen evolution reaction. *Electrochimica acta*. 2012;**59**:105-12.

[120] C. M. Hwang, M. Ishida, H. Ito, T. Maeda, A. Nakano, Y. Hasegawa, N. Yokoi, A. Kato, T. Yoshida. Influence of properties of gas diffusion layers on the performance of polymer electrolyte-based unitized reversible fuel cells. *International Journal of Hydrogen Energy*. 2011;**36**:1740-53.

[121] B. Han, J. Mo, Z. Kang, F.-Y. Zhang. Effects of membrane electrode assembly properties on two-phase transport and performance in proton exchange membrane electrolyzer cells. *Electrochimica Acta*. 2016;**188**:317-26.

[122] R. O'Hayre, F. B. Prinz. The air/platinum/Nafion triple-phase boundary: characteristics, scaling, and implications for fuel cells. *Journal of The Electrochemical Society*. 2004;**151**:A756-A62.

[123] W. Zhu, S. Deevi. A review on the status of anode materials for solid oxide fuel cells. *Materials Science and Engineering: A*. 2003;**362**:228-39.

[124] R. P. Iczkowski, M. B. Cutlip. Voltage losses in fuel cell cathodes. *Journal of The Electrochemical Society*. 1980;**127**:1433-40.

[125] B. Steele. Material science and engineering: the enabling technology for the commercialisation of fuel cell systems. *Journal of Materials Science*. 2001;**36**:1053-68.

[126] Z. Kang, J. Mo, G. Yang, S. T. Retterer, D. A. Cullen, T. J. Toops, J. B. Green Jr, M. M. Mench, F.-Y. Zhang. Investigation of thin/well-tunable liquid/gas diffusion layers exhibiting superior multifunctional performance in low-temperature electrolytic water splitting. *Energy & Environmental Science*. 2016;**11**.

[127] A. Le Goff, V. Artero, B. Jousselme, P. D. Tran, N. Guillet, R. Métayé, A. Fihri, S. Palacin, M. Fontecave. From hydrogenases to noble metal–free catalytic nanomaterials for H2 production and uptake. *Science*. 2009;**326**:1384-7.

[128] A. Stoyanova, G. Borisov, E. Lefterova, E. Slavcheva. Oxygen evolution on Ebonex-supported Pt-based binary compounds in PEM water electrolysis. *International Journal of Hydrogen Energy*. 2012;**37**:16515-21.

[129] R. Tunold, A. Marshall, E. Rastenc, M. Tsypkin, L.-E. Owe, S. Sunde. Materials for Electrocatalysis of Oxygen Evolution Process in PEM Water Electrolysis Cells. *ECS Transactions*. 2010;**25**:103 - 17.

[130] F. Y. Zhang, D. Spernjak, A. K. Prasad, S. G. Advani. In situ characterization of the catalyst layer in a polymer electrolyte membrane fuel cell. *Journal of the Electrochemical Society*. 2007;**154**:B1152-B7.

[131] X. G. Yang, F. Y. Zhang, A. L. Lubawy, C. Y. Wang. Visualization of liquid water transport in a PEFC. *Electrochemical and Solid State Letters*. 2004;**7**:A408-A11.

[132] S. Grigoriev, V. Porembsky, V. Fateev. Pure hydrogen production by PEM electrolysis for hydrogen energy. *International Journal of Hydrogen Energy*. 2006;**31**:171-5.

[133] N. Samsonov, L. Bobe, L. Gavrilov, V. Korolev, V. Novikov, N. Farafonov, V. Soloukhin, S. J. Romanov, P. Andrejchuk, N. Protasov. Water recovery and oxygen generation by electrolysis aboard the International Space Station. SAE Technical Paper; 2002.

[134] O. F. Selamet, U. Pasaogullari, D. Spernjak, D. S. Hussey, D. L. Jacobson, M. D. Mat. Two-phase flow in a proton exchange membrane electrolyzer visualized in

situ by simultaneous neutron radiography and optical imaging. *International Journal of Hydrogen Energy*. 2013;**38**:5823-35.

[135] E. Brightman, J. Dodwell, N. van Dijk, G. Hinds. In situ characterisation of PEM water electrolysers using a novel reference electrode. *Electrochemistry Communications*. 2015;**52**:1-4.

[136] M. A. Hoeh, T. Arlt, I. Manke, J. Banhart, D. L. Fritz, W. Maier, W. Lehnert. In operando synchrotron X-ray radiography studies of polymer electrolyte membrane water electrolyzers. *Electrochemistry Communications*. 2015;**55**:55-9.

[137] J. Mo, Z. Kang, S. T. Retterer, D. A. Cullen, T. J. Toops, J. B. G. Jr., M. M. Mench, F.-Y. Zhang. Discovery of true electrochemical reactions for ultrahigh catalyst mass activity in water splitting. *Science Advances*. 2016;**2**:e1600690.

[138] W. L. Qu, S. M. Yoon, I. Mudawar. Two-phase flow and heat transfer in rectangular micro-channels. *J Electron Packaging*. 2004;**126**:288-300.

[139] J. Mo, S. M. Steen III, B. Han, Z. Kang, A. Terekhov, F.-Y. Zhang, S. T. Retterer, D. A. Cullen. Investigation of titanium felt transport parameters for energy storage and hydrogen/oxygen production. in *13th International Energy Conversion Engineering Conference*. 2015. AIAA 2015-3914.

[140] J. Mo, Z. Kang, G. Yang, S. T. Retterer, D. A. Cullen, T. J. Toops, J. B. G. Jr., F.-Y. Zhang. Thin liquid/gas diffusion layers for high-effieciency hydrogen production from water splitting. *Applied Energy*. 2016;**177**:817-22.

[141] M. Carmo, D. L. Fritz, J. Mergel, D. Stolten. A comprehensive review on PEM water electrolysis. *International Journal of Hydrogen Energy*. 2013;**38**:4901-34.

[142] F. Marangio, M. Santarelli, M. Cali. Theoretical model and experimental analysis of a high pressure PEM water electrolyser for hydrogen production. *International Journal of Hydrogen Energy*. 2009;**34**:1143-58.

[143] P. Millet, N. Mbemba, S. Grigoriev, V. Fateev, A. Aukauloo, C. Etiévant. Electrochemical performances of PEM water electrolysis cells and perspectives. *International Journal of Hydrogen Energy*. 2011;**36**:4134-42.

[144] X. Cheng, Z. Shi, N. Glass, L. Zhang, J. Zhang, D. Song, Z.-S. Liu, H. Wang, J. Shen. A review of PEM hydrogen fuel cell contamination: Impacts, mechanisms, and mitigation. *Journal of Power Sources*. 2007;**165**:739-56.

[145] D. Bessarabov, H. Wang, H. Li, N. Zhao. PEM Electrolysis for Hydrogen Production: Principles and Applications: *Taylor & Francis*; 2015.

[146] B. Han, S. Steen, J. Mo, F.-Y. Zhang. Modeling of interfacial resistance effects on the performance and efficiency for electrolyzer energy storage. in *13th International Energy Conversion Engineering Conference*. 2015. AIAA 2015-3915.

[147] L. An, T. Zhao, Z. Chai, P. Tan, L. Zeng. Mathematical modeling of an anion-exchange membrane water electrolyzer for hydrogen production. *International Journal of Hydrogen Energy*. 2014;**39**:19869-76.

[148] A. Arvay, J. French, J. C. Wang, X. H. Peng, A. M. Kannan. Nature inspired flow field designs for proton exchange membrane fuel cell. *International Journal of Hydrogen Energy*. 2013;**38**:3717-26.

[149] T. Berning, D. M. Lu, N. Djilali. Three-dimensional computational analysis of transport phenomena in a PEM fuel cell. *Journal of power sources*. 2002;**106**:284-94.

[150] S. Lubetkin. The fundamentals of bubble evolution. *Chemical Society Reviews*. 1995;**24**:243-50.

[151] R. Wüthrich, C. Comninellis, H. Bleuler. Bubble evolution on vertical electrodes under extreme current densities. *Electrochimica Acta*. 2005;**50**:5242-6.

[152] A. Bozorgnezhad, M. Shams, H. Kanani, M. Hasheminasab, G. Ahmadi. Two-phase flow and droplet behavior in microchannels of PEM fuel cell. *International Journal of Hydrogen Energy*. 2016;**41**:19164-81.

[153] S. Lubetkin. The motion of electrolytic gas bubbles near electrodes. *Electrochimica acta*. 2002;**48**:357-75.

[154] W. Fritz. Maximum volume of vapor bubbles. *Phys Z*. 1935;**36**:379-84.

[155] B. E. Staniszewski. Nucleate boiling bubble growth and departure. Cambridge, Mass.: Massachusetts Institute of Technology, Division of Industrial Cooperation,[1959]; 1959.

[156] Y. Chen, M. Groll. Dynamics and shape of bubbles on heating surfaces: A simulation study. *International Journal of Heat and Mass Transfer*. 2006;**49**:1115-28.

[157] J. Klausner, R. Mei, D. Bernhard, L. Zeng. Vapor bubble departure in forced convection boiling. *International journal of heat and mass transfer*. 1993;**36**:651-62.

[158] D. Chen, L.-m. Pan, S. Ren. Prediction of bubble detachment diameter in flow boiling based on force analysis. *Nuclear Engineering and Design*. 2012;**243**:263-71.

[159] S. Grigoriev, P. Millet, S. Volobuev, V. Fateev. Optimization of porous current collectors for PEM water electrolysers. *International Journal of Hydrogen Energy*. 2009;**34**:4968-73.

[160] S. Grigoriev, A. Kalinnikov, P. Millet, V. Porembsky, V. Fateev. Mathematical modeling of high-pressure PEM water electrolysis. *Journal of applied electrochemistry*. 2010;**40**:921-32.

[161] A. Awasthi, K. Scott, S. Basu. Dynamic modeling and simulation of a proton exchange membrane electrolyzer for hydrogen production. *International journal of hydrogen energy*. 2011;**36**:14779-86.

[162] M. Debe, S. Hendricks, G. Vernstrom, M. Meyers, M. Brostrom, M. Stephens, Q. Chan, J. Willey, M. Hamden, C. K. Mittelsteadt. Initial performance and durability of ultra-low loaded NSTF electrodes for PEM electrolyzers. *Journal of the Electrochemical Society*. 2012;**159**:K165-K76.

[163] Z. Abdin, C. Webb, E. M. Gray. Modelling and simulation of a proton exchange membrane (PEM) electrolyser cell. *International Journal of Hydrogen Energy*. 2015;**40**:13243-57.

[164] S. K. Panda, M. Annamalai. Experimental study on bubble absorber with multiple tangential nozzles. 2014.

[165] H. Bai, B. G. Thomas. Bubble formation during horizontal gas injection into downward-flowing liquid. *Metallurgical and materials transactions B*. 2001;**32**:1143-59.

[166] G. Sakuma, Y. Fukunaka, H. Matsushima. Nucleation and growth of electrolytic gas bubbles under microgravity. *International Journal of Hydrogen Energy*. 2014;**39**:7638-45.

[167] H. Matsushima, D. Kiuchi, Y. Fukunaka, K. Kuribayashi. Single bubble growth during water electrolysis under microgravity. *Electrochemistry Communications*. 2009;**11**:1721-3.

[168] P. Chandran, S. Bakshi, D. Chatterjee. Study on the characteristics of hydrogen bubble formation and its transport during electrolysis of water. *Chemical Engineering Science*. 2015;**138**:99-109.

[169] H. Liu, L.-m. Pan, H. Huang, Q. Qin, P. Li, J. Wen. Hydrogen bubble growth at micro-electrode under magnetic field. *Journal of Electroanalytical Chemistry*. 2015;**754**:22-9.

[170] X. Yang, F. Karnbach, M. Uhlemann, S. Odenbach, K. Eckert. Dynamics of single hydrogen bubbles at a platinum microelectrode. *Langmuir*. 2015;**31**:8184-93.

[171] D. Fernández, P. Maurer, M. Martine, J. Coey, M. E. Möbius. Bubble formation at a gas-evolving microelectrode. *Langmuir*. 2014;**30**:13065-74.

[172] H. Matsushima, T. Iida, Y. Fukunaka. Gas bubble evolution on transparent electrode during water electrolysis in a magnetic field. *Electrochimica Acta*. 2013;**100**:261-4.

[173] H. Matsushima, Y. Fukunaka, K. Kuribayashi. Water electrolysis under microgravity: Part II. Description of gas bubble evolution phenomena. *Electrochimica acta*. 2006;**51**:4190-8.

[174] C. Sillen, E. Barendrecht, L. Janssen, S. Van Stralen. Gas bubble behaviour during water electrolysis. *International Journal of Hydrogen Energy*. 1982;**7**:577-87.

[175] R. de Jonge, E. Barendrecht, L. Janssen, S. van Stralen. Gas bubble behaviour and electrolyte resistance during water electrolysis. *International Journal of Hydrogen Energy*. 1982;**7**:883-94.

[176] R. R. Unocic, X. G. Sun, R. L. Sacci, L. A. Adamczyk, D. H. Alsem, S. Dai, N. J. Dudney, K. L. More. Direct Visualization of Solid Electrolyte Interphase Formation in Lithium-Ion Batteries with In Situ Electrochemical Transmission Electron Microscopy. *Microsc Microanal*. 2014;**20**:1029-37.

[177] S. Escobar Vargas, J. Gonzalez, D. Fabris, R. Sharma, C. Bash, O. Ruiz. Microbubble efficiency during fast boiling growth. *TECNOLOGÍA Y DESARROLLO*. 2007;**2**:139-44.

[178] V. P. Carey. Liquid–vapor Phase Change Phenomena–An Introduction to the Thermodynamics of Vaporization and Condensation Processes in Heat Transfer Equipment. *Taylor and Francis, Bristol, PA*; 1992. p. 158-63.

[179] G. Thorncroft, J. F. Klausner. Bubble forces and detachment models. *Multiphase Science and Technology*. 2001;**13**.

[180] R. Eastman. Dynamics of bubble departure. in *AIAA, 19th Thermophysics Conference*. 1984.

[181] N. Vargaftik, B. Volkov, L. Voljak. International tables of the surface tension of water. *Journal of Physical and Chemical Reference Data*. 1983;**12**:817-20.

VITA

Jingke Mo was born in Hengyang, Hunan, China. He graduated from high school in 2002. Jingke attended Beijing University of Aeronautics & Astronautics, graduated with a B.S. in Engineering Mechanics in 2006. Jingke went to graduate school at the University of Memphis in 2007 where he received his M.S. in Mechanical Engineering in 2009. He worked several years before returning to the school at the University of Tennessee, knoxville for his Ph.D. in Aerospace Engineering since 2014.